Synthesis, Characterization and Catalytic Application of Ru/Sn- and Cu/Zn-Based Nanocomposites

Dissertation

zur Erlangung der Doktorwürde

vorgelegt von

Yanzhi Guo

aus Shandong, China

Institut für Anorganische Chemie

der

Universität Duisburg-Essen

Essen 2006

Synthesis, Characterization and Catalytic Application of Ru/Sn- and Cu/Zn-Based Nanocomposites

Dissertation

submitted for the Degree

of Doctor of Natural Sciences

by

Yanzhi Guo

from Shandong, China

Institute of Inorganic Chemistry

University of Duisburg-Essen

Essen 2006

Index

1 Introduction

Since a long time the world has been relying on crude oil as the main energy source. Due to limited reserves and the soaring price of crude oil, and more importantly, increasing concerns about the environment, alternatives have to be developed. The usage of solar energy and hydrogen is among the most important strategies. For example, the decomposition of pure water to hydrogen and oxygen with photocatalysts such as RuO_2/SnO_2 is an attractive but challenging route [1]. Recently, with the development of fuel cells powered by hydrogen, which is highly efficient and environmental-friendly, the production and storage of hydrogen went into the focus of scientists and engineers.

The on-board supply of hydrogen for vehicles can generally be divided into three groups:

(1) storage of high-pressure or liquid hydrogen;

(2) use of metal-hydrides for hydrogen storage;

(3) reforming of methanol.

The lack of hydrogen refueling infrastructures, combined with the complexity of on-board storage and handling of hydrogen, are the drawbacks of applying pure hydrogen in vehicles. The alternative is to carry liquid fuels that have high energy densities and can be converted to hydrogen-rich gases by an on-board processor. Methanol is one of the most favorable liquid fuels due to the following reasons:

(1) low reaction temperature and atmospheric pressure;

(2) small molecule with high molar ratio of hydrogen to carbon;

(3) low CO concentration, which is poisonous to fuel cell;

(4) obtainable from natural gas, biomass, in addition to oil;

(5) minor efforts of changing the fuelling station from gasoline or diesel [2].

The production of methanol from synthesis gas (CO, H_2, CO_2) and the steam reforming of methanol to hydrogen-rich gases are based on $CuO/ZnO/Al_2O_3$ catalysts.

Various routes and reaction conditions were explored in this work for the synthesis of Ru-Sn- and Cu-Zn-Al- based nanocomposites. Online methods such as TG-IR or TG-MS were employed to study the thermolysis of metal or intermetallic precursors. SEM, TEM, XRD and EXAFS were used to elucidate the morphology and crystal structure of the samples. Physisorption and chemisorption were applied before the catalytic test of methanol synthesis to investigate the specific surface area, the pore structure, and the copper surface area.

Chapter 2 reviews the structures, properties and applications of different cyanide complexes, the Cu-based catalysts for methanol synthesis, and the application of sol-gel synthesis for the preparation of catalysts.

Chapter 3 reports the preparation and thermolysis of the Ru-Sn based coordination polymer $((CH_3)_3Sn)_4Ru(CN)_6$ in inert and oxidative atmosphere. Ru_3Sn_7 was almost quantitatively formed after thermolysis in nitrogen, whereas the mixed oxide $(Sn, Ru)O_2$ was formed in air. Both compounds can be obtained in a nanocrystalline state if the reaction conditions are properly chosen. This underscores the potential of this precursor method to prepare compounds away from thermodynamic equilibrium, e. g. with a high specific surface.

Chapter 4 presents a batch-wise and a continuous synthesis method for the precipitation of the copper–zinc coordination compound $Zn[Cu(CN)_3]$. Structurally, this compound consists of Cu–C–N–Zn units that bridge Cu and Zn centers. With the continuous overflow precipitation method, fine spherical particles were obtained at high solution concentrations and short residence time (or a high flow rate). The thermolysis of the cyanides was studied in-situ by TG-IR and TG-MS. Under oxidizing conditions, cyanogen is lost only at lower temperatures whereas at higher temperatures, thermal decomposition to carbon dioxide and nitrogen oxides occurs. The products were mixtures of CuO and ZnO, which were reduced to Cu/ZnO and used as catalysts for methanol synthesis. The ternary oxides $CuO/ZnO/Al_2O_3$ were prepared by the thermolysis of the precipitates of $Zn[Cu(CN)_3]/Al_2O_3$ and $Zn[Cu(CN)_3]/Al(OH)_3$. A higher catalytic activity was observed in methanol synthesis for the co-precipitated samples, which can be attributed to a high dispersion of Cu and improved metal-substrate interactions.

Chapter 5 discusses the synthesis and thermolysis of $Zn(CN)_2$ and the binuclear complex $[Zn(en)_3][Zn(CN)_4]$. Under oxygen, the thermolysis of both complexes led to ZnO nanoparticles with a size of 100–200 nm. There is no correlation between the morphology of the crystals of the parent compound and the ZnO particles, i.e., the structure completely

breaks down during thermolysis. It was found that under oxygen the decomposition of [Zn(en)$_3$][Zn(CN)$_4$] occurred in a few steps in the range of 150–500 °C, whereas that of the Zn(CN)$_2$ occurred in one step between 530 °C and 610 °C. The thermolysis of the Zn-based compounds is proved to be a promising route to nano-sized ZnO.

Chapter 6 reports a sol-gel route for the synthesis of nanostructured porous ZnO/Al$_2$O$_3$. It was found that ZnO could be atomically dispersed in Al$_2$O$_3$ in a wide range of Zn concentrations. A high content of Al$_2$O$_3$ led to amorphous ZnO with a high specific surface area and small pores. However, the maximum pore volume was obtained at a Zn:Al ratio of 1:1. As a result, the nanostructure of the oxides can be fine-tuned by the Zn:Al ratio. The obtained atomically-mixed bi-metallic oxides are promising supports for metals like Cu.

Chapter 7 explores a novel sol-gel route using propylene oxide as gelation initiator for the preparation of CuO/Al$_2$O$_3$ and CuO/ZnO/Al$_2$O$_3$. Cu-Al and Cu-Zn-Al precursor xerogels and aerogels were prepared by drying the wet gel under air and in supercritical carbon dioxide, respectively. After thermolysis at 400 °C, CuO/Al$_2$O$_3$ and CuO/ZnO/Al$_2$O$_3$ calcined xerogels and aerogels were obtained, which can be used as catalysts for the synthesis of methanol. The optimized CuO/ZnO/Al$_2$O$_3$ (Cu:Zn:Al=4:2:2) xerogel has a catalytic activity of about 59 % of the industrial reference catalyst. The porous CuO/Al$_2$O$_3$ and CuO/ZnO/Al$_2$O$_3$ aerogels prepared with this method have high specific surface areas.

Chapter 8 discusses a solution route for the synthesis of copper oxide, zinc oxide and copper-zinc mixed oxides, which were prepared by heat-treatment of the respective metal hydrate aqueous solutions at low temperatures. The preparation conditions, such as the addition of NaAOT (sodium bis(2-ethylhexyl) sulfosuccinate) or the variation of the solvents (aqueous or organic), have a significant effect on the morphology of the products. CuO leaflets, platelets and spherical particles were obtained in the synthesis without NaAOT in water, with NaAOT in water, and with NaAOT in a mixture of water and butanol, respectively. Flower-like ZnO structures consisting of ZnO rods with different shapes and sizes were formed in the presence of NaAOT, in water or in a mixture of water and butanol. The ratio of copper to zinc in the oxidic products can be easily varied in the synthesis.

2 Theoretical background

2.1 Cyanide coordination compounds

2.1.1 Cyanide complexes

More than 300 years ago, M. Diesbach for the first time prepared a bright blue pigment in an unusual way.[3] He boiled beef blood in a strongly basic medium and he was surprised to get a blue coloration. At this time, neither cyanide nor hexacyanometalates were known but Prussian blue was born, which is sometimes recognized as the first coordination compound.

The formula of the genuine Prussian blue is $Fe^{III}_4[Fe^{II}(CN)_6]_3 \cdot 14\ H_2O$ [4]. The structure was first proposed by Keggin and Miles [5] and then reformulated by Ludi and Güdel [6]. Prussian blues constitute a large family of cubic systems $C_nA_p[B(CN)_6]_q \cdot x\ H_2O$ where A occupies all the corners and all the centers of the faces and the $[B(CN)_6]$ units are located at the octahedral sites. C is a monovalent cation, which can be inserted into a part of the tetrahedral sites of the cubic structure. The reaction leading to the neutral solid is a simple Lewis acid–base interaction:

$$q[B(CN)_6]_{aq}^{\ p-} \text{ (Lewis base)} + pA_{aq}^{\ q+} \text{ (Lewis acid)} \rightarrow \{A_p[B(CN)_6]_q\}^0 \cdot x\ H_2O\ (s) \qquad (2\text{-}1)$$
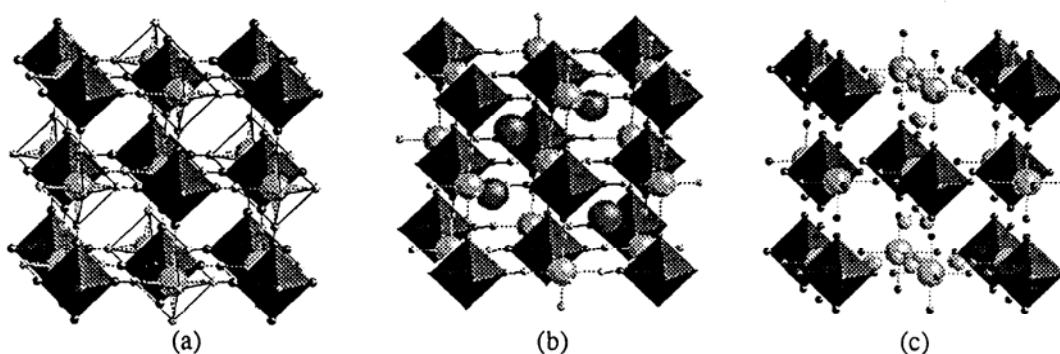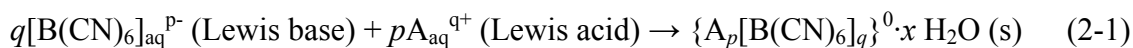
Fig. 2-1: Typical structures of cubic Prussian blue: (a) $A^{III}[B^{III}(CN)_6]$, A_1B_1; (b) $Cs^IA^{II}[B^{III}(CN)_6]$, $Cs_1A_1B_1$; (c) $\{A^{II}\}_3[B^{III}(CN)_6]_2 \cdot x\ H_2O$, A_3B_2. $[B(CN)_6]$ are the dark solid octahedra surrounded by CN (very small spheres), A are the light small spheres, C are the gray medium size spheres in (b); in (c) H_2O are shown by the small light-gray spheres [7].

Three kinds of structures appear in these complexes (Fig. 2-1) [7]. The first two are characterized by an A:B=1:1 stoichiometry, where the coordination spheres of A and B are $\{A(NC)_6\}$ and $\{B(CN)_6\}$. A(B) has six B(A) neighbors. The third structure has an A:B=3:2 stoichiometry, with one third of $[B^{III}(CN)_6]$ vacancies filled by water molecules; the B coordination sphere is left unchanged but the mean coordination sphere of A becomes $\{A(NC)_4(H_2O)_2\}$. The mean number of B neighbors around A is now four.

2.1.2 Application of metal cyanide complexes in catalysis

For multi-component catalysts it is essential that the small individual particles of the active component do not exhibit significant variations in chemical composition [8, 9]. When the active supported particles have a variable chemical composition, the experimentally observed activity and selectivity of the catalyst will mirror an average of the catalytic behavior of active species of a different chemical composition.

Generally, supported bimetallic catalysts are prepared using the same procedures as for the production of monometallic supported catalysts, such as impregnation, deposition-precipitation and ion exchange [10]. These procedures, however, usually result in supported catalyst precursors of a non-uniform chemical composition of the individual active particles. The variation of the chemical composition is mainly due to a lack of interaction between the two metals to be alloyed during the various steps of the preparation.

Metal cyanides are suitable complexes for the preparation of bimetallic catalysts with a uniform chemical composition [11]. Precipitates of a stoichiometrically fixed composition can be readily obtained by addition of a solution of a simple salt of the first metal to a complex cyanide anion of the second metal. As a result, a wide range of binuclear complexes can be prepared. In order to prevent unintentional promoting or poisoning effects of the cyanide ligands, it must be possible to remove the ligands completely at a relatively low temperature to avoid sintering of the catalysts.

As a matter of fact, a large range of industrially interesting supported catalysts can be potentially prepared from cyanide complexes [12, 13]. A prerequisite for the successful preparation of supported catalysts is a sufficient interaction of the precipitating precursor with the dispersed support. The dispersion of the cyanide precursors on the support can be

investigated using transmission electron microscopy (TEM) and X-ray photoelectron spectroscopy (XPS).

Table 2-1 shows some different combinations. It can be seen that combinations of a divalent metal ion, M^{II}, and iron cyanide complexes are possible in proportions M^{II}/Fe of 1.0, 1.5 and 2.0 by using Fe^{II} nitroprusside, Fe^{III} cyanide and Fe^{II} cyanide, respectively.

Table 2-1: Catalysts preparation from metal cyanide complexes for Fischer-Tropsch synthesis. Al_2O_3 can be used as support in general [14].

Catalyst	Precursor complex	Color (aq)	Color (s)
Fe	$Fe_3[Fe(CN)_6]_2$	dark blue	dark blue
Fe	$Fe_2Fe(CN)_6$	pale blue	dark blue
Cu_3Fe_2	$Cu_3[Fe(CN)_6]_2$	green	green
Cu_2Fe	$Cu_2Fe(CN)_6$	purple brown	purple brown
Ni_3Fe_2	$Ni_3[Fe(CN)_6]_2$	dark yellow	dark yellow
Ni_2Fe	$Ni_2Fe(CN)_6$	pale brown	pale brown
CoFe	$CoFe(CN)_5NO$	salmon pink	salmon pink
Co_3Fe_2	$Co_3[Fe(CN)_6]_2$	red brown	purple
Co_2Fe	$Co_2Fe(CN)_6$	pastel green	steel blue
Mn_3Fe_2	$Mn_3[Fe(CN)_6]_2$	brown	brown
Mn_2Fe	$Mn_2Fe(CN)_6$	pale grey	pale grey
CuNiFe	$CuNiFe(CN)_6$	purple brown	purple brown
FePd	$FePd(CN)_4$	white	orange brown
Fe_2Mo	$Fe_2Mo(CN)_8$	yellow green	grey blue
Cu_2Mo	$Cu_2Mo(CN)_8$	purple	purple
Ni_2Mo	$Ni_2Mo(CN)_8$	pastel green	pale green
Co_2Mo	$Co_2Mo(CN)_8$	orange	sand

Boellaard et al.[15] investigated the behavior of alumina supported copper-iron catalysts derived from metal cyanide complexes in the Fischer-Tropsch synthesis. The cyanide complexes $Cu_2Fe(CN)_6$, and $Cu_3[Fe(CN)_6]_2$ were precipitated on alumina support respectively. The cyanide precursors were subsequently treated in an oxygen/helium (1 vol% O_2) gas flow and

subsequently reduced in an hydrogen/argon (10 vol% H_2) gas flow at temperatures up to 548 K. The obtained CuFe, Cu_3Fe_2 and Cu_2Fe were used as catalysts for the Fischer-Tropsch synthesis. It was found that the initial activity of the copper-iron catalysts was much higher than that of the monometallic iron catalysts prepared also from a cyanide complex. Although the activity of the bimetallic catalyst then dropped slowly to a lower level, it remained higher than that of the monometallic iron catalysts.

The structure and decomposition process of nickel-iron cyanide $K_{0.8}Ni_{1.1}[Fe(CN)_6] \cdot 4.5\ H_2O$ were investigated by Ng et al.[16]. The coprecipitated cyanide complex was treated at different temperatures under pure argon to study the effect of annealing on the structure. The complex was annealed also in air to form a metastable structure. The structure of the cyanide complex is shown in Fig. 2-2.
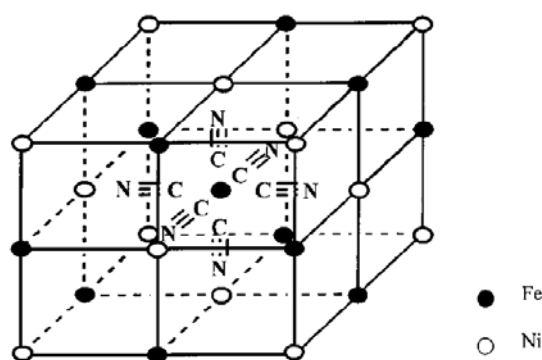
Fig. 2-2: Structure of Fe-Ni cyanide $K_{0.8}Ni_{1.1}[Fe(CN)_6] \cdot 4.5\ H_2O$. For simplicity and clarity, the K^+ ions and coordination water molecules have been omitted. The solid and dotted lines represent the cyanide (CN^-) bonds. In an ideal cubic structure, each Fe ion is bonded to a carbon atom while each Ni ion is bonded to a nitrogen atom [16].

The Fe and Ni ions are octahedrally coordinated by C and N atoms, respectively, forming three-dimensional bimetallic networks with the CN^- groups as the bridging ligands. The impurity atoms such as K^+ ions may occupy the interstitial sites in the cubic crystal lattice. The conversion of the ferromagnetic Fe^{III}-CN-Ni^{II} linkage to a paramagnetic Fe^{II}-CN-Ni^{III} linkage occurred after heat treatment at 150 °C in argon. When the annealing temperature was increased, another disordered structure $(Ni,Fe)(CN)_2O_{1..2}$ was observed. Decomposition of the cyanide began at 250 °C. This involved the loss of some cyanide ligand bondings, leading to structures such as $(Ni,Fe)(CN)_{1..2}$. This was completely decomposed above 550 °C, whereby nanoscaled Fe-Ni particles were found, as well as a minor amount of iron carbide and carbon

particles. Annealing at 600 °C under an argon/air mixture led to the formation of fairly pure Fe-Ni particles with particles size of 5-10 nm.

2.2 Cu-based catalysts for methanol synthesis

2.2.1 Reaction mechanism for methanol synthesis

Methanol synthesis by hydrogenation of CO or CO_2 is a moderately exothermic reaction [17]:

$$CO\ (g) + 2\ H_2\ (g) \rightarrow CH_3OH\ (l)\ (\Delta H_{298} = -91\ kJ\ mol^{-1}) \tag{2-2}$$

$$CO_2\ (g) + 3\ H_2\ (g) \rightarrow CH_3OH\ (l) + H_2O\ (l)\ (\Delta H_{298} = -49.5\ kJ\ mol^{-1}) \tag{2-3}$$
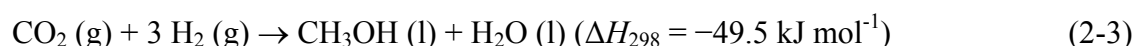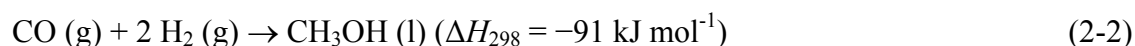
Reaction (2-2) and (2-3) are thermodynamically favored at low temperatures. To avoid the accumulation of a large amount of reaction heat, one-pass conversion of the reactant gas is only 15-25 % in the commercial process. It is necessary to set up a recycling unit to reuse the reactant gases that do not convert. Simultaneously, the water gas shift reaction (2-4) occurs as a side reaction in conventional processes, consuming water that is formed in reaction (2-3).

$$H_2O + CO \rightarrow H_2 + CO_2\ (\Delta H_{298} = -41.2\ kJ\ mol^{-1}) \tag{2-4}$$
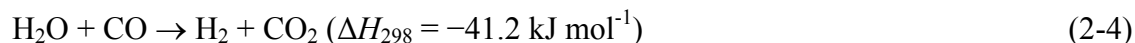
Combination of the water gas shift reaction results in a strong driving force, which dramatically increases the synthesis gas conversion [18].

Methanol synthesis from pure CO and H_2 via the formation of methyl formate has been discussed, where carbonylation of methanol and hydrogenation of methyl formate were considered as two main steps of the reaction [19, 20].

Many research projects have been carried out to elucidate the role of CO_2 in methanol formation. Klier [21] stated that CO_2 only adjusts or controls the surface composition, oxidation state, and dispersion of CuO in the catalyst but is not a direct reactant. On the contrary, Chinchen et al.[22, 23] suggested that CO_2 is the sole carbon source for methanol synthesis and summarized the reaction sequence as following:

$$H_2\ (g) \rightarrow 2\ H\ (a) \tag{2-5}$$

$$CO_2\ (g) \rightarrow CO_2\ (a) \tag{2-6}$$

$$CO_2 \text{ (a)} + H \text{ (a)} \rightarrow HCO_2 \text{ (a)} \qquad (2\text{-}7)$$

$$HCO_2 \text{ (a)} + 2 H \text{ (a)} \rightarrow CH_3O \text{ (a)} + O \text{ (a)} \qquad (2\text{-}8)$$

$$CH_3O \text{ (a)} + H \text{ (a)} \rightarrow CH_3OH \text{ (g)} \qquad (2\text{-}9)$$

$$CO \text{ (g)} + O \text{ (a)} \rightarrow CO_2 \text{ (g)} \qquad (2\text{-}10)$$

$$H_2 \text{ (g)} + O \text{ (a)} \rightarrow H_2O \text{ (g)} \qquad (2\text{-}11)$$
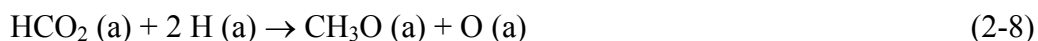
where, the gas phase and adsorbate species are indicated by (g) and (a), respectively. However, most researchers believe that CO and CO_2 can be both hydrogenated to methanol and the predominant reaction depends on the operating conditions.
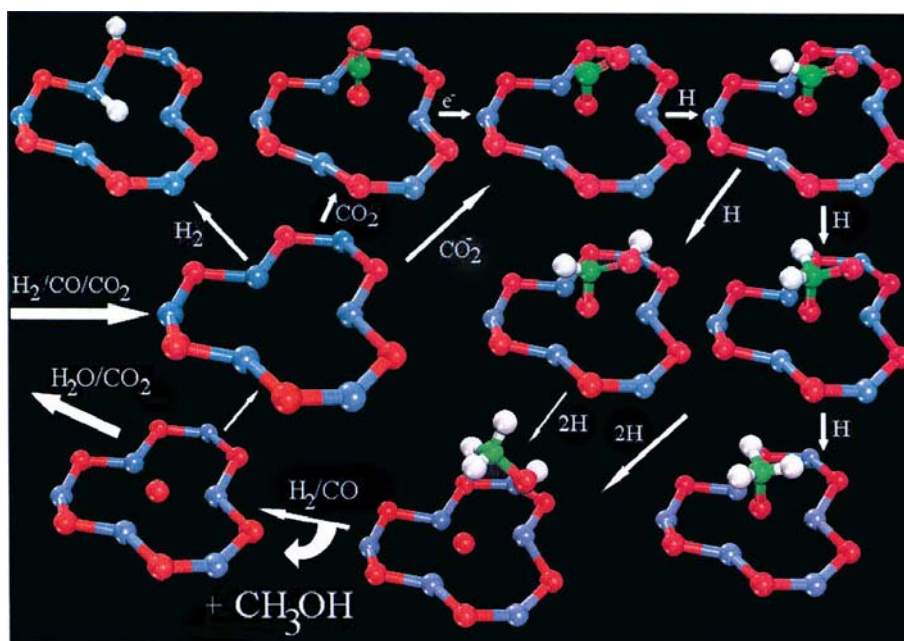
Fig. 2-3: Catalytic cycle for methanol synthesis from syngas ($CO/CO_2/H_2$). Pictorial representation of geometry optimized stable reactants, intermediates and products with the portion of surface substrate modeled in the QM region [24].

French et al.[24, 25] investigated the reactions on the surface of ZnO by quantum mechanics/molecular mechanics (QM/MM). The proposed catalytic cycle was summarized in Fig. 2-3. It is started with the adsorption of CO_2 and H_2. CO_2, upon adsorption in a neutral interstitial site, retains the linear structure exhibited in the gas phase. On adding an electron

the neutral CO_2 molecule bends and the extra electron populates an antibonding level. The interaction with the surface stabilizes the radical CO_2^- species. The reaction then proceeds by the hydrogenation of the adsorbed CO_2^- species. The adsorption of hydrogen leads to a closed-shell species. Further hydrogenation can proceed either through the formation of $H_2CO_2^-$ or $HCOOH^-$ (formic acid) as shown in Fig. 2-3. Further hydrogenation and interactions of the resulting species with the surface and possible surface defects lead to a large variety of possible intermediates. Examples of a methoxy ion (CH_3O^-) chemisorbed onto the surface and physisorbed methanol are also shown in Fig. 2-3. To complete the catalytic cycle, methanol is removed from the surface and the active site was recycled by desorption of carbon dioxide and water.

Zhang et al.[26] used CO/H_2, CO_2/H_2, and $CO/CO_2/H_2$, respectively, as reactant gases to investigate the function of CO_2. They found that both methanol formation rates for the individual CO and CO_2 hydrogenations were much lower than that for a CO/CO_2 mixture hydrogenation, and that the methanol formation rate for CO hydrogenation was lower than that for CO_2 at 490 K. This means that CO_2 remarkably promotes methanol formation and it is also a carbon source in methanol synthesis.
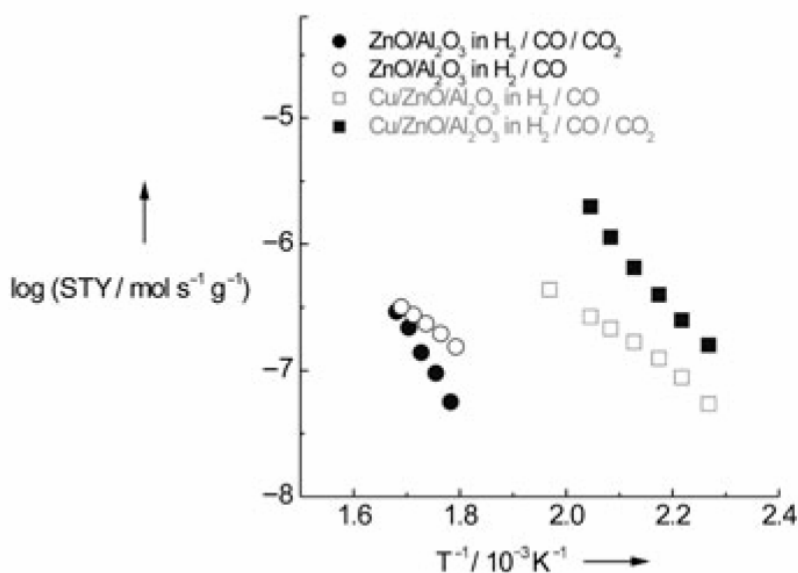
Fig. 2-4: Comparison of the activity of binary (ZnO/Al_2O_3) and ternary ($Cu/ZnO/Al_2O_3$) catalysts (STY: space-time yield) [27].

$Cu/ZnO/Al_2O_3$ is applied technically in large-scale, low-temperature methanol synthesis. Kurtz et al.[27] compared reactions performed using CO/H_2 and $CO/CO_2/H_2$ as syngases, with a Cu-free binary ZnO/Al_2O_3 catalyst and a ternary $Cu/ZnO/Al_2O_3$ catalyst under near-industrial conditions (Fig. 2-4). The ternary catalyst was found to be much more active than the binary ZnO/Al_2O_3 catalyst. A synthesis gas containing CO_2 results in a drastic increase in activity for the $Cu/ZnO/Al_2O_3$ system but a decrease for the ZnO/Al_2O_3 system.

Fakley and co-workers [28] proposed another mechanism, in which methanol reacts with methanoates on zinc oxide to produce methyl methanoate, which is ultimately hydrogenated when in contact with copper:

$$\textbf{Cu} \quad CO_2 + 3H_2 \rightarrow CH_3OH + H_2O \tag{2-12}$$

$$\textbf{ZnO} \quad OH\,(a) + CO \rightarrow HCOO\,(a) \tag{2-13}$$

$$HCOO\,(a) + CH_3OH \rightarrow HCOOCH_3 + O\,(a) \tag{2-14}$$

$$\textbf{Cu} \quad HCOOCH_3 + 4\,H\,(a) \rightarrow 2\,CH_3OH \tag{2-15}$$
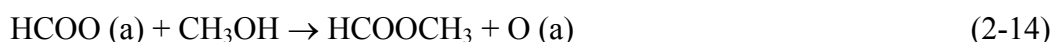
This route could explain the appearance of traces of methyl methanoate in the product stream during industrial synthesis. In addition, this bifunctional mechanism can better explain the synergy between the copper and zinc oxide.

Another bifunctional mechanism was proposed by Herman et al.[29], where the nondissociative Cu^+ sites chemisorb and activate carbon monoxide, while the hydrogen is activated on the zinc oxide surface. This model is illustrated in Fig. 2-5. The initial step in the synthesis of methanol over a Cu/ZnO catalyst is the adsorption and activation of CO on the Cu^+ sites and of hydrogen on the surrounding ZnO surface sites. The heterogeneous splitting of hydrogen and the bonding of CO to cationic Cu^+ sites represent an electrophilic attack on the carbon end of CO by protons and a nucleophilic attack on the oxygen end of CO by hydride ions. It was suggested that the hydrogenolysis of the Cu-CH_2OH bond is the rate-limiting step.
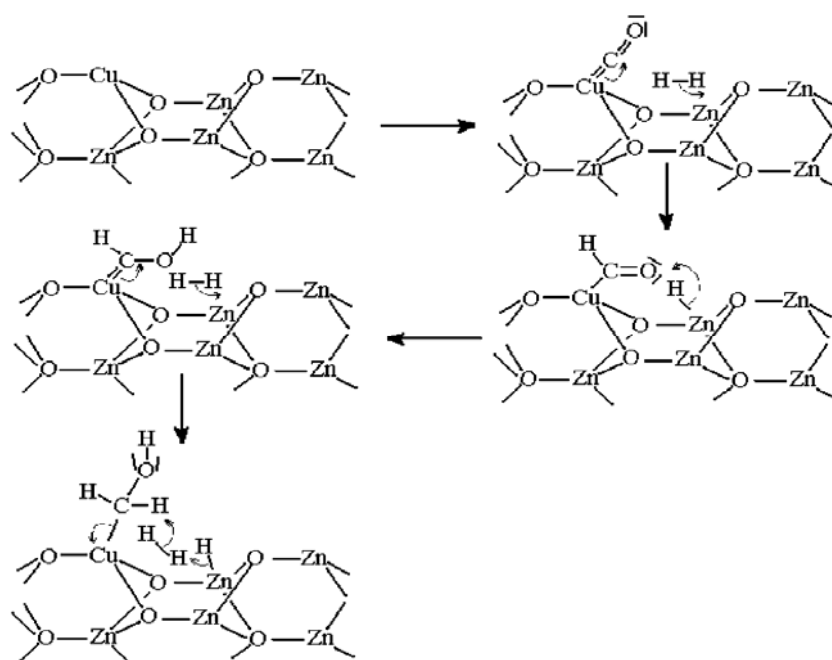
Fig. 2-5: Mechanism model for methanol synthesis [29].

Fisher and Bell [30] proposed another bifunctional mechanism for methanol synthesis from CO/H_2 on $Cu/ZrO_2/SiO_2$, in which formate species form on zirconia and undergo stepwise hydrogenation to bisoxymethylene, methoxide, and finally methanol, with atomic hydrogen being supplied through spillover from Cu. The reductive elimination of methoxide is slow in comparison to other steps in the reaction mechanism. The suppressed rate of methanol synthesis from CO as compared to CO_2 hydrogenation is the result of the absence of water formation, which prevents the more simple release of methoxide by hydrolysis. At the same time, the authors compared the rates of methanol synthesis on $Cu/ZrO_2/SiO_2$ and Cu/SiO_2 catalysts. They found that the enhanced rate of methanol synthesis on $Cu/ZrO_2/SiO_2$ as compared with that on Cu/SiO_2 could be attributed to the reaction proceeding through the lower energy formate route on $Cu/ZrO_2/SiO_2$, while proceeding through the higher energy formyl mechanism on Cu/SiO_2.

On the other hand, Tsubaki et al.[31] studied the reaction of a new methanol synthesis method on Cu/ZnO at low temperature (443 K) from syngas ($CO/CO_2/H_2$) using ethanol as a promoter. This new route of methanol synthesis consists of the following fundamental steps:

$$CO + H_2O \rightarrow CO_2 + H_2 \qquad\qquad (2\text{-}16)$$

$$CO_2 + H_2 + ROH \rightarrow HCOOR + H_2O \tag{2-17}$$

$$HCOOR + 2H_2 \rightarrow CH_3OH + ROH \tag{2-18}$$

Fig. 2-6 shows the mechanism scheme of the methanol synthesis using an ethanol promoter on a Cu/ZnO catalyst [32]. In this mechanism, formate adsorption species are formed at first by adsorbing the syngas (CO/CO$_2$/H$_2$) on Cu/ZnO catalysts. The gas-phase and physisorbed ethyl formate, the reactive intermediate, is then formed by the reaction of adsorbed formate and gas-phase ethanol. The ethyl formate is reduced by hydrogen atoms on Cu/ZnO to form gas-phase methanol directly. The formation of ethyl formate is a key step in this methanol synthesis route at low temperature.
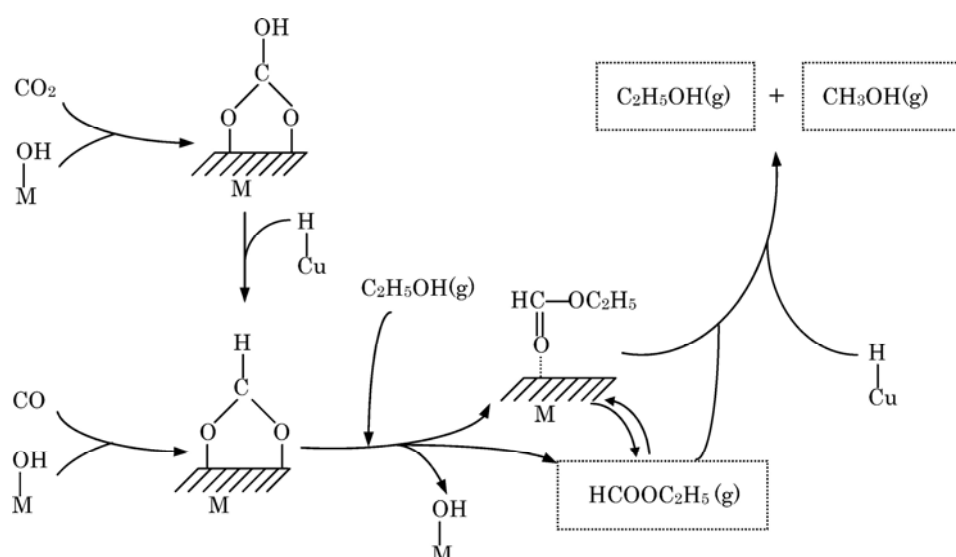
Fig. 2-6: Proposed mechanism for the low temperature synthesis of methanol from syngas (CO/CO$_2$/H$_2$) using ethanol as promoter (M is Cu/ZnO) [32].

2.2.2 Catalysts for methanol synthesis

Catalysts prepared by the coprecipitation method

The copper/zinc oxide catalyst supported on alumina is industrially important for methanol synthesis from synthesis gas (CO$_2$, CO and H$_2$)[33]. Coprecipitation methods are the most widely used methods to prepare copper-based catalysts. Precipitators such as sodium carbonates and oxalates are added to a solution of the desired salts to coprecipitate and form

the catalyst precursors. The metal oxides are then obtained by calcination of the precursors. The properties and catalytic activities of the products can be adjusted by the preparation conditions, such as pH, concentration, stirring rate, duration of precipitation and aging, and calcination conditions.

Previous studies indicate that the precipitation parameters strongly affect the performance of a Cu-ZnO-based catalyst, in which Cu/ZnO catalysts are prepared using precursors such as hydrozincite $Zn_5(CO_3)_2(OH)_6$, aurichalcite $(Cu_x,Zn_{1-x})_5(CO_3)_2(OH)_6$, malachite $Cu_2(CO_3)(OH)_2$, zincian-malachite $(Cu_x,Zn_{1-x})_2(CO_3)(OH)_2$, or their mixtures [34-37]. Günter et al.[38] investigated the binary Cu/ZnO catalysts with varying Cu:Zn molar ratios (90/10 to 10/90) and found that the precursor phase composition directly influences the resulting Cu microstructure and in turn the performance of the Cu/ZnO catalyst. Three multiphasic composition ranges in the hydroxycarbonate precursors can be distinguished as a function of composition. The first region extends from 0 to ~15 mol% Zn and encompasses the pure malachite phase as well as zincian-malachite phase. The second region extends from 20 to 50 mol% Zn and encompasses the transition from zincian-malachite to aurichalcite. The third region at a Zn concentration larger than 50 mol% encompasses the transition of aurichalcite to hydrozincite. The Cu-containing hydrozincite, upon calcination and reduction, preferentially gives microstrained Cu crystallites, which exhibit a higher intrinsic activity for methanol synthesis.

The pH value plays an important role in determining the composition of the precipitates. The effect of the preparation pH on the composition of the precursors and the activity of the Cu/ZnO/Al₂O₃ catalysts for methanol synthesis was studied by Fang et al.[39]. It was found that at lower pH value, $Cu_2(CO_3)(OH)_2$ and $(Cu, Zn)_2CO_3(OH)_2$ are main phases of the precursors. With the increase of pH, the content of $(Cu,Zn)_6Al_2CO_3(OH)_{16}\cdot4\ H_2O$ increases and the content of $Cu_2(CO_3)(OH)_2$ and $(Cu, Zn)_2CO_3(OH)_2$ decreases. The catalyst prepared at pH = 8 shows the highest activity for methanol synthesis.

Ageing is also a key step in the post precipitation process for the microstructure of the catalyst precursors [40]. Bems et al.[41] studied the influence of ageing on the microstructure of the Cu/Zn hydroxycarbonate precursors and the Cu/Zn oxides obtained by subsequent calcination. An illustration of the relevant microstructural features with respect to the properties of the calcined oxides is shown in Fig. 2-7. The primary catalyst particles are almost equally sized

oxide particles with a substantial solid-solid interface. The geometry of the interface and the internal microstructure of both components can result from the peculiarities of the precursor. The amorphous and therefore more reactive precursor with high hydroxide and nitrate contents allows the growth of well-separated large CuO and ZnO crystallites, whereas a finely granular and crystalline precursor produces an intimate intergrowth of small and distorted oxide crystallites.

Fig. 2-7: Evolution of the microstructural characteristics with ageing of the precursors and the resulting oxides [41].

Ning et al.[42] compared the morphology, structure and catalytic activity of the ternary CuO/ZnO/Al$_2$O$_3$ catalysts prepared by the oxalate gel-coprecipitation method and the conventional hydroxycarbonate coprecipitation method. A homogeneous Cu and Zn distribution over spherical particles was obtained when oxalate was used as the precipitator, whereas irregular particles with Cu aggregates on the surface of the catalyst were found when carbonate salts were used as coprecipitation agents. The sample obtained using oxalate showed a higher Cu-dispersion and therefore a higher catalytic activity for methanol sythesis than the sample prepared using carbonate.

Catalysts prepared by other methods

Cu-based catalysts can be also prepared by other methods. Vukojević et al.[43] reported that colloidal copper nanoparticles synthesized by reduction of copper acetylacetonate with trialkylaluminum are highly active for homogeneous methanol synthesis. The organoaluminum compounds also stabilize the colloid by forming an organometallic protecting shell around the nanoparticles. The copper particle size is in the range of 3-5 nm.

Freshly synthesized copper colloids were tested for methanol formation in a high-pressure, stainless steel autoclave in a quasi-homogeneous phase. The copper nanoparticles were remarkably active catalysts in the quasi-homogeneous phase for methanol synthesis.

Chemical vapor deposition (CVD) was also used to prepare Cu/ZnO catalysts for methanol synthesis. Becker et al.[44] synthesized Cu/ZnO nanocomposites on the support of periodic mesoporous silicates, such as MCM-41 and MCM-48. The supported Cu/ZnO catalysts were obtained via metal-organic CVD using Cu(OCHMeCH$_2$NMe$_2$)$_2$ and ZnEt$_2$ as precursors. The obtained Cu/ZnO/MCM-48 sample shows a high activity for methanol synthesis. Kurtz et al.[45] prepared the binary Cu/Al$_2$O$_3$ catalyst by the coprecipitation method and the ternary Cu/ZnO/Al$_2$O$_3$ catalyst via CVD of ZnEt$_2$ on the Cu/Al$_2$O$_3$ samples. It was found that the CVD synthetic route enhanced the synergy between Cu and ZnO, leading to a higher catalytic activity for methanol sythesis.

2.2.3 Effects of ZnO and Al$_2$O$_3$ in Cu-based catalysts

Effect of ZnO

It is widely accepted that the use of ZnO as a support material leads to a highly dispersed Cu catalyst. The effect of ZnO on the activity of Cu-based catalysts can be classified into three categories:

(1) ZnO acts as a reservoir of hydrogen for the hydrogenation of CO over Cu surfaces [46, 47];

(2) the morphology of copper particles on the ZnO support is responsible for the effect of ZnO in the methanol synthesis [48, 49];

(3) ZnO$_x$ species migrate under reducing conditions onto the Cu surface forming Cu-Zn active sites and stabile Cu species [50, 51].

Dennison et al.[52] observed that hydrogen is adsorbed on ZnO to a much greater extent when Cu is present in the catalyst. On the other hand, Burch and co-workers [46] found that hydrogen spillover from Cu to ZnO occurs very rapidly from a partially oxidized Cu surface but only to a very small extent from a fully reduced copper surface. Moreover, the hydrogen atoms were trapped at surface defects or at interstitial sites of ZnO, but they were not held too strongly. This means that a possible role of ZnO might serve as a reservoir to provide H atoms for

subsequent hydrogenation of adsorbed reaction intermediates. Similarly, Spencer [47] suggested that synergistic effects are the result of H spillover produced from ZnO to Cu metal.

A morphology effect was also postulated to state the role of the zinc oxide support in a Cu-based catalyst. The ZnO support may optimize the dispersion of the Cu particles and stabilize many active sites by preventing the unavoidable agglomeration of Cu particles which takes place during a long-term operation, and by restraining Cu particles from being poisoned by feed gas impurities. Yoshihara and Campbell [53] found that the active sites in methanol synthesis on Cu/ZnO catalysts are metallic Cu and the role of the ZnO support is to stabilize more metallic Cu sites. On the other hand, Ovesen et al.[48] correlated the changes in particle morphology and the number of oxygen vacancies at the Zn-O-Cu interface. They showed that the interaction between copper and zinc oxides is important for the dynamic spreading of the copper particles on the support.

Fujitani et al.[51, 54] suggested that ZnO is also an active component in methanol synthesis. They observed that Zn species could migrate to the Cu surface in a physical mixture of Cu/SiO_2 and ZnO/SiO_2 upon reduction with H_2. The quality of the active sites was not changed, but the quantity of the active sites increased with increasing reduction temperature. This means that the role of ZnO is to create Cu-Zn active sites on the Cu surface. The catalytic activity of a Zn-deposited Cu (111) surface was much higher than that of Cu (111) alone. They also postulated a model for the function of ZnO sites during methanol synthesis. As we can see in Fig. 2-8, the model explains that the role of ZnO was not to improve the morphology of Cu sites but to create the Cu-Zn active sites for methanol synthesis. In this context, ZnO modifies the electronic properties of Cu sites by an electron exchange and interaction with Cu particles.

Naumann d'Alnoncourt et al.[55] investigated the influence of ZnO on the heat of adsorption of CO on a ternary ($Cu/ZnO/Al_2O_3$) and two binary (Cu/ZnO and Cu/Al_2O_3) catalysts. The shape of the adsorption isotherms and the initial heat of adsorption was different for the catalysts with and without ZnO. The initial heat of adsorption was found to be inversely correlated with the activity for methanol synthesis: $Cu/ZnO/Al_2O_3$ had the lowest initial heat of adsorption and was the most active catalyst for methanol synthesis, whereas Cu/Al_2O_3 had the highest initial heat of adsorption and the lowest activity. The decrease in the heat of adsorption of CO induced by the presence of ZnO is rationalized by strong metal-support interactions, i. e.,

ZnO_x species are assumed to cover the Cu metal surface presumably as Zn + O coadsorbate under reducing conditions.
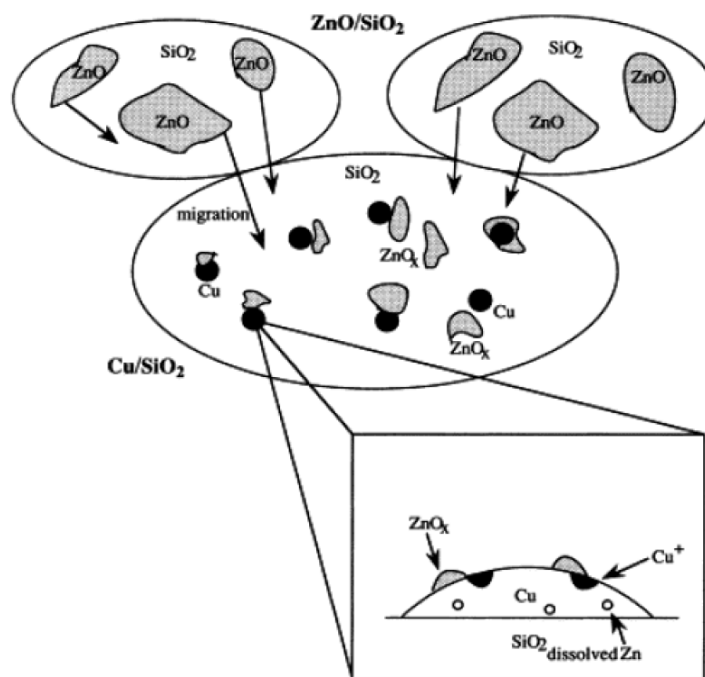
Fig. 2-8: Model of the active site for methanol synthesis over a physical mixture of Cu/SiO_2 + ZnO/SiO_2 [51].

Effects of Al_2O_3 in Cu-based catalysts

Al_2O_3 is widely used as a promoter in the Cu-based catalyst. The formation of zinc aluminate can prevent the agglomeration of active sites. In addition, Al_2O_3 accelerates the adsorption and activation of CO because of its disorder and defect surface domain. Furthermore, it can also stabilize the highly dispersed Cu/ZnO structure. Chen et al.[56] reported that doping with trivalent metal ions such as Al^{3+}, Sc^{3+}, and Cr^{3+} could also enhance the formation of monovalent cationic defects on the crystal surface of ZnO, which might accelerate both enrichment and stabilization of Cu^+ on the surface during the reduction and reaction processes.

Kurtz et al.[57] compared the binary Cu/ZnO as well as the ternary $Cu/ZnO/Al_2O_3$ catalyst with respect to their catalytic activity and stability in methanol synthesis. $Cu/ZnO/Al_2O_3$ had a higher initial catalytic activity than Cu/ZnO. After 75 h the activity of Cu/ZnO decreased

much more rapidly than that of Cu/ZnO/Al$_2$O$_3$. Because the decrease in the catalytic activity is particularly pronounced for the Al$_2$O$_3$-free Cu/ZnO catalyst, Al$_2$O$_3$ can be regarded as a stabilizer for the Cu cystallites by preventing the Cu particles from sintering. In addition, the presence of Al$_2$O$_3$ enhances the metal-support interactions, which, in turn, facilitate the formation of more active Cu particles.

2.3 Application of sol-gel methods to catalyst preparation

2.3.1 An overview of sol-gel processes

The sol-gel process is a versatile solution process for the preparation of material with a variety of structures and properties [58, 59]. In general, the sol-gel process involves the transition of a system from a liquid sol (mostly colloidal) into a solid gel phase. As shown in Fig. 2-9, the starting materials used in the preparation of the sol are usually inorganic metal salts or metal-organic compounds such as metal alkoxides. In a typical sol-gel process, the precursor is subjected to a series of hydrolysis and polymerization reactions to form a colloidal suspension, or a sol. The colloidal nanoparticles in the sol are then linked to each other in a 3-dimensional, liquid-filled solid network (wet gel). The transformation to a gel can be initiated in several ways, but the most convenient approach is to change the pH of the reaction solution. Further processing of the sol enables one to make materials in different forms. Thin films can be produced on a piece of substrate by spin coating or dip-coating. If the viscosity of a sol is adjusted into a proper viscosity range, fibers can be drawn from the sol.

The method used to remove liquid from a solid will affect the product's properties. If the liquid in a wet gel is removed under supercritical conditions, a highly porous and extremely low-density material ("aerogel") is obtained. If the gel is dried slowly in a fluid-evaporation process, the gel's structural network collapses and a high-density material known as xerogel is thus obtained.

Alkoxides are common precursors in sol-gel chemistry. However, alkoxides can be very reactive and are commercially available for only a number of elements, which restricts the types of materials that can be prepared. In studying the mechanisms that drive the sol-gel process, it was found that organic epoxides can also initiate the reaction [60] [61]. With this approach, precursors that are more widely available can be used, thus increasing the number of potential materials that can be developed. In addition, the starting materials, solvents, and

gelling agents used with epoxides are less expensive than those used with alkoxides. Reducing the production costs may increase the commercial interest in new sol-gel materials.
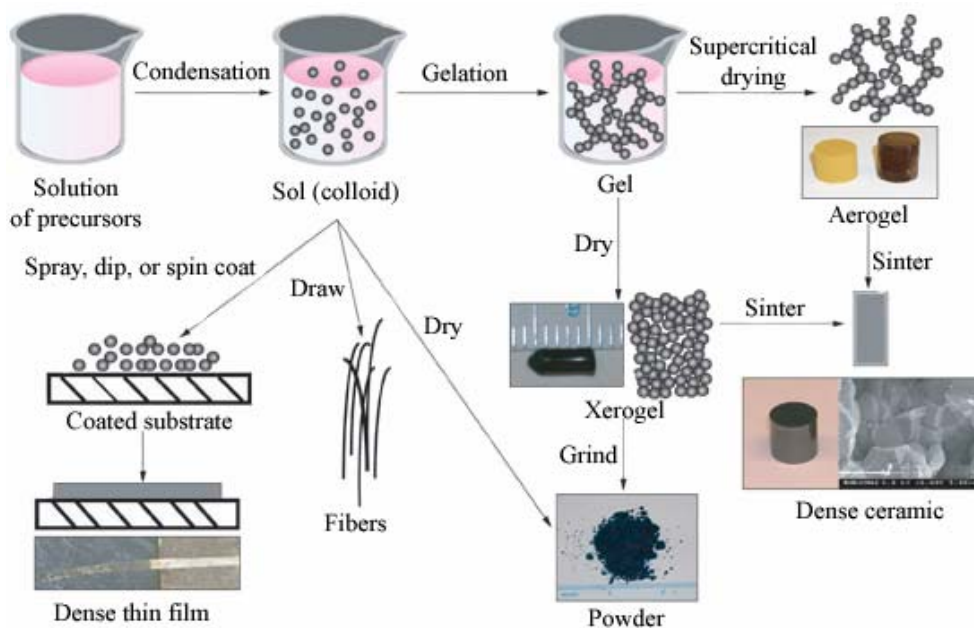
Fig. 2-9: Sol-gel technologies and their products [62].

2.3.2 Application of sol-gel methods in catalysis

Catalyst preparation usually involves complex processes. The performance of the final product is very sensitive to rather subtle changes in the synthesis procedure. Because of the possibility of controlling the variables involved in solid synthesis, the sol-gel route can be considered as an extremely interesting way to prepare catalysts. The versatility of the sol-gel techniques allows to control the texture, composition, homogeneity and structural properties of solids, and makes it possible to prepare tailored materials such as dispersed metals, oxide catalysts and chemically modified supports.

The goal of catalytic processes is to obtain high levels of catalytic activity. The conversion of reagents into products takes place on defined sites on the surface of the solid. The higher the number of the active sites, the higher the activity that will be exhibited by the solids. This points to the interest of increasing the number of active sites and controlling their nature during the catalyst preparation in order to obtain high activity. The selectivity of catalysts is

also related to the nature of the active sites, the reaction kinetics and the control of the reaction conditions.

The number and properties of the active sites and the reaction kinetics depend on several factors, which can be controlled to some extent by the sol-gel synthetic methods. These factors include:

(1) high specific surfaces;

(2) controlled pore size distribution;

(3) textural stability under the preparation and reaction conditions;

(4) a good and homogeneous dispersion;

(5) structural properties must be controllable in order to obtain the desired crystalline or amorphous structure;

(6) easily controlled composition, especially for the preparation of multi-component catalysts, or catalysts promoted by small concentrations of additives;

(7) mechanical properties should meet the requirements of the reaction conditions;

(8) the catalysts should be active as long as possible without severe deactivation due to chemical or physical blocking of active sites.

Table 2-2 presents a general overview of different catalysts prepared by sol-gel methods [63].

Table 2-2: Catalyst supports or catalysts prepared by sol-gel methods [64].

Materials		Application in catalysis
Single oxide	SiO_2	support, spillover
	Al_2O_3	support, spillover
	ZrO_2	support, spillover
	TiO_2	support, photocatalysis
	ThO_2	partial oxidation
	Cr_2O_3	partial oxidation
	Fe_2O_3	partial oxidation
	MoO_2	support
Binary oxides	$NiO-Al_2O_3$	partial oxidation, nitroxidation
	$NiO-SiO_2$	nitroxidation
	$NiO-MgO$	nitroxidation, ammonia synthesis
	V_2O_5-MgO	ammonia synthesis
	$Cr_2O_3-Al_2O_3$	nitroxidation
	$PbO-Al_2O_3$	nitroxidation
	$PbO-ZrO_2$	nitroxidation
	$Fe_2O_3-Al_2O_3$	Fischer-Tropsch
	$Fe_2O_3-SiO_2$	Fischer-Tropsch
	$CuO-Al_2O_3$	partial oxidation
Ternary oxides	$NiO-SiO_2-Al_2O_3$	nitroxidation, partial oxidation
	$NiO-Al_2O_3-MgO$	nitroxidation, partial oxidation
	$NiO-SiO_2-MgO$	nitroxidation, partial oxidation
	$NiO-Fe_2O_3-Al_2O_3$	nitroxidation, partial oxidation
	$NiO-V_2O_5-MgO$	nitroxidation, partial oxidation
	$NiO-MgO-Al_2O_3$	nitroxidation, partial oxidation
	$Fe_2O_3-NiO-Al_2O_3$	nitroxidation, partial oxidation
	$Cr_2O_3-Al_2O_3-MgO$	nitroxidation, partial oxidation, $NO+NH_3$
	$Cr_2O_3-Fe_2O_3-MgO$	nitroxidation, partial oxidation, $NO+NH_3$
	$Cr_2O_3-Fe_2O_3-Al_2O_3$	nitroxidation, partial oxidation, $NO+NH_3$
Metal-oxide	$Pt-SiO_2$	hydrogenation
	$Ni-SiO_2$	hydrogenation
	$Ni-Al_2O_3$	hydrogenation
	$Ni-SiO_2-Al_2O_3$	hydrogenation
	$Ni-SiO_2-MgO$	hydrogenation
	$Cu-Al_2O_3$	hydrogenation
	$Cu-SiO_2$	hydrogenation
	$Cu-MgO$	hydrogenation
	$Ni-MoO_2$	hydrogenation
	$Pb-Al_2O_3$	hydrogenation
	$Cu-ZrO_2$	hydrogenation
	$Cu-ZrO_2-Al_2O_3$	hydrogenation
	$Cu-ZnO- Al_2O_3$	hydrogenation

2.3.3 Preparation of catalysts by sol-gel methods

Materials obtained by sol-gel methods have been used as photocatalysts for the degradation of organic wastes at room temperature [65, 66]. An example of this application is the photocatalytic degradation of 3-chlorosalicylic acid over TiO_2 membranes [66]. The selected halogenated organic compounds, such as dibromoethane, trichloroethylene, chlorobenzenes or chlorophenols, can present severe environmental pollution risks. Sabate et al. [66] designed a continuous-flow reactor in which the TiO_2 catalyst was deposited on a glass tube. The coating procedure is carried out as follows: A solution of titanium tetraisopropoxide in isopropanol is rapidly mixed with water at room temperature. A gel is obtained after 30 min. This hydroxide gel is treated with HNO_3 to form a highly dispersed stable colloidal solution. A glass tube is immersed into the colloidal sol for 30 s. It is then withdrawn at a controlled slow speed, dried at room temperature for 1 h, and calcined at 400 °C for 3 h. Eight layers of TiO_2 are successively deposited in this way. A TiO_2 membrane with a total thickness of 1.3 μm is then obtained. Degradation of the 3-chlorosalicylic acid with bubbling air leads to the formation of HCl and CO_2 without significant deactivation over time.

Titania-based catalysts prepared by so-gel method were also used for formaldehyde photocatalytic oxidation [67]. Titania sols were prepared by acid hydrolysis of a $TiCl_4$ precursor instead of titanium alkoxides. The acid concentration can effect the particle size and stability of sols. Stable titania sols with smallest particles of 14 nm were obtained when the H^+/Ti molar ratio was 0.5. The titania sols were modified with SiO_2 and ZrO_2 to synthesize a series of modified catalysts, which were used for the photocatalytic oxidation of formaldehyde at 37 °C. Compared to pure TiO_2, the addition of silica or zirconia significantly increased the photocatalytic activity. This increase was attributed to a higher surface area and porosity or a smaller crystallite size.

Anhydrous formaldehyde is generally produced via the dehydration reaction of an aqueous solution of formaldehyde [68, 69]. Due to the high cost of this procedure, a one-step process was developed which yields anhydrous formaldehyde from direct dehydrogenation of methanol using Ag-containing catalysts [70, 71]. The Ag-SiO_2-MgO sol-gel composites were prepared from the precursors of $Si(OC_2H_5)_4$ (TEOS), $Mg(NO_3)_2 \cdot 6\ H_2O$ and $AgNO_3$. An aqueous solution of $AgNO_3$ and $Mg(NO_3)_2$ was added to the silica sol solution, followed by aging at 75 °C, drying at 120 °C and calcination at 900 °C. The obtained Ag-SiO_2-MgO catalyst

showed high activity (conversion of 96 % and selectivity of 78 %) in the direct dehydrogenation of methanol to anhydrous formaldehyde.

Vanadia-silica xerogels and aerogels were prepared by the sol-gel method and used as catalysts for epoxidation reactions [72]. Gels were obtained from vanadium(III)acetylacetonate and $Si(OC_2H_5)_4$ (TEOS) with various V/Si molar ratios. The structure of the mixed oxides was influenced mainly by the V/Si molar ratio and the drying mode. The catalytic behaviour of the xerogels and the aerogels was tested in the epoxidation reaction of trans-2-hexen-1-ol. The results showed that the V/Si ratio did not significantly influence the catalytic activity, but that the effect of the drying mode (xerogel or aerogel) was remarkable. The reaction time needed to achieve a maximum yield varied between 7 and 12 h for the xerogels, whereas only 2 h was required with the aerogels. The difference in the catalytic behaviour was attributed to a difference in the metal-support interactions and the coordination of the supported vanandia with the reactants.

3 Thermolysis of (Me$_3$Sn)$_4$Ru(CN)$_6$: preparation and characterization of Ru$_3$Sn$_7$ and (Ru, Sn)O$_2$

3.1 Introduction

Coprecipitation is widely used to prepare nano-scale bimetallic systems such as catalysts [73, 74]. In contrast, organometallic coordination polymers give the possibility to blend two or more different metals on an atomic scale, i.e. to avoid the necessity of mixing the individual compounds as separate solid phases. Due to the fact that the metals are already constituents of one crystalline phase, a lower reaction temperature can be expected for the thermolysis of such precursors compared to conventional syntheses where a high temperature is required to achieve a sufficiently fast diffusion of the compounds [75, 76].

Such systems are therefore recognized to be suitable precursors for intermetallic compounds that incorporate the initially blended metals. The class of coordination polymers based on trimethyltin units and hexacyanometallates, (Me$_3$Sn)$_n$M(CN)$_6$ (Me = CH$_3$; n = 3, 4; M = Fe, Co, Ru), offers versatile precursor compounds because they can be easily prepared from trimethyltin chloride and the corresponding potassium hexacyanometallates by a precipitation reaction [77-79]. The thermolysis of different compounds of this class of reactants has been studied and it was shown that intermetallic phases and mixed oxides can be prepared by this reaction at moderate temperatures [80, 81].

Controlled thermolysis of cyanide-containing coordination polymers was shown to be suitable for the preparation of nanocrystalline intermetallics and metal oxides. Heibel et al. [82] prepared Pd/Co alloys and the binary oxide PdCoO$_2$ by the thermolysis of a "cyanogel" obtained from K$_2$PdCl$_4$ and K$_3$Co(CN)$_6$. The processing atmosphere had a significant influence on the nature of the decomposition products. Sharp et al. [83] studied the thermolysis of cyanogels prepared from SnCl$_4$·5 H$_2$O and K$_4$[Fe(CN)$_6$] and found that the decomposition was a multi-step process. The products were α-Fe$_2$O$_3$ and SnO$_2$ with good CO-sensing properties due to a high BET surface area.

A variety of applications can be found for the Ru–Sn system including catalysis, gas sensors and electrode materials. Supported Ru–Sn catalysts prepared by co-impregnation were reported to be active and selective in the hydrogenation of citric [84] and oleic acid [85]. In this

bimetallic system, tin is believed to be an effective promoter that considerably improves the catalytic activity and selectivity [85]. The composition and structure of the bimetallic system as well as the interaction of Ru and Sn play a key role in the enhancement of the catalytic activity. Sato et al. [1] employed RuO$_2$-doped SnO$_2$ as photocatalyst for the decomposition of pure water to hydrogen and oxygen. It was also reported that the surface of SnO$_2$ which was functionalized by RuO$_2$ was very effective in chemical sensing of hydrocarbons [86]. The amount and distribution of the doped RuO$_2$ were among the most important parameters for hydrocarbon sensing. In addition, RuO$_2$ is a very promising electrode material due to its large capacitance and high conductivity [87-89]. Ultrafine RuO$_2$/SnO$_2$ binary oxide particles have also been prepared by Ito et al. [90] and Wang et al. [91] by sol–gel processes.

Based on earlier studies [80, 81], the thermolysis of the title compound was studied in detail in order to learn more about the properties of the products, which are obtained under either inert or oxidizing conditions.

3.2 Experimental

(Me$_3$Sn)$_4$Ru(CN)$_6$·2 H$_2$O was prepared by precipitation from aqueous solutions of trimethyltin chloride and potassium hexacyanoruthenate in stoichiometric amounts (Me = CH$_3$) [80].

$$K_4Ru(CN)_6 + 4\ Me_3SnCl \rightarrow (Me_3Sn)_4Ru(CN)_6\downarrow + 4\ KCl \qquad (1)$$
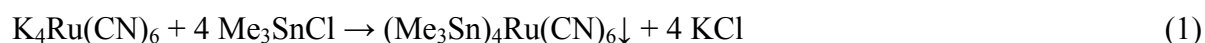
The precipitate was isolated by filtration and dried under air at room temperature.

The controlled thermolysis of the coordination polymer was carried out in a horizontal quartz tube reactor with an inner diameter of 30 mm. The thermal decomposition products under nitrogen or air were collected at different temperatures from 200 °C to 1000 °C after a pre-set reaction time (typically 0.5 or 4.5 hours).

Thermogravimetry-infrared spectroscopy (TG-IR) was carried out with a Netzsch STA 409 TG-DTA/DSC apparatus connected to a Bruker Vertex 70 infrared system for in-situ gas analysis. The samples were heated from room temperature to 1000 °C at a rate of 5 K min^{-1} under either N$_2$ or O$_2$ with flow rates of 50 mL min^{-1}. The evolved gases were monitored in-situ by IR spectroscopy. X-Ray diffraction was carried out with a Siemens D5000 system with Cu Kα radiation (1.54178 Å; Bragg–Brentano geometry; Al sample holders). The

morphology of the thermolysis products was studied by scanning electron microscopy (LEO Gemini 1530). IR characterization of the products was performed with a BIO-RAD FTS 175 instrument in KBr pellets.

3.3 Results and discussion

The coordination polymer was obtained as a dihydrate during precipitation. Elemental analysis gave 22.6 wt% C (calc. 22.8 wt%), 3.5 wt% H (calc. 4.2 wt%), and 8.6 wt% N (calc. 8.8 wt%). The crystal water was completely lost after longer exposure to air, which was confirmed by elemental analysis, i.e. 23.8 wt% C (calc. 23.7 wt%), 3.9 wt% H (calc. 3.9 wt%), and 8.9 wt% N (calc. 9.2 wt%). Experiments were carried out with either the dihydrate or the anhydride, as indicated below. The crystal structure of the coordination polymer with four molecules of crystal water was determined earlier by single crystal X-ray diffraction [92].

3.3.1 Thermolysis under nitrogen

The thermolysis in nitrogen occurred in a multi-step process (Fig. 3-1a). The weight loss started around 230 °C. The simultaneously recorded IR spectra (Fig. 3-1b) showed that C–H-containing species (2920 cm^{-1} and 2985 cm^{-1}) made up the majority of the decomposition gases. These must be fragments of the trimethyltin groups. At a slightly higher temperature (250 °C), the cyanide band at 2324/2360 cm^{-1} occurred as well, indicating either dicyane or trimethyltin cyanide. The simultaneous presence of C–H bands suggests the presence of trimethyltin cyanide. For dicyane, IR bands at 2117, 2298, 2541, and 2659 cm^{-1} are reported in the NIST database; therefore we conclude that dicyane is a minor volatile decomposition product.

The final weight of the residue of 47.5 wt% was considerably smaller than the metal concentration of 63.1 wt% in the original coordination polymer, which indicates that either Ru or Sn were lost. It is likely that tin was lost in the form of trimethyltin cyanide because the final weight was closer to the composition of Ru$_3$Sn$_7$, for which we expect a residual weight of 41.5 wt%. However, there must be some excess in tin (present in elemental form, see below) in the Ru$_3$Sn$_7$ phase.
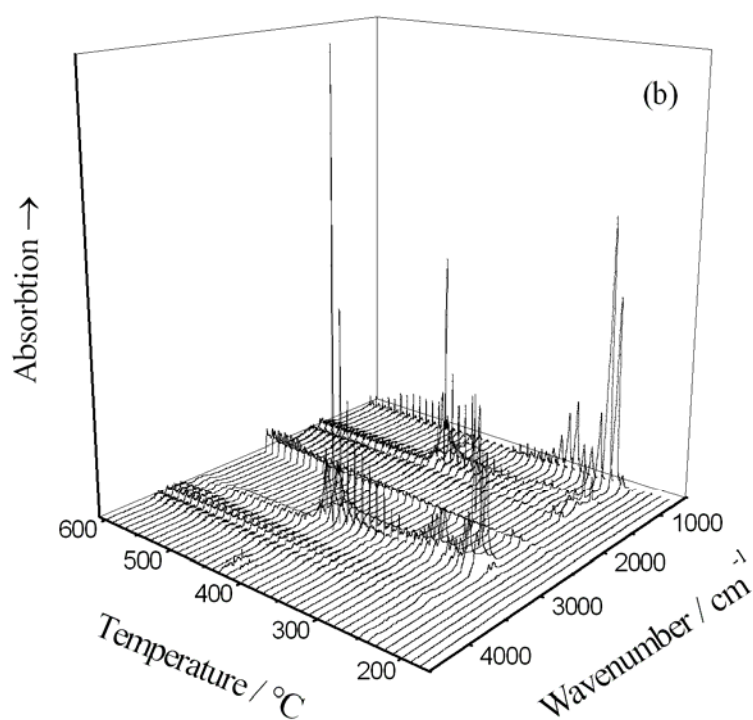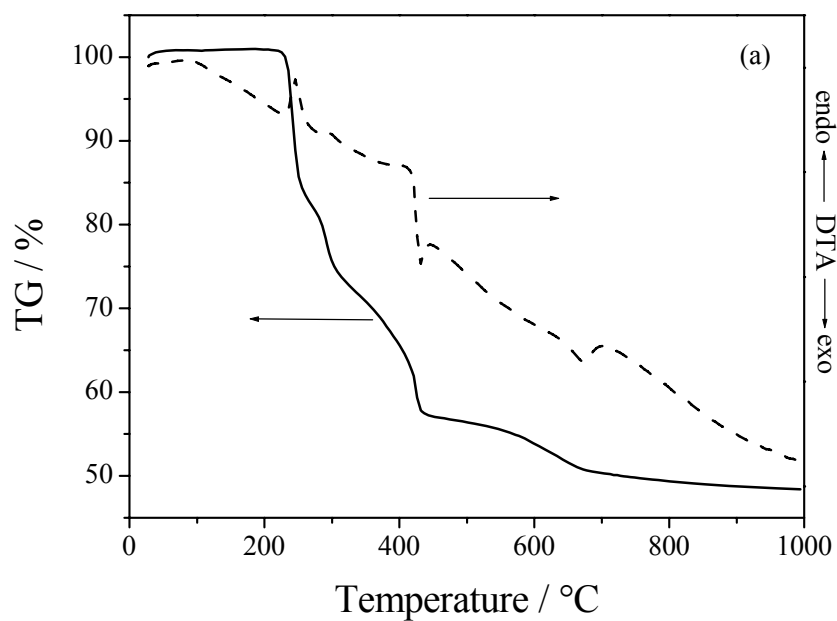
Fig. 3-1: Thermogravimetric analysis of the Ru–Sn bimetallic coordination polymer (no hydrate water) under N$_2$ (a) at a heating rate of 5 K min^{-1}, and the corresponding time-resolved IR spectra (b).
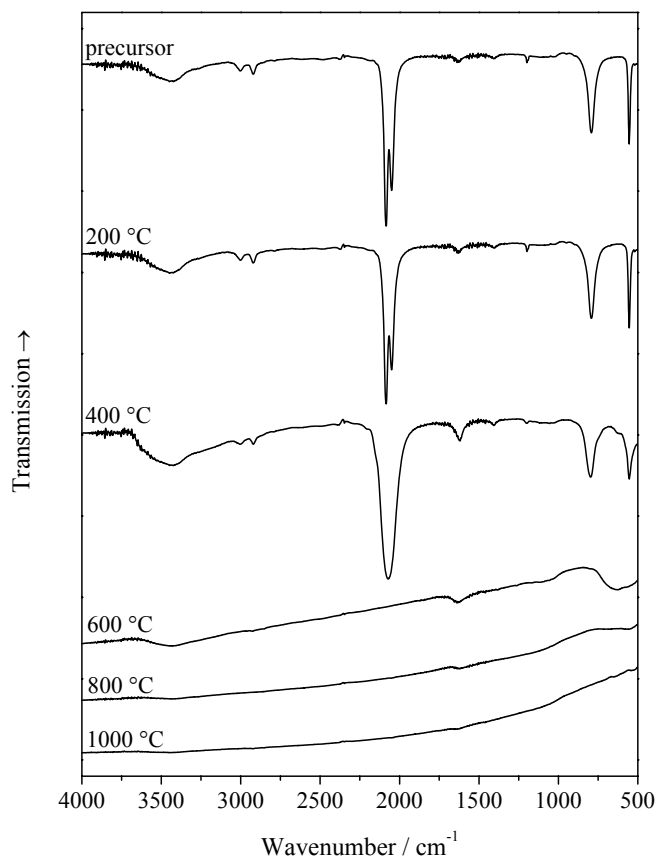
Fig. 3-2: IR spectra of the Ru–Sn coordination polymer (dihydrate) and its solid thermolysis products obtained under N$_2$ at different temperatures.

The Ru–Sn coordination polymer and the corresponding solid thermolysis products at different temperatures in nitrogen were studied by ex-situ IR spectroscopy. Fig. 3-2 shows the characteristic cyanide band at 2099/2067 cm^{-1} (at smaller wavenumber than the gaseous fragments due to the bridging of two metal centres) and the typical C–H bands in Me$_3$Sn at 2998/2920 cm^{-1} as a function of the thermolysis temperature. The spectrum of the Ru–Sn complex exhibited a sharp cyanide doublet, which is due to the high crystallinity of the complex. The doublet disappeared after thermolysis at 400 °C and a broad peak appeared in the same region (approx. 2080 cm^{-1}). The crystallinity of the compound obviously decreased upon thermal treatment. However, the cyanide group was still present at 400 °C. The bands for Me$_3$Sn at 2998/2920 cm^{-1} showed similar changes. Thermolysis at 600 °C resulted in the complete disappearance of both the cyanide and the Me$_3$Sn bands. This indicates clearly that

the thermal decomposition of the Ru–Sn coordination polymer in nitrogen is completed at about 600 °C.
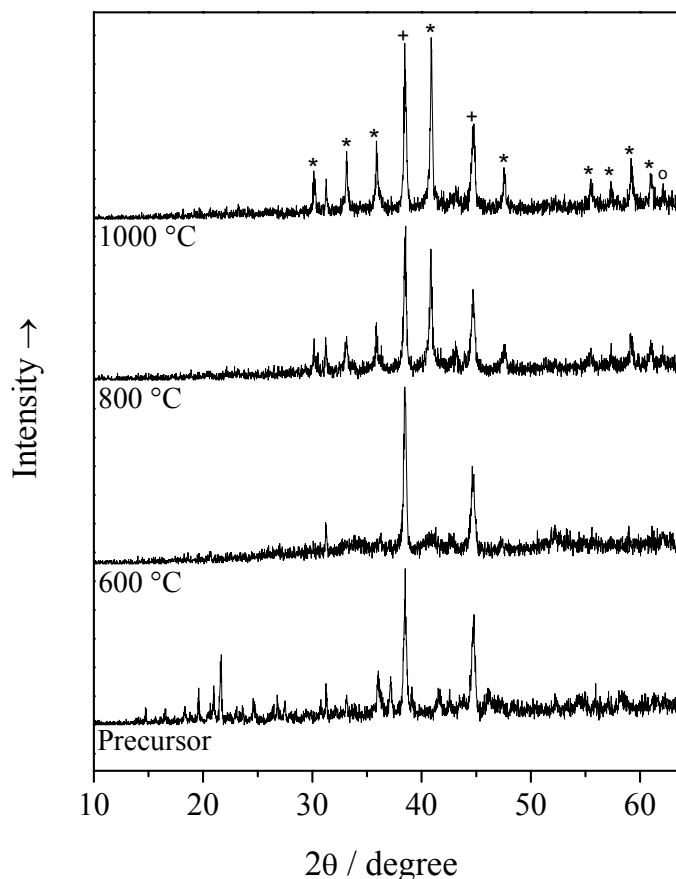

Fig. 3-3: XRD patterns of the Ru–Sn bimetallic complex (no crystal water) and the thermolysis products under N$_2$. The marked peaks correspond to Ru$_3$Sn$_7$ (*) and Sn (°). The peaks marked with (+) result from the aluminum sample holder.

Ru$_3$Sn$_7$ is traditionally prepared by high-temperature treatment, for example, using a radio-frequency oven of Ru and Sn mixtures in vacuum or in inert gases at 1200 °C [93, 94]. A body-centered cubic structure is frequently observed [93-97]. The X-ray diffraction pattern shown in Fig. 3-3 clearly demonstrated the presence of Ru$_3$Sn$_7$ after the thermolysis of the coordination polymer in nitrogen being finished at 600 °C. Elemental Sn was also present in traces. It was furthermore found that prolonged annealing at 1000 °C led to a considerable decrease in the crystallinity of Ru$_3$Sn$_7$ and to the formation of a new, as yet unidentified phase. This indicates

that there is a window in time and temperature that must be kept when Ru$_3$Sn$_7$ is to be quantitatively prepared.

(a)　　　　　　　　　　　　　　　　　(b)

(c)　　　　　　　　　　　　　　　　　(d)
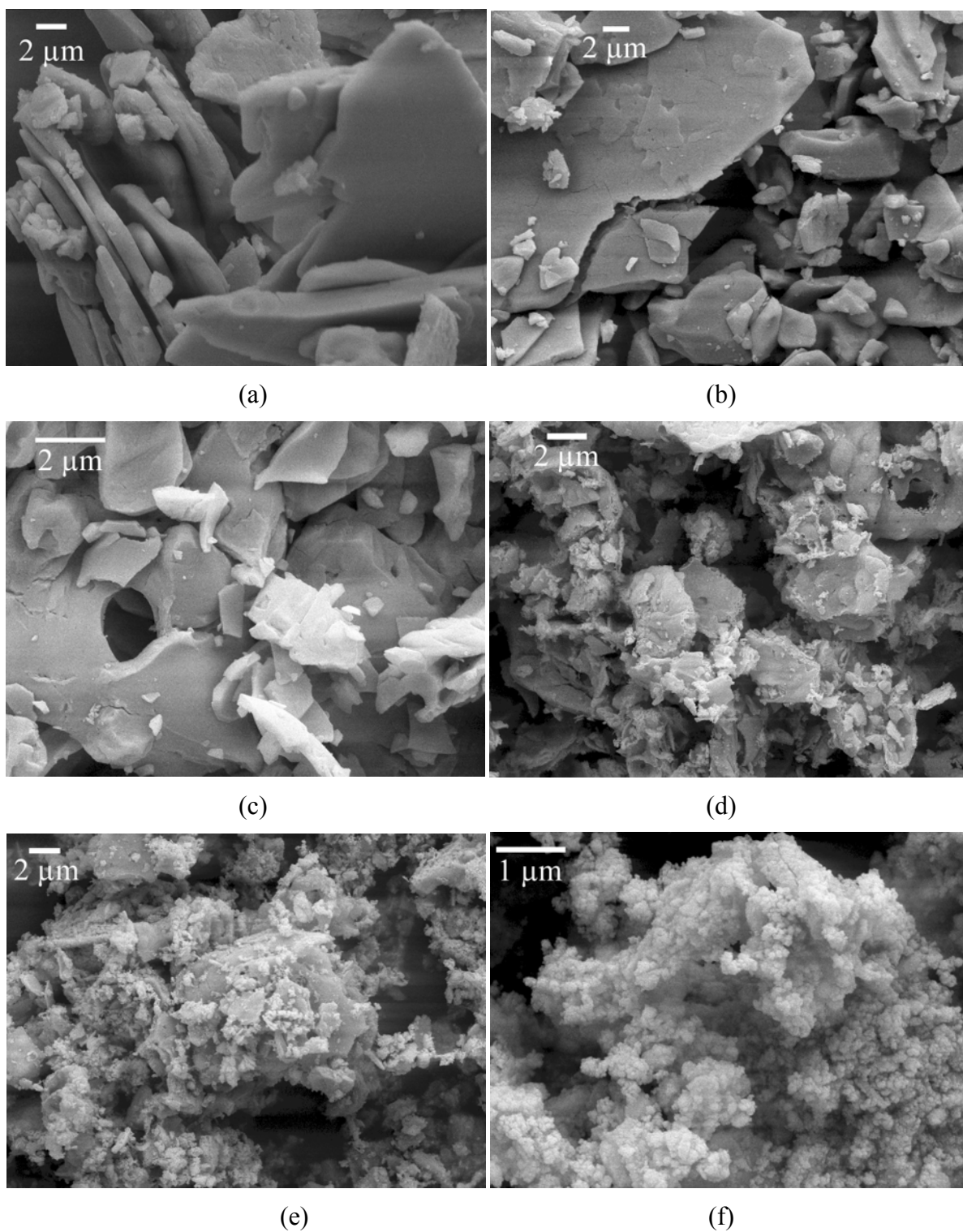
(e)　　　　　　　　　　　　　　　　　(f)

Fig. 3-4: SEM images of the original coordination polymer (dihydrate; a), and its thermolysis products under nitrogen at 200 °C (b), 400 °C (c), 600 °C (d), 800 °C (e) and 1000 °C (f).

The morphology of the Ru–Sn coordination polymer and the thermolysis products under N$_2$ were studied by scanning electron microscopy (Fig. 3-4). The initial coordination polymer crystallized as micrometer-sized platelets. The crystals were destroyed after thermal treatment at 600 °C in nitrogen. Thermolysis at 1000 °C resulted in fine nanoparticles of Ru$_3$Sn$_7$. Ru$_3$Sn$_7$ has a peritectic melting point of 1235 °C [27], therefore melting or sintering can probably be excluded.

3.3.2 Thermolysis under oxidizing conditions[*]

Two well-defined steps were seen in the thermogravimetric curve under oxygen (Fig. 3-5 a). The first sharp step accompanied with a loss of 18 wt% at around 210 °C is associated with the detection of evolved hydrocarbons (C–H; 3016 cm^{-1}), cyanides (CN; 2343 cm^{-1}), carbon dioxide (C=O; 2360 cm^{-1}, 2312 cm^{-1} and 671 cm^{-1}) and water (O–H; 3735 cm^{-1}, 1745 cm^{-1}) (Fig. 3-5 b). The second step with a loss of about 1.2 wt% up to around 400 °C resulted from the combustion of residual carbon under release of carbon dioxide. The total weight loss of 19.2 % from TG results is in good agreement with the theoretical value of 19.3 %, assuming that metal oxides are the final thermolysis product (4 SnO$_2$ + RuO$_2$).

The thermolysis on the preparative scale under air at 600 °C gave the mixed oxide (Sn, Ru)O$_2$, as confirmed by the corresponding XRD pattern (Fig. 3-6). The thermal decomposition of the complex was completed at 600 °C in air. However, the crystallinity changed remarkably with increasing temperature. A semi-quantitative estimation of the crystallite size using the Scherrer equation [98] gave domain sizes of 4–6 nm (230 °C; full width at half maximum of peaks [FWHM] 1.4–2.4° 2θ), 7 nm (450 °C; FWHM 1.2° 2θ), and 7–8 nm (600 °C; FWHM 1.05–1.2° 2θ). At 1000 °C, the peak width (FWHM 0.17° 2θ) was still above the instrumental resolution limit (FWHM 0.10° 2θ), indicating a crystallite size of about 48 nm. The (110), (101), and (211) peaks were used and the results were averaged. A splitting of the diffraction peaks for this mixed crystal phase into those of pure SnO$_2$ and RuO$_2$ was never observed, therefore we assumed a true miscibility in the solid state and interpreted the diffraction peak

---

[*] This part was done in cooperation with Mr. Rainer Weiss, Essen.

broadening as a domain size effect. The maximum of the peaks for the mixed crystals were between those of pure SnO$_2$ and RuO$_2$, but closer to SnO$_2$ due to its higher content.
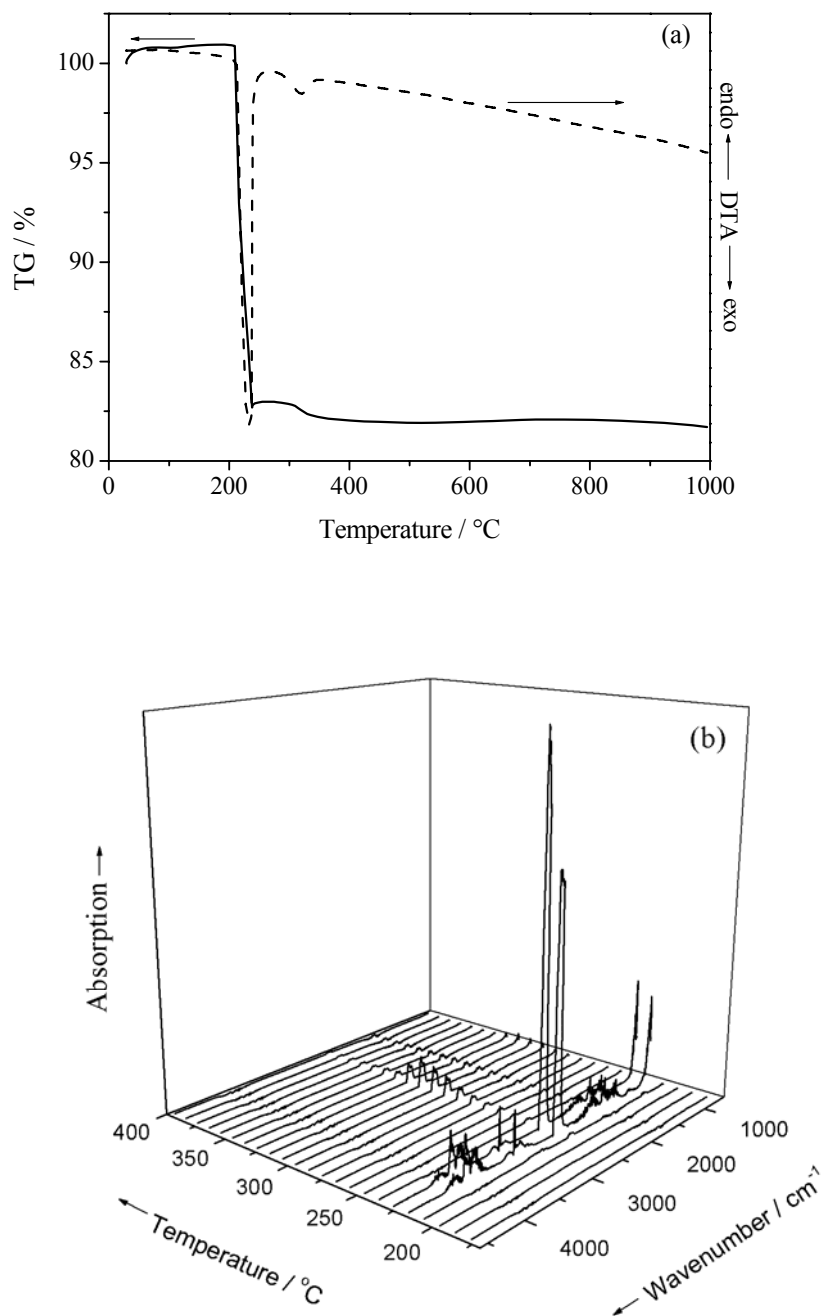

Fig. 3-5: Thermogravimetric analyses of the Ru–Sn bimetallic coordination polymer (no hydrate water) under air (a) at a heating rate of 5 K min^{-1}, and the corresponding time-resolved IR spectra (b).
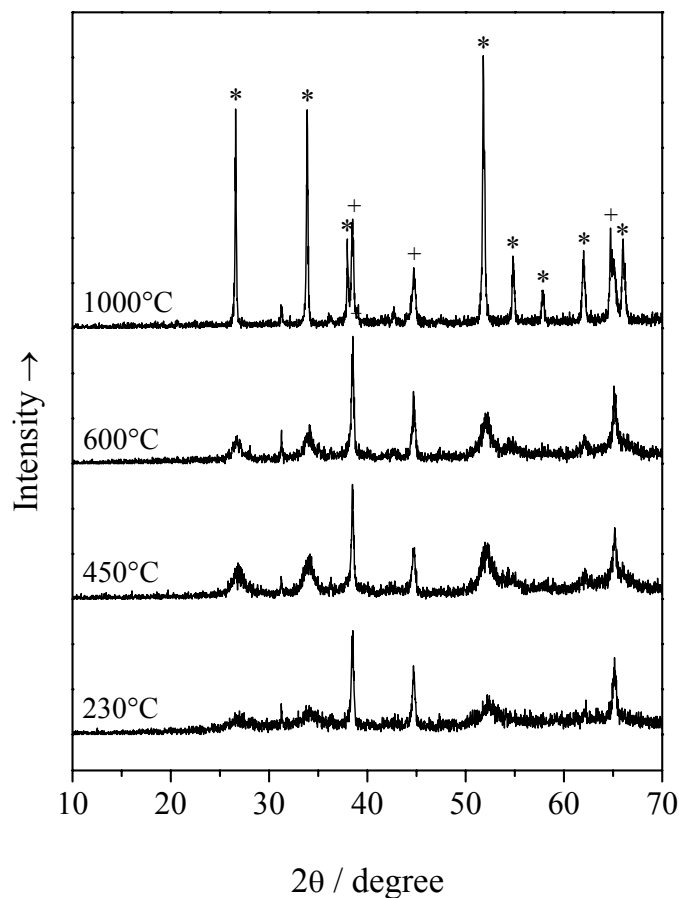
Fig. 3-6: XRD patterns of (Sn,Ru)O$_2$ thermolyzed under air. The marked peaks (*) correspond to (Sn,Ru)O$_2$ mixed crystals. The peaks marked with (+) result from the aluminum sample holder.

The thermolysis products in air were porous blocks as shown in Fig. 3-7 C. N or H was not detected by elemental analysis or energy-dispersive X-ray spectrometry (EDX), which confirmed that the decomposition of the coordination polymer was complete in air at 450 °C. At 1000 °C, the initially porous blocks disassembled into sub-micrometer-sized crystallites. The elemental analysis by EDX gave molar ratios of Ru : Sn of 1 : 4 (230, 400, and 600 °C) and 1 : 62 (1000 °C). At 1000 °C, ruthenium had almost disappeared. It was assumed that Ru was released as a volatile oxide (RuO$_2$ or RuO$_4$) from the solid phase under these conditions. This led to a porous structure (Fig. 3-7 D), where sub-micrometer-sized spherical particles preserved the initial crystallite morphology. Fig. 3-5 a shows a slow but continuous weight loss above 900 °C that we attribute to this loss of ruthenium. By a control experiment where a

sample was heated in the thermobalance to 1000 °C and held at that temperature for 4.5 h, a continuous weight loss was also observed. However, this did not reach the theoretical value of 15.0 wt% for complete loss of RuO$_2$. It is therefore assumed that ruthenium primarily escapes from the sample surface and that EDX as a surface-sensitive tool mainly detects ruthenium depleted regions.
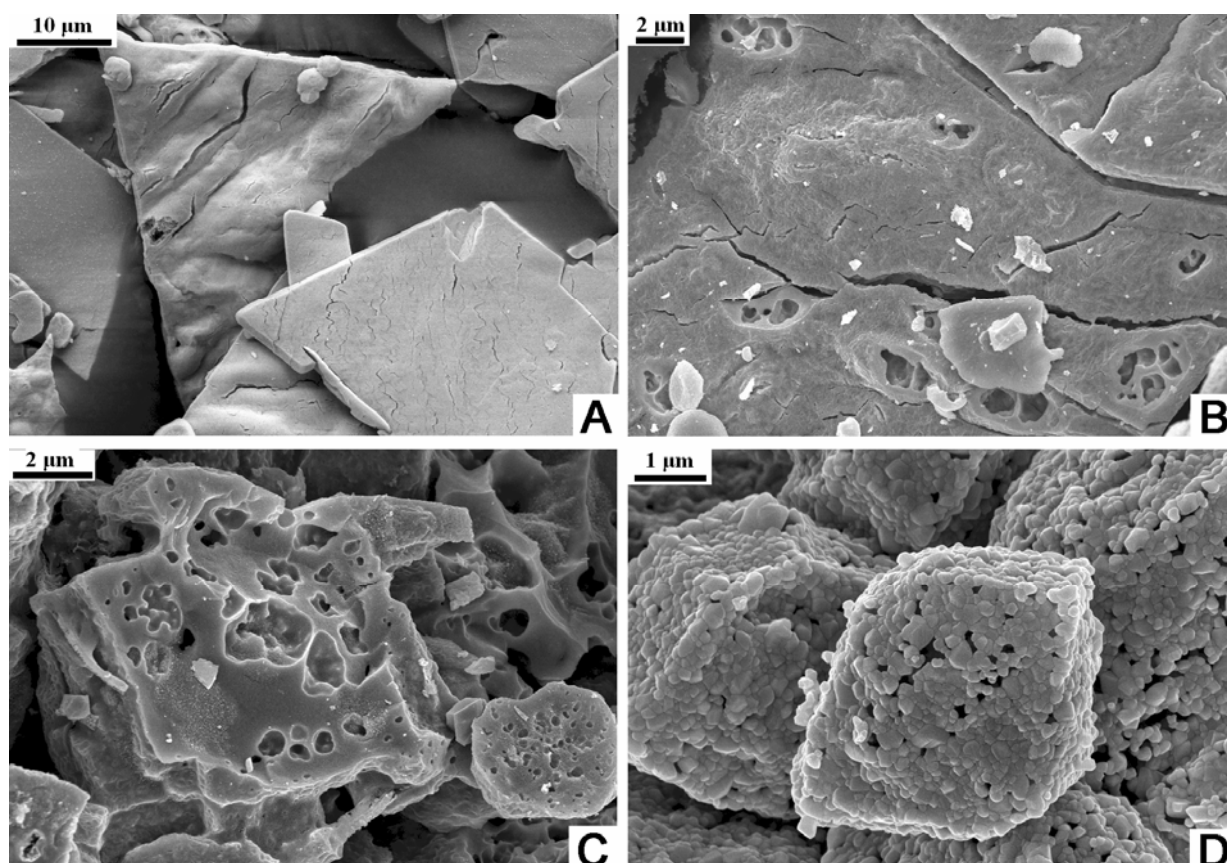

Fig. 3-7: SEM images of the thermolysis product of the coordination polymer in air at 230 °C (A), 450 °C (B), 600 °C (C), and 1000 °C (D).

SnO$_2$ and RuO$_2$ are isostructural. They crystallize in the tetragonal space group $P4_2/mnm$ with unit cell lengths of a = 4.7342/4.4919 Å and c = 3.1871/3.1066 Å (SnO$_2$/RuO$_2$) [99, 100]. This explains why only one set of reflections in the XRD for the intermediates was observed (Fig. 3-6), i.e. mixed crystals were obtained [91, 101]. There was a slight shift in the peak positions of (Sn,Ru)O$_2$ to smaller values with increasing temperature that it was ascribed to the loss of ruthenium and correspondingly to a unit cell expansion (Vegard's rule).

3.4 Conclusions

The thermolysis of the coordination polymer tetrakis(trimethyltin)hexacyanoruthenate(II), ((CH$_3$)$_3$Sn)$_4$Ru(CN)$_6$ was studied in inert and oxidative atmosphere. Ru$_3$Sn$_7$ was almost quantitatively formed after thermolysis in nitrogen whereas the mixed oxide (Sn,Ru)O$_2$ was formed in air. Both compounds can be obtained in a nanocrystalline state if the reaction conditions are chosen properly. This underscores the potential of this precursor method to prepare compounds away from the thermodynamic equilibrium, i.e. with a high specific surface.

4 Copper/zinc oxide nanocomposites: the controlled thermolysis of Zn[Cu(CN)₃]

4.1 Introduction

Copper–zinc oxide mixtures can be obtained in a variety of morphologies, including thin films [102], nanowires [103] and nanoparticles [104]. High-surface area copper/zinc oxide is an active catalyst for methanol synthesis, water-gas shift reactions, and various hydrogenations [105]. It is widely accepted that zinc oxide can improve the dispersion of copper and thereby the catalytic activities [106]. Copper–zinc oxide nanocomposites are usually prepared by co-precipitation from aqueous solutions. Typically, a mixed solution of copper and zinc salts (usually nitrates or acetates) is prepared and the precipitation of both carbonates is induced by addition of sodium or ammonium carbonate whilst stirring, followed by drying and calcinations [55, 107-109]. The particle size and crystallinity of the products can be adjusted by the pH, the concentration, the stirring rate, the duration of precipitation and aging, and the calcination conditions [57]. Pollard et al. [105] used the minerals georgeite [$Cu_5(CO_3)_3(OH)_4\cdot 6\ H_2O$] and azurite [$Cu_3(CO_3)_2(OH)_2$] as precursors for copper–zinc mixed oxides. Recently, a nonaqueous organometallic route was developed by Hambrock et al. [110] and uniform copper–zinc nanoparticles were obtained. They used $Cu[OCH(Me)CH_2NMe_2]_2$ and Et_2Zn as precursors. The thermolysis was carried out in the coordinating solvent hexadecylamine at elevated temperatures and nano-scale colloidal copper–zinc systems with different zinc contents were obtained. Zhou et al. [103] prepared copper–zinc nanowires by heating CuI_2 and ZnI_2 in a dynamic oxygen atmosphere. A self-catalysed vapour-liquid-solid growth mechanism was suggested.

Polymeric metal cyanides represent a homogeneous mixture of the individual metals on the atomic length scale. The heterogeneous mixing of individual compounds is therefore avoided. The controlled thermolysis of these compounds can be carried out at comparatively low temperature due to the presence of a suitable organic leaving group, i. e. the cyanide in the precursors. A higher temperature is usually required in conventional syntheses to achieve a sufficiently fast diffusion. The composition as well as the crystal structure of the bimetallic Fe–Sn and Ru–Sn composites can be fine-tuned by the thermolysis conditions such as time,

temperature and atmosphere [80, 81, 111]. Such systems are suitable precursors for the preparation of bimetallic nanocomposites that incorporate the initially blended metals.

A continuous overflow method was used for the preparation of calcium phosphate nanoparticles from solution [112]. The particle size, morphology and crystallinity can be adjusted by the process parameters, mainly the residence time (the flow rate of the solutions), and the concentration of the solutions. It was therefore the aim of this work to prepare a suitable cyanide precursor for the Cu/ZnO system and to control its morphology by different crystallisation methods. Thereby, the properties of the final product should be adjustable [38, 41, 113].

4.2 Experimental

In the batch precipitation method (Fig. 4-1a), $[Zn(CN)_4]^{2-}$ was prepared by mixing aqueous solutions of zinc sulphate and potassium cyanide. Copper(II) sulphate was then added during stirring and copper zinc cyanide was obtained as precipitate.

In the continuous overflow precipitation method (Fig. 4-1b), the aqueous solutions of $K_2[Zn(CN)_4]$ and $CuSO_4$ were pumped at different flow rates (giving different residence times) into a stirred precipitation vessel at room temperature. The overflowing suspension was immediately filtered. The precipitate was dried overnight under air at room temperature and stored in sealed vials until further characterization. All reagents were used in stoichiometric amounts.

The controlled thermolysis of the cyanides prepared by the batch precipitation method was carried out in a horizontal quartz tube reactor with an inner diameter of 30 mm. The thermal decomposition was carried out under air at 300, 400 and 500 °C for 3 hours. The mixed oxides were then reduced under hydrogen/nitrogen (molar ratio 5:95) at 250 °C for 3 hours. The thermolysis of the cyanide precursor was also tested in a fluidized-bed reactor at a temperature of up to 400 °C under air. In addition, shock pyrolysis in a drop-tube reactor at 1000 °C under air was studied.

The Cu-Zn cyanide synthesized by the continuous overflow method was thermolyzed under air at 300 °C for 3 hours in the quartz tube reactor.
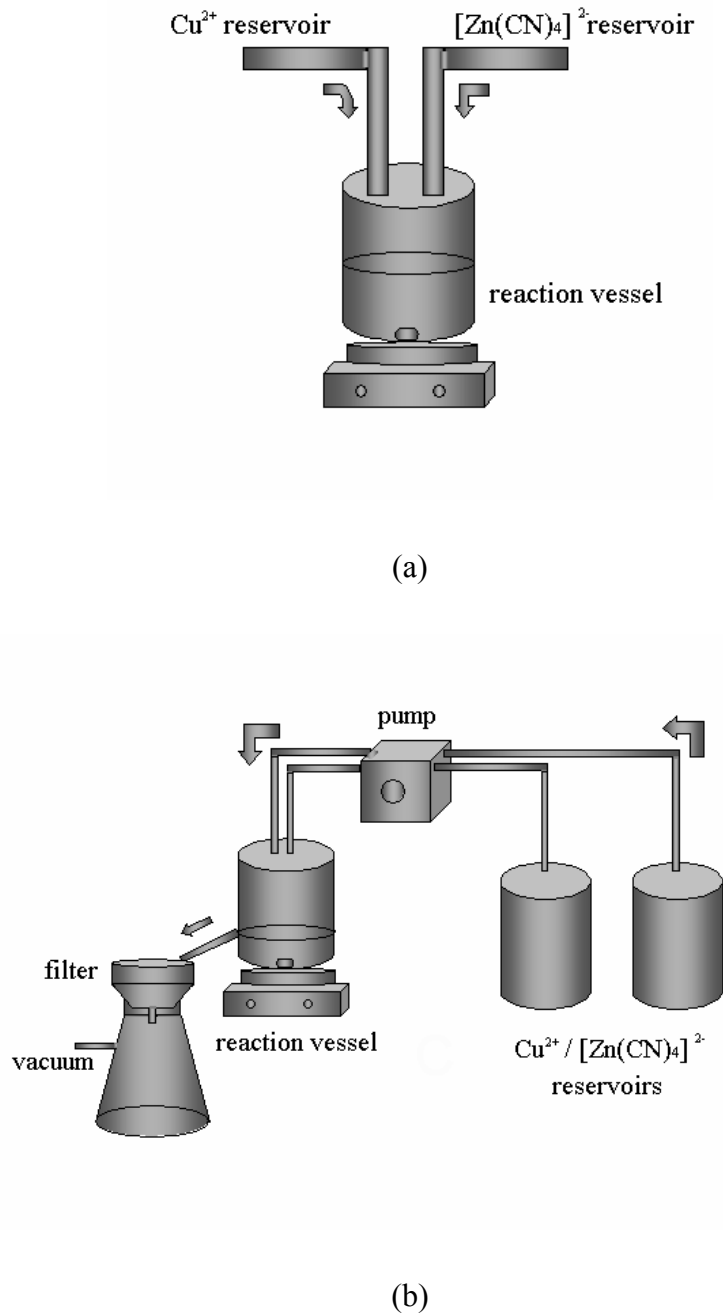
(a)

(b)

Fig. 4-1: Schematic set-ups of the batch precipitation method (a) and of the continuous overflow method (b).

Two different methods were employed for the preparation of the $CuO/ZnO/Al_2O_3$ samples, as described below:

(1) Using Al_2O_3 powders as Al_2O_3 source. A predetermined amount of Al_2O_3 powder was added to an aqueous solution of copper(II) sulphate, corresponding to different Cu:Al ratios.

$[Zn(CN)_4]^{2-}$, prepared by mixing aqueous solutions of zinc sulphate and potassium cyanide, was then added during stirring. $Zn[Cu(CN)_3]/Al_2O_3$ was obtained as precipitate. After thermolysis of the complex under air at 300 °C for 3 hours, the ternary oxide of $CuO/ZnO/Al_2O_3$ was obtained.

(2) Using $Al(OH)_3$ as Al_2O_3 source. $Al(NO_3)_3 \cdot 9 H_2O$ was dissolved in water to give a clear solution. The solution changed to a sol with white precipitates when the pH of the solution was adjusted to 7 by adding NaOH solution. The aqueous solutions of $K_2[Zn(CN)_4]$ and $CuSO_4$ were then added simultaneously to form the co-precipitate of $Zn[Cu(CN)_3]/Al(OH)_3$. The oxide product $CuO/ZnO/Al_2O_3$ was obtained by thermolysis of the co-precipitate under air at 300 °C for 3 hours.

The combined application of thermogravimetry and infrared spectroscopy (TG-IR) was carried out with a Netzsch STA 409 TG-DTA/DSC apparatus connected to a Bruker Vertex 70 infrared system for in-situ gas analysis. Samples were heated from room temperature to 1000°C at a rate of 5 K min^{-1} under O_2 at a flow rate of 50 mL min^{-1}. The evolved gases were monitored in-situ by infrared spectroscopy (IR). The infrared spectra were all corrected for background absorption. Background spectra were recorded at room temperature before the start of the experiment with the cavity filled by flow gas. Thermogravimetry-mass spectroscopy (TG-MS) was carried out with a TGA 7 Perkin–Elmer thermobalance coupled to a quadruple mass spectrometer (OmniStarTM, Pfeiffer). The sample was heated with 10 K min^{-1} under synthetic air (20.5 vol% oxygen in nitrogen) at a flow rate of 100 mL min^{-1}.

X-ray diffraction was carried out at room temperature at beamline B2 at the Hamburger Synchrotronstrahlungslabor (HASYLAB) at Deutsches Elektronen Synchrotron (DESY), as well as with a Siemens D5000 system with Cu $K\alpha$ radiation (1.54178 Å; Bragg–Brentano geometry). The morphology of the thermolysis products was studied by scanning electron microscopy (LEO Gemini 1530). The structure of the resulting Cu/ZnO was studied by transmission electron microscopy (TEM) with a Philips CM 200 FEG instrument. The specific surface area of the Cu/ZnO and CuO/ZnO samples was determined by nitrogen physisorption at 77 K (BET method). The samples were out-gassed at 573 K until the pressure was lower than 500 Pa.

Extended X-ray absorption fine structure (EXAFS) spectroscopy was carried out at beamline E4 at HASYLAB/DESY. The programs SPLINE and XFIT [114] were used for quantitative data

evaluation. Theoretical standards were computed with the program FEFF 6.01a [115]. The amplitude reduction factor S_o^2 was fixed to 1. Variation parameters were the bond lengths, the coordination numbers, the Debye-Waller factors (σ^2), and the zero-energy correction (E_o).

The catalytic activities of Cu/ZnO samples were measured using a single-tube reactor[*] as follows: 100 mg of the sample (sieve fraction 250-355 μm) were placed in a fixed-bed glass-lined U-tube reactor. The reduction was performed under flowing diluted H_2 (2 vol% H_2 in He) by increasing the temperature up to 448 K with 1 K min^{-1} and maintaining for 14 h. To ensure complete reduction, the temperature was then increased to 513 K and the sample was treated with pure H_2. The methanol formation activity was measured at 493 K under atmospheric pressure. The feed gas consisted of 72 vol% H_2, 10 vol% CO, 4 vol% CO_2 and 14 vol% He. Gases of the highest available purity (>99.9995 vol%) were used. The online analysis of the products was performed by a previously calibrated quadruple mass spectrometer (Balzers GAM 422). The active surface area of Cu was determined by N_2O reactive frontal chromatography at 300 K [116].
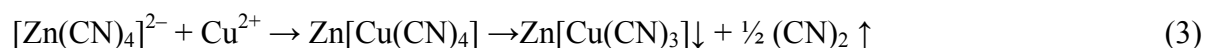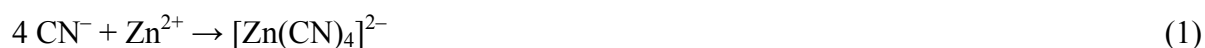
Catalytic measurements of $CuO/ZnO/Al_2O_3$ samples were performed in a high-throughput 49-parallel channel reactor[†] [117]. The catalyst (100 mg diluted with 200 mg quartz per well) was placed in a sample holder consisting of a stainless steel cartridge closed at the bottom by a stainless-steel sinter metal frit. Prior to the catalytic measurements the catalysts were reduced with H_2 at 518 K following the procedure for the commercial benchmark catalyst ICI Katalco 51-8. Before measuring the catalytic activity, all samples were equilibrated for 3 h (reaction pressure 4.5 MPa, reaction temperature 518 K, analytic flow 20 mL min^{-1}). The reaction gas consisted of 70 vol% H_2, 24 vol% CO, and 6 vol% CO_2. A double GC system (HP GC 6890) equipped with a methanizer FID was used for online gas analysis. Oxo-product separation (H_3COH, $HCOOCH_3$, $H_3CCOOCH_3$, H_3CCH_2OH) was carried out on a SuppelcoWAX 0.53 mm column and CO, CO_2 and CH_4 were separated on a Carboxen 1006 column. Methanol productivities for all measured samples were compared to the productivity of the industrial benchmark catalyst ICI Katalco 51-8.

---

[*] Performed in the Laboratory of Industrial Chemistry, Ruhr University Bochum.

[†] Carried out in Max-Planck Institute of Coal Research, Mühlheim.

4.3 Results and discussion

For the preparation of the Cu–Zn cyanide complex, there are two possible routes as shown in Equations (1), (2) and (3). In both cases, tetrahedral $[Zn(CN)_4]^{2-}$ is formed in the first step (1). Subsequently, both reactions (2) and (3) are likely to occur. Because the stability constant of $[Zn(CN)_4]^{2-}$ (4×10^{19} M^{-4}) [118] is smaller than that of $[Cu(CN)_4]^{2-}$ (1×10^{27} M^{-4}) [119], the latter compound is preferred in equilibrium. However, the oxidation state of $[Cu(CN)_4]^{2-}$ is not stable leading to a reduction of Cu^{II} to Cu^{I}. Thus, a transient state of $[Cu(CN)_3]^{2-}$ can be assumed, followed by the formation of $Zn[Cu(CN)_3]$ as precipitate and the release of $(CN)_2$ into the gas phase.

$$4\ CN^- + Zn^{2+} \rightarrow [Zn(CN)_4]^{2-} \tag{1}$$

$$[Zn(CN)_4]^{2-} + Cu^{2+} \rightarrow Cu[Zn(CN)_4] \downarrow \tag{2}$$

$$[Zn(CN)_4]^{2-} + Cu^{2+} \rightarrow Zn[Cu(CN)_4] \rightarrow Zn[Cu(CN)_3] \downarrow + \tfrac{1}{2}\ (CN)_2 \uparrow \tag{3}$$

4.3.1 Batch-wise preparation and thermolysis

For the Cu–Zn cyanide complex prepared by the batch precipitation method, elemental analysis gave 17.5 wt% C, 20.2 wt% N, 30.3 wt% Cu and 31.2 wt% Zn. This corresponds to a Cu/Zn/CN molar ratio of 1:1:3.1. It was concluded that $Zn[Cu(CN)_3]$ (calcd. 17.4 wt% C, 20.3 wt% N, 30.7 wt% Cu and 31.6 wt% Zn) is the main component of the precipitates and that a small amount of $Cu[Zn(CN)_4]$ (calcd. 20.6 wt% C, 24.0 wt% N, 27.3 wt% Cu and 28.1 wt% Zn) is also present.

The infrared spectra of this complex support this assumption (Fig. 4-2). The strong peak at 2155 cm^{-1} is the contribution of CN groups bound (via carbon) to Cu^{I} [120]. An additional contribution at 2217 cm^{-1} is attributed to CN bound (via carbon) to Zn [121]. It is obvious that $Zn[Cu(CN)_3]$ is dominating in the prepared cyanides due to its high peak intensity in the spectra.
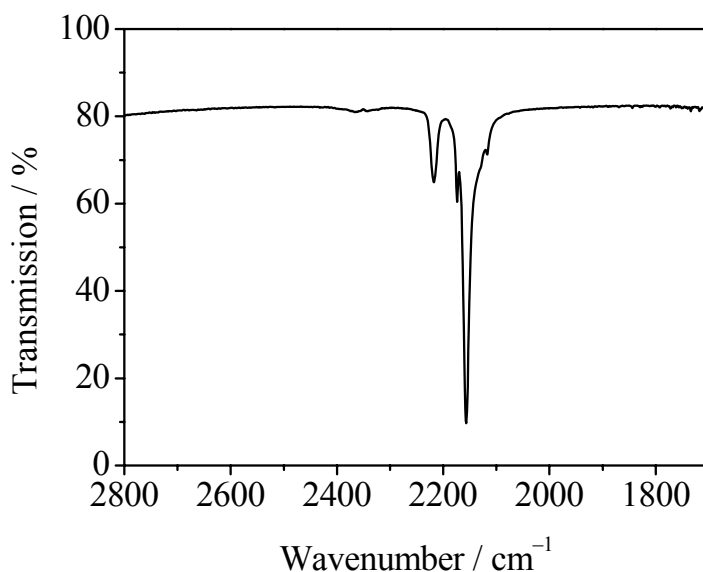
Fig. 4-2: Infrared spectra of Zn[Cu(CN)$_3$], prepared by the batch precipitation method.

EXAFS analysis were performed to investigate the structure of the copper zinc cyanide complex (no single crystals could be obtained). Fig. 4-3 a&b show the Cu K-edge EXAFS raw data and Fourier transform magnitudes (FTs) of the complex Zn[Cu(CN)$_3$]. The nearest neighbors derived from the FTs were fit as 3 carbon atoms at 1.92 Å (Table 4-1, part a). Another carbon atom appeared at a larger distance, at 2.37 Å. This can be ascribed to different Cu–CN bonds [120]. In this case the coordination polyhedron around Cu can be described as a deformed trigonal pyramid with one CN group at a larger distance. The corresponding nitrogen atoms in cyanide appeared at 3.12 Å (3 N) and 3.71 Å (1 N), respectively. The Zn K-edge EXAFS raw data and Fourier transform magnitude of the complex are shown in Fig. 4-3 c&d. As nearest neighbors of zinc, 4 nitrogen atoms are present in a distance of 1.93 Å (Table 4-1, part b). The second peak indicates the corresponding carbon atoms of the cyanide group at 3.22 Å. In both EXAFS spectra (Cu and Zn), a metallic neighbor can be fit in a distance of 5.1 to 5.2 Å. By EXAFS, it cannot be distinguished between a copper neighbor and a zinc neighbor, but the given stoichiometry suggests a network which consists of Cu–C–N–Zn units.
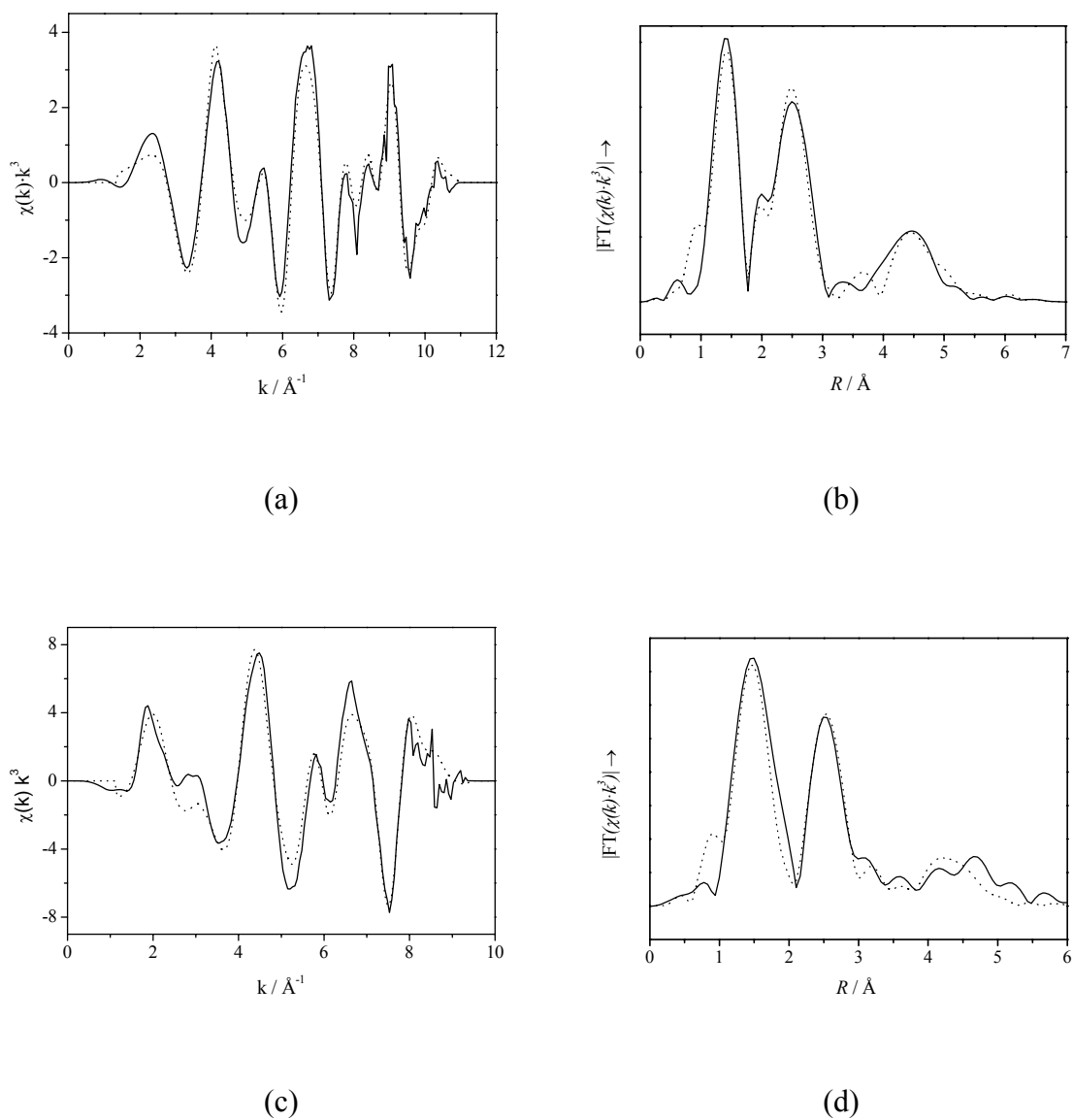
(a)

(b)

(c)

(d)

Fig. 4-3: EXAFS raw data and Fourier transform magnitudes of the Zn[Cu(CN)$_3$] prepared by the batch precipitation method. Solid line: experimental data, dotted line: fit data. Cu K-edge (a, b) and Zn K-edge (c, d).

Table 4-1: Fit parameters for the Cu K-edge (a) and Zn K-edge (b) EXAFS spectra of Zn[Cu(CN)$_3$] prepared by the batch precipitation method.

Zn[Cu(CN)$_3$]	R/Å	N	$\sigma^2 \cdot 10^3$/Å^2
Cu-3 C	1.92	3.1	3.3
Cu-C	2.37	1.0	2.8
Cu-3 N	3.12	3.2	0.1
Cu-N	3.71	1.4	4.2
Cu-4 Zn	5.12	4.2	5.9

(a)

Zn[Cu(CN)$_3$]	R/Å	N	$\sigma^2 \cdot 10^3$/Å^2
Zn-4 N	1.93	4.4	6.6
Zn-4 C	3.22	4.3	3.0
Zn-4 Cu	5.20	4.3	5.8

(b)

The thermolysis of the copper–zinc complex was studied by thermogravimetric analysis coupled with infrared spectroscopy (TG-IR). When heated up under oxygen, the decomposition of the copper–zinc complex started at about 300 °C (Fig. 4-4, part a). Two steps at about 440 °C and 510 °C can be derived from the TG weight loss curve. The weight loss ceased at about 530 °C. At 1000 °C, only CuO/ZnO was present, as shown by XRD. The total weight loss was about 23 %. From the weight loss it can be deduced that the precursor consists of Zn[Cu(CN)$_3$] (a theoretical weight loss of 22.2 % for a complete transformation to CuO/ZnO) rather than Cu[Zn(CN)$_4$] (a theoretical weight loss of 30.9 %). This is in good agreement with the elemental analysis. Two exothermal peaks in the DTA curve correspond to the two steps in the weight loss curve, indicating oxidative combustion.

The infrared spectra in Fig. 4-4 (part b) correspond to the evolved gas phase during heating. The contribution of cyanides (CN, at 2343 cm^{-1}) appeared first. Carbon dioxide (C=O, 2360/2312/671 cm^{-1}) was subsequently released at elevated temperature, showing again the two steps at about 440 °C and 510 °C, indicated by the two maxima in the time-resolved spectra.
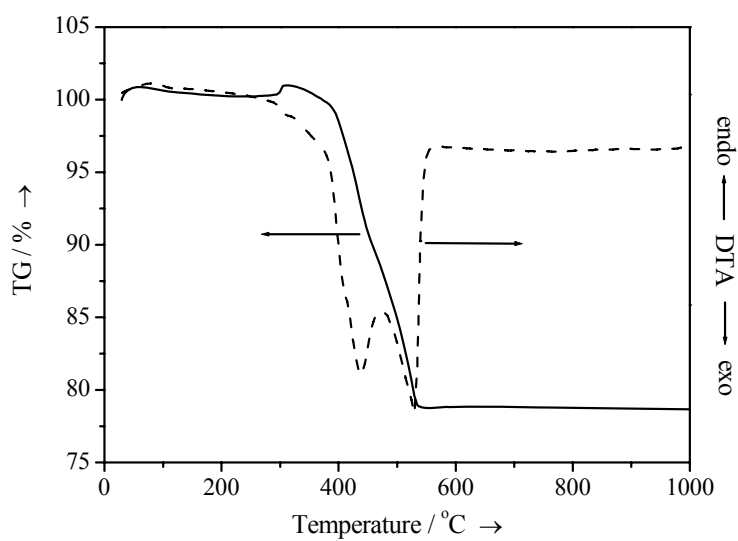
(a)
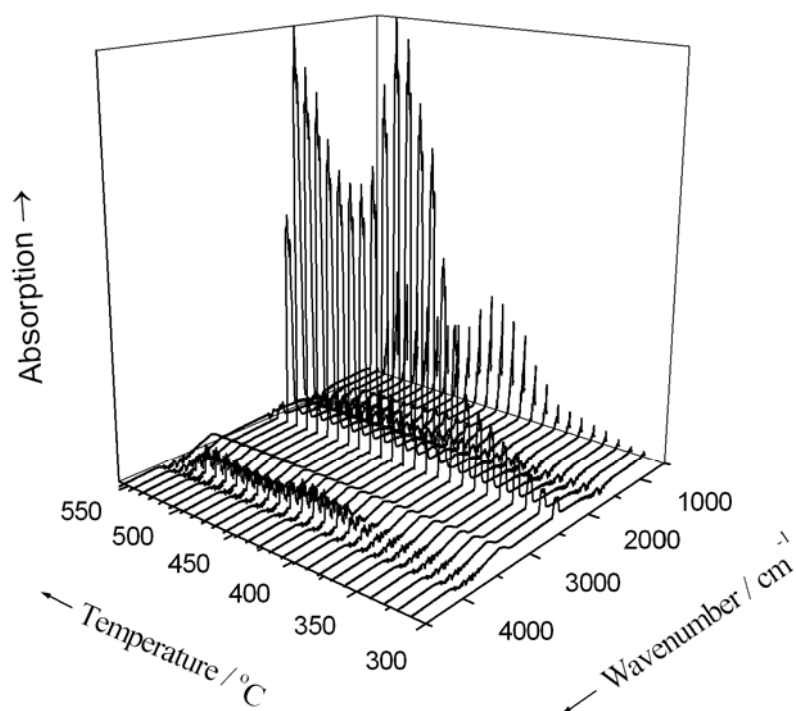
(b)

Fig. 4-4: Thermogravimetric analysis of $Zn[Cu(CN)_3]$ under oxygen (a) and the corresponding time-resolved infrared spectra of the released gases during heating (b) (heating rate 5 K min^{-1}).

Another experiment was carried out with thermogravimetric analysis coupled with mass spectroscopy (TG-MS). Air was used as oxidizing gas and the copper–zinc complex was heated from room temperature to 1000 °C. The weight loss started at about 300 °C and stopped at around 620 °C (Fig. 4-5, part a). The thermolysis was shifted to higher temperature compared with the TG-IR results because oxygen was replaced by air and the heating rate was increased from 5 K min^{-1} to 10 K min^{-1}. The total weight loss was about 24 wt%.

The mass spectra in Fig. 4-5 (part b) clearly show the release of gaseous species. Cyanogen [$(CN)_2$: mass 52] was released at low temperatures in two steps, corresponding to the low intensity of the cyanide peak in the IR spectra. The initial "dip" in the TG curve at around 300°C can be related to a non-oxidative elimination of cyanogen. The release of carbon dioxide, nitrogen monoxide and nitrogen dioxide occurred at higher temperatures in two steps, indicated by two peaks or a broad peak with a shoulder.

The XRD patterns of the thermolysis products under air at different temperatures are shown in Fig. 4-6 (a). Copper oxide and zinc oxide are present. With rising thermolysis temperature, the height of the peaks increased and their width decreased, indicating an increasing particle size (a better crystallinity). The three oxides samples of Fig. 4-6 (a) were then reduced at 250 °C in H_2/N_2 to Cu/ZnO. The effects of the initial thermolysis temperatures under air are also represented in the XRD patterns of the reduced samples (Fig. 4-6 b).

EXAFS analysis was performed to investigate the structure of the oxide mixtures (CuO/ZnO), and of the reduced samples (Cu/ZnO). In the Cu K-edge raw data and FTs of the CuO/ZnO mixture (Fig. 4-7), the shells of Cu–O and Cu–Cu in CuO are clearly present, supporting the X-ray diffraction data (Table 4-2) [122].
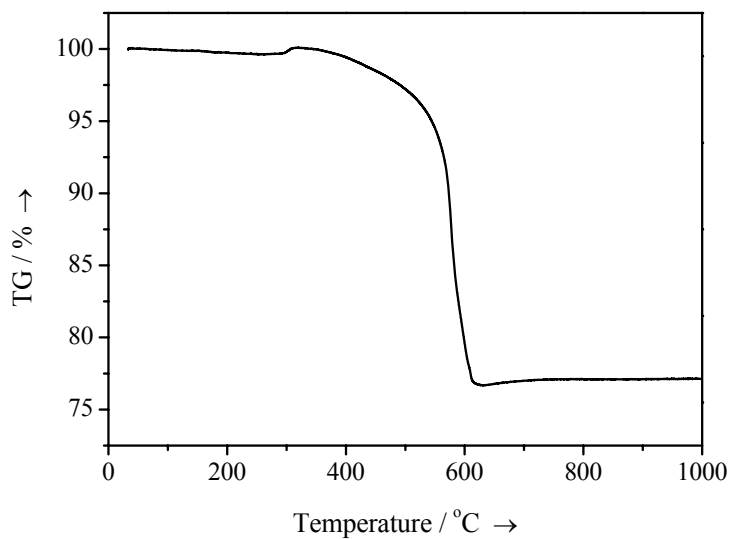
(a)
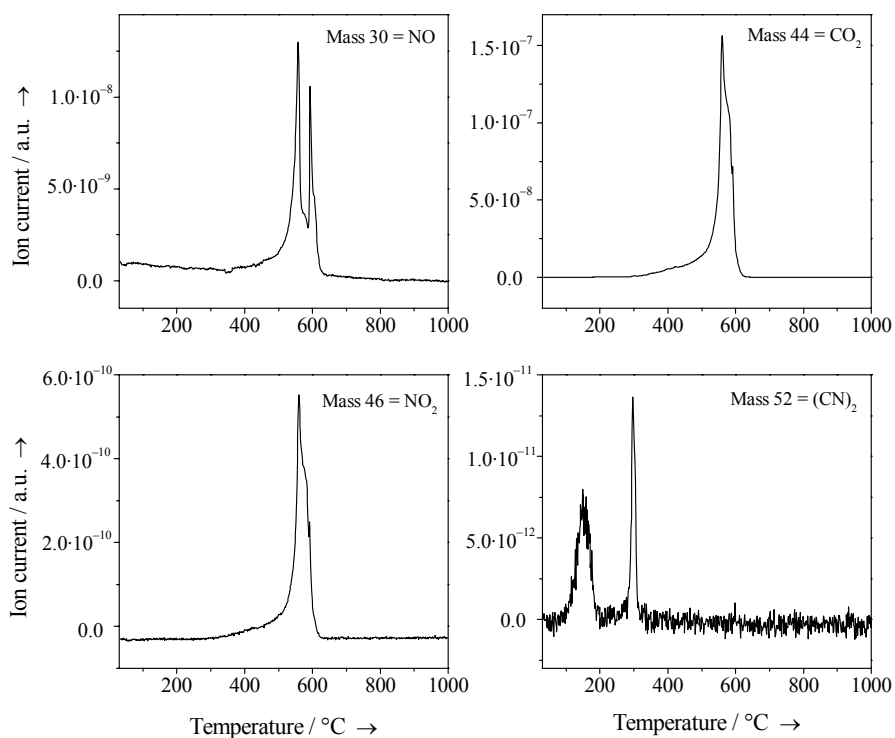
(b)

Fig. 4-5: (a) Thermogravimetric analysis of $Zn[Cu(CN)_3]$ under air, (b) the corresponding time-resolved mass spectra of four different masses in the released gases (heating rate 10 K min^{-1}).
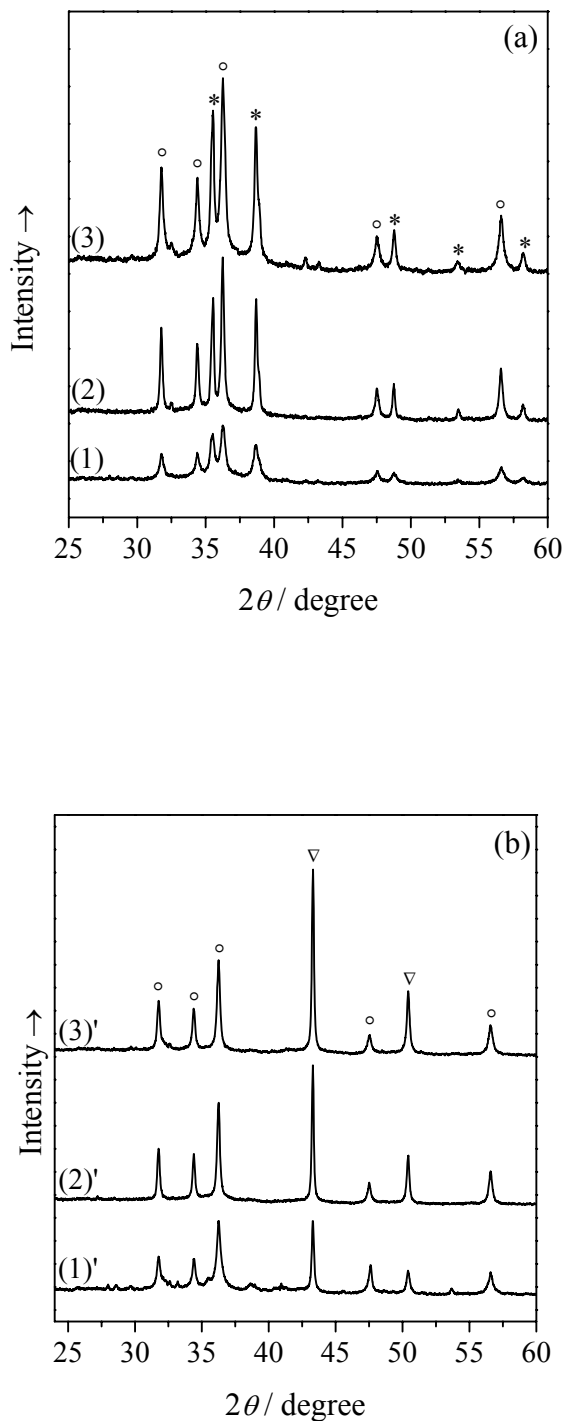
Fig. 4-6: (a) XRD patterns of CuO/ZnO obtained by oxidation of Zn[Cu(CN)₃] at 300 °C (1), 400 °C (2) and 500 °C (3) for 3 hours; (b) XRD patterns of Cu/ZnO obtained by reduction of the corresponding oxide mixtures under H_2/N_2 for 3 hours at 250 °C. The marked peaks orrespond to ZnO (o), CuO (*) and Cu (∇).
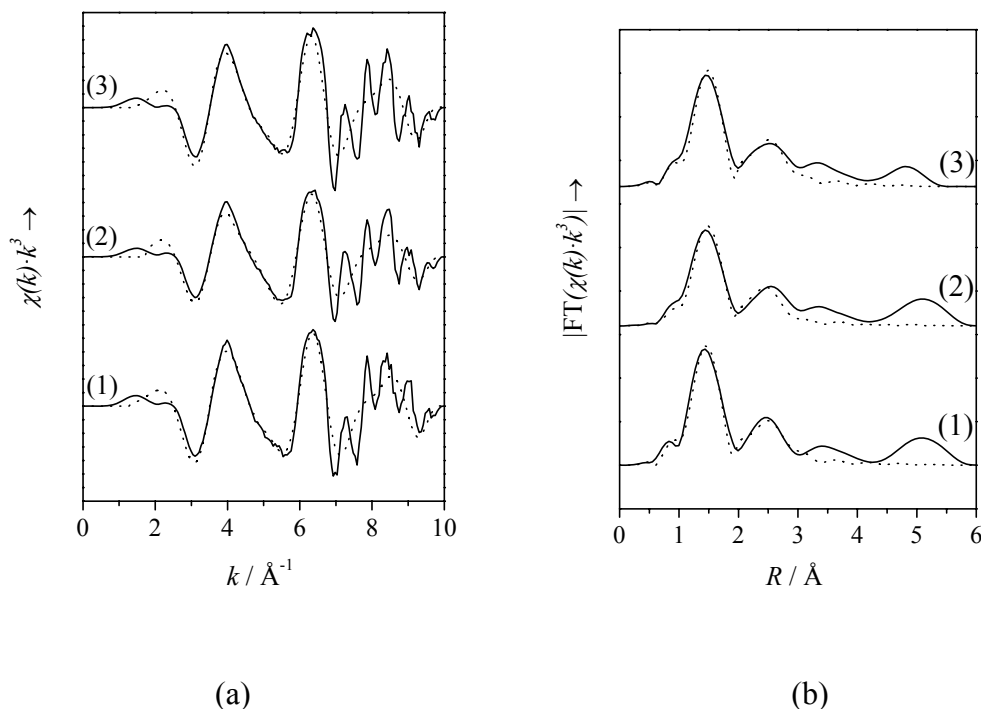
(a)   (b)

Fig. 4-7: Cu K-edge EXAFS raw data (a) and Fourier transform magnitudes (b) of CuO/ZnO obtained by thermolysis of Zn[Cu(CN)$_3$] at 300 °C (1), 400 °C (2) and 500 °C (3) under air for 3 h. Solid line: experimental data, dotted line: fit data.

Table 4-2: Fit parameters for the Cu K-edge EXAFS spectra of CuO/ZnO obtained by thermolysis of Zn[Cu(CN)$_3$] at 300 °C, 400 °C and 500 °C under air for 3 h.

CuO/ZnO	Cu - 4 O			Cu – 8 Cu		
	R /Å	N	$\sigma^2 \cdot 10^3 /Å^2$	R /Å	N	$\sigma^2 \cdot 10^3 /Å^2$
300 °C	1.94	3.9	5.5	2.91	8.4	19.9
400 °C	1.96	3.9	4.0	2.93	8.2	22.9
500 °C	1.96	3.8	5.5	2,94	8.1	23.2

Fig. 4-8 shows the Cu K-edge raw data and FTs of the reduced samples (Cu/ZnO). The Cu–Cu distances of the first shell were in the range of 2.69–2.74 Å (Table 4-3), and compared well to that of the bulk metal (2.56 Å). The coordination numbers were about 12, also in agreement with the cubic close packing of the bulk metal. The second shell of copper was at a distance of about 3.5 Å with a coordination number of 6. The weak peaks at about 1.5 Å may

result from CuO or Cu_2O (in bulk Cu_2O the first coordination number is 2 and the Cu–O distance is 1.84 Å; see also the results for CuO) [123]. Possibly, this is the result of an oxidation of the copper surface due to exposure to air before the EXAFS measurement.

(a)   (b)
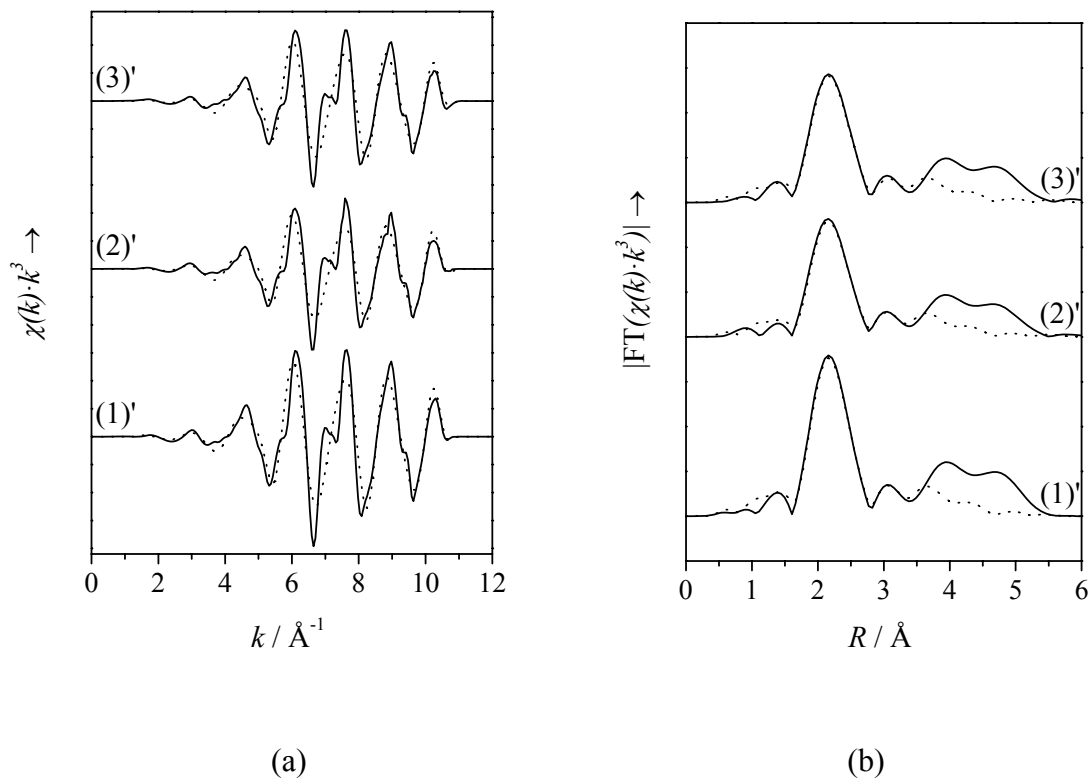
Fig. 4-8: Cu K-edge EXAFS raw data (a) and Fourier transform magnitudes (b) of Cu/ZnO reduced from the above-mentioned thermolysis products under H_2/N_2 at 250 °C for 3 h. Solid line: experimental data, dotted line: fit data.

Table 4-3: Fit parameters for the Cu K-edge EXAFS spectra of Cu/ZnO reduced from the corresponding thermolysis products under H_2/N_2 at 250 °C for 3 h.

	Cu – 12 Cu			Cu – 6 Cu		
Cu/ZnO	R /Å	N	$\sigma^2 \cdot 10^3 / \text{Å}^2$	R /Å	N	$\sigma^2 \cdot 10^3 / \text{Å}^2$
300 °C/250 °C	2.74	11.9	6.5	3.48	6.8	17.9
400 °C/250 °C	2.69	11.9	7.1	3.41	6.5	13.0
500 °C/250 °C	2.74	12.2	6.9	3.49	6.6	17.1

The morphology of the Cu–Zn cyanide complex and the thermolysis products were studied by scanning electron microscopy (Fig. 4-9). The initial complex crystallized as micrometer-scale platelets, which were destroyed by the subsequent thermolysis. The diameter of the agglomerates decreased at higher thermolysis temperatures, in contrast to the crystallite size determined by XRD, which increased with increasing temperatures. However, the macroscopic morphology is not directly related to the internal domain size.
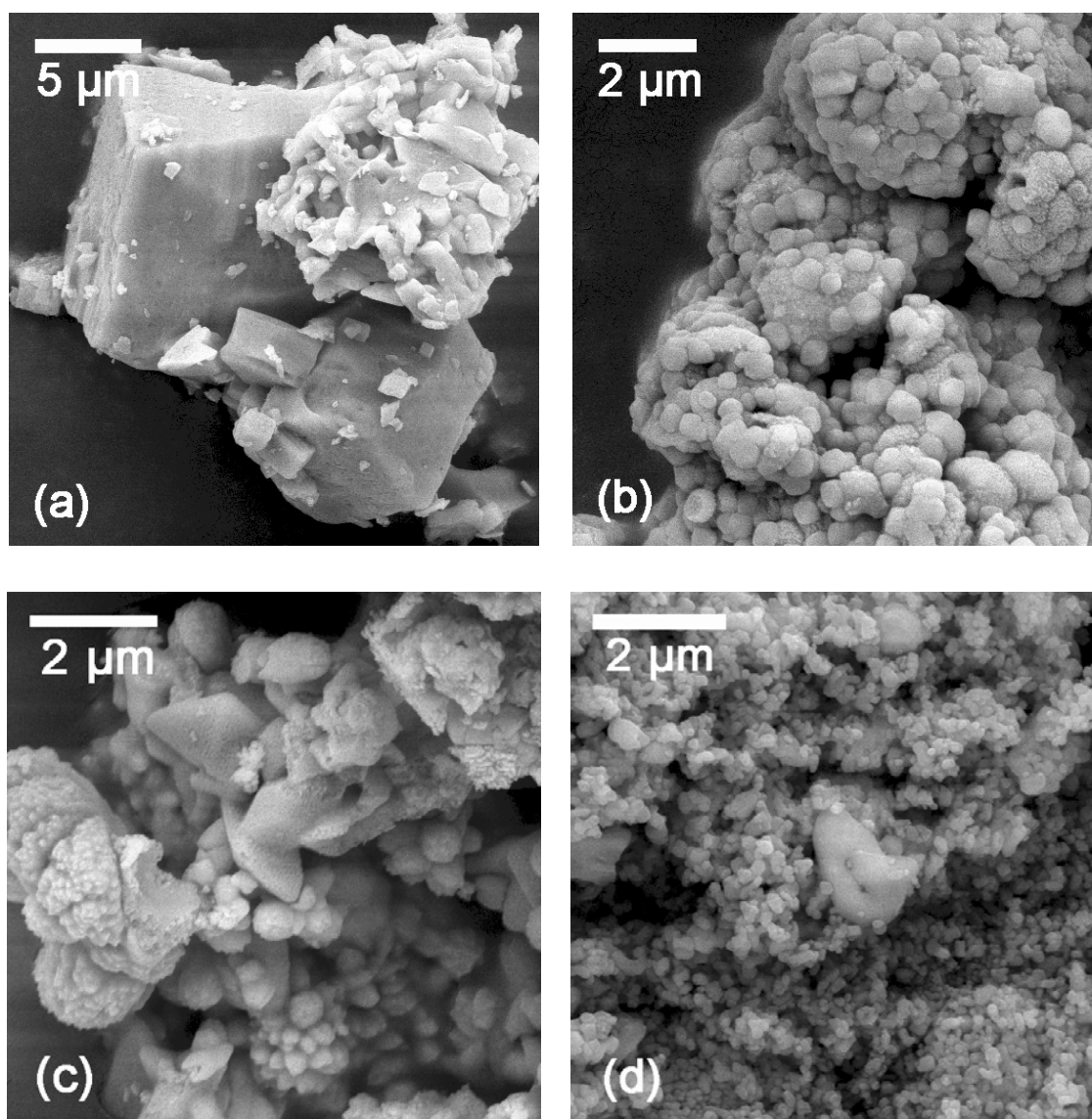

Fig. 4-9: SEM images of $Zn[Cu(CN)_3]$ from batch preparation (a) and its thermolysis products (CuO/ZnO) obtained under air for 3 h at 300 °C (b), 400 °C (c), 500 °C (d), respectively.

The structure of Cu/ZnO reduced from the corresponding thermolysis products under H_2/N_2 was studied by TEM (Fig. 4-10). The typical diameter of the particles is about 100–200 nm. As is discussed above, the morphology can be considerably influenced by the thermolysis temperature under oxidation conditions. However, the variation of the thermolysis temperature did not cause visible changes of the morphology under reduction atmosphere.
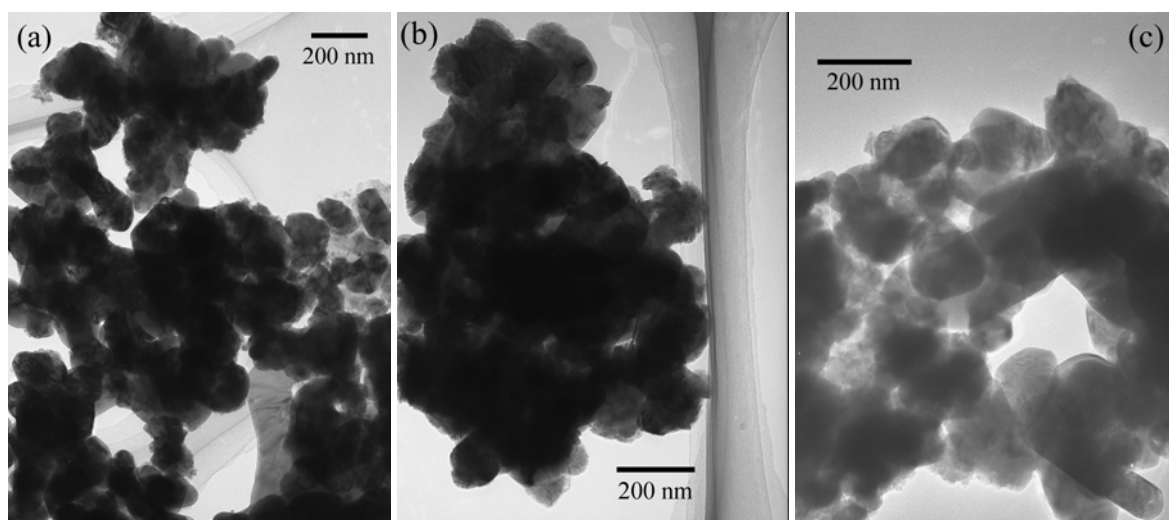
Fig. 4-10: TEM images of Cu/ZnO reduced under H_2/N_2 at 250 °C for 3 h from oxide products obtained at 300 °C (a), 400 °C (b) and 500 °C (c), respectively.

The BET surface area of the Cu/ZnO samples was determined by nitrogen physisorption. The catalytic activity of the products for methanol synthesis was carried out in a single-tube reactor with 72 vol% H_2, 10 vol% CO, 4 vol% CO_2 and 14 vol% He as feed gases. Table 4-4 shows the BET surface areas and the results of the catalytic tests. The sample Cu/ZnO 400 °C/250 °C had the highest BET surface area of 32.9 $m^2 \, g^{-1}$. Nevertheless, the catalytic activity for methanol synthesis turned out to be rather low, as indicated by the methanol concentration in the gas mixture. The low activity can be attributed to a small active copper surface area and a lack of metal-support interactions. In addition, the poisoning by adsorbed CN cannot be excluded.

Table 4-4: BET surface area and catalytic activity of the Cu/ZnO products.

Cu/ZnO	BET surface area / $m^2\,g^{-1}$	MeOH
300 °C/250 °C	10.5	15 ppm
400 °C/250 °C	32.9	15 ppm
500 °C/250 °C	6.3	15 ppm

4.3.2 Continuous overflow preparation and thermolysis

In the continuous overflow precipitation method, the properties of the product can be better controlled in comparison to simple batch-wise preparations. The main variation parameters are the residence time and the concentrations.

The morphology of the Cu–Zn cyanide complex was studied as a function of the solution concentration and the average residence time (related to the flow rate), respectively. First, the concentration was varied at a constant flow rate. It can be seen in Fig. 4-11 parts a–c that with increasing concentrations of Cu^{2+} and $[Zn(CN)_4]^{2-}$, the complex morphology changed from platelets to spherical particles and the size decreased. Second, the residence time was varied at a constant concentration. This effect is obvious (Fig. 4-11, parts d–f): A shorter residence time led to smaller particles. Hence, it can be concluded that both a higher concentration and a lower residence time (or high flow rate) lead to smaller (nano-) particles (spherical) instead of well-crystalline microcrystals (platelets).

Elemental analysis of the sample in Fig. 4-11 (part f) gave a Cu/Zn/CN ratio of 1:1:3.04 (16.8 wt% C, 19.6 wt% N, 29.0 wt% Cu, and 30.6 wt% Zn), which indicates that $Zn[Cu(CN)_3]$ was still the main component of the precipitates obtained by continuous overflow method, even at the highest concentration and the shortest residence time.
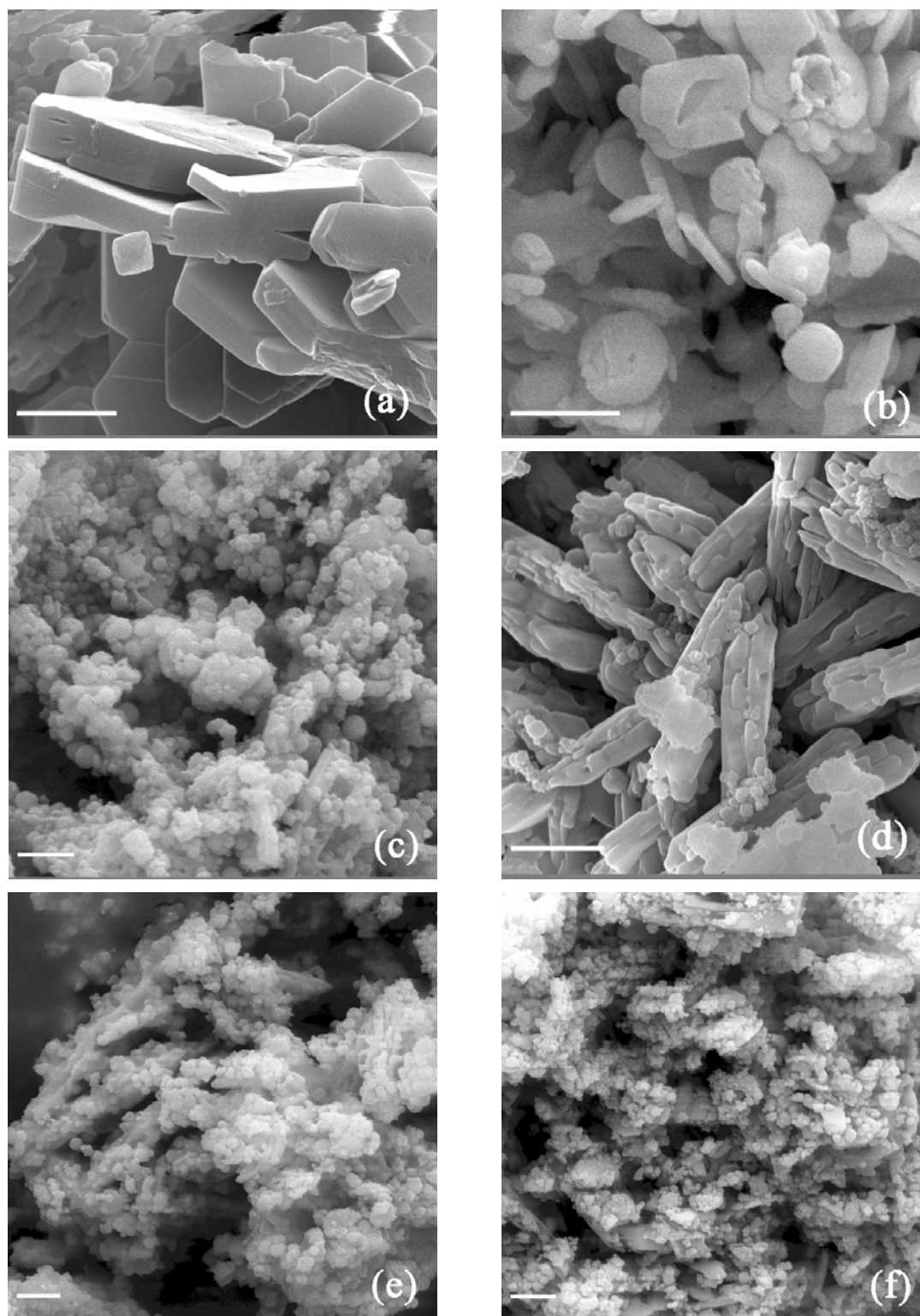
Fig. 4-11: SEM images of Zn[Cu(CN)$_3$] prepared by the continuous overflow method with different [Zn(CN)$_4$]$^{2-}$ concentrations (residence time of 30 s), i. e., 0.05 mol L^{-1} (a), 0.3 mol L^{-1} (b), 0.4 mol L^{-1} (c) and different residence time (constant concentration of 0.4 mol L^{-1}), i. e., 140 s (d), 30 s (e), 15 s (f). Cu^{2+} and [Zn(CN)$_4$]$^{2-}$ were always present in stoichiometric ratio (1:1). Scale bar: 1 μm.
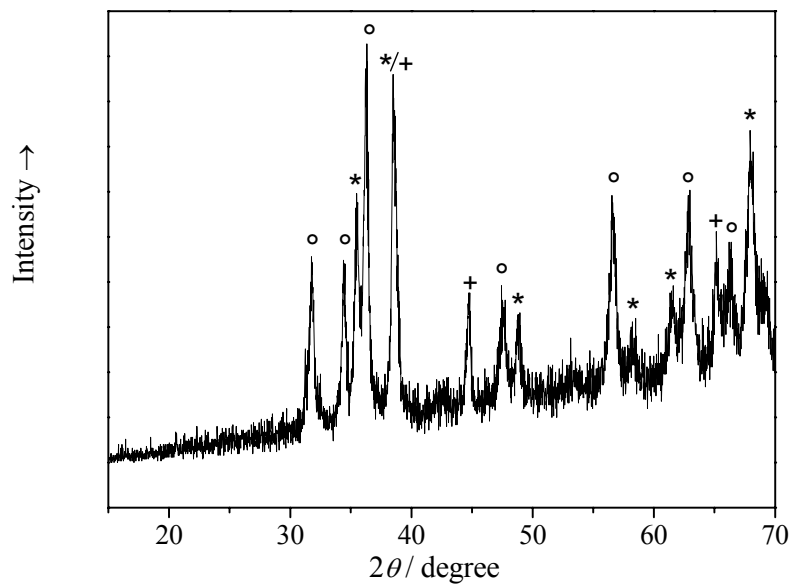
Fig. 4-12: XRD patterns of CuO/ZnO obtained by the oxidation of Zn[Cu(CN)$_3$] prepared by the continuous overflow method (with [Zn(CN)$_4$]$^{2-}$ and Cu^{2+} concentrations of 0.4 mol L^{-1} and residence time of 15 s) at 300 °C. The marked peaks correspond to ZnO (o), CuO (*) and the Al sample holder (+).
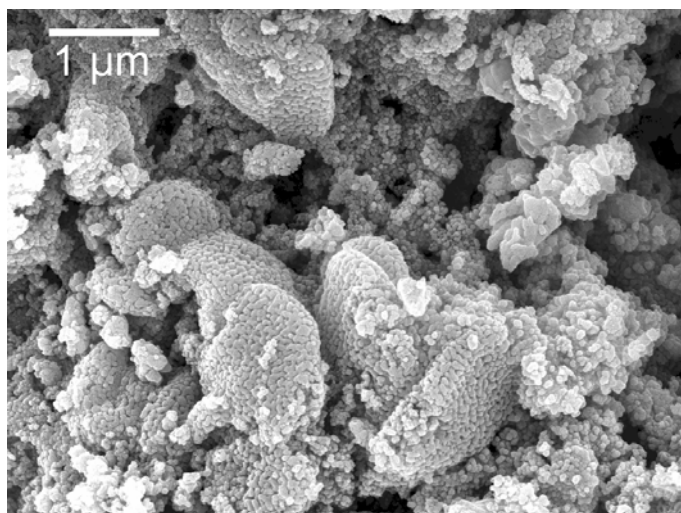
Fig. 4-13: SEM image of CuO/ZnO obtained by thermolysis of Zn[Cu(CN)$_3$] prepared by the continuous overflow method (with [Zn(CN)$_4$]$^{2-}$ and Cu^{2+} concentrations of 0.4 mol L^{-1} and residence time of 15 s) at 300 °C.
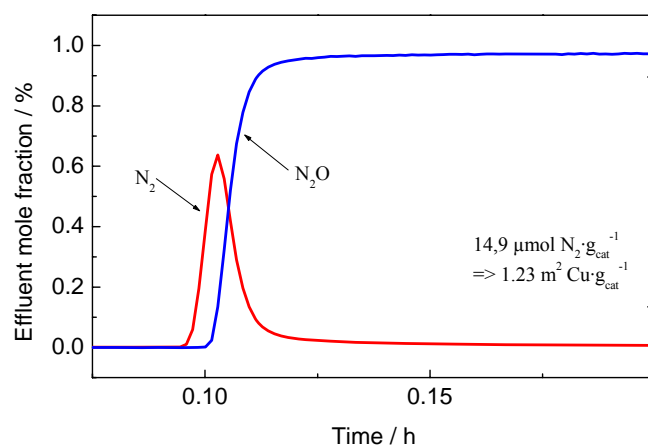
(a)
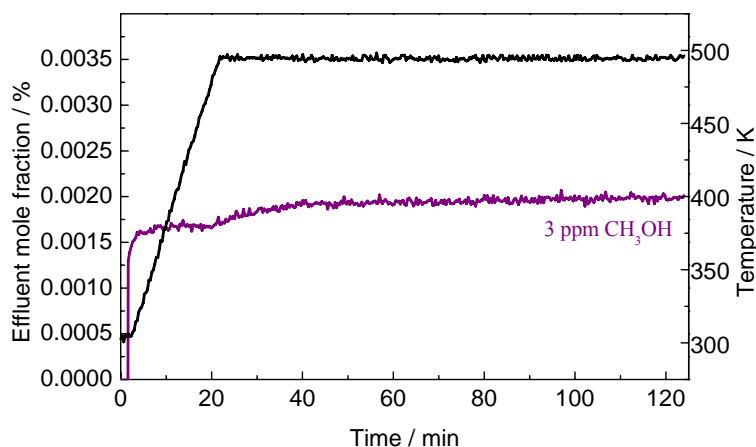
(b)

Fig. 4-14: Measurements of the specific copper surface area (a) and the catalytic activity of Cu/ZnO in the single-tube reactor (b). The Cu/ZnO was obtained from the reduction of the CuO/ZnO sample of Fig. 4-13.

The active Cu surface area and the catalytic activity for methanol synthesis of the sample shown in Fig. 4-13 were determined using the single-tube reactor. After reduction, the sample had a specific copper surface area of 1.23 m^2 g^{-1} (Fig. 4-14 a). The catalytic activity of the sample was rather low, corresponding to the low surface area of copper (Fig. 4-14 b).

Although the Cu-Zn cyanide precursor is formed in platelets or small particles, the active copper surface may be blocked by traces of carbon-containing species after thermolysis. The thermolysis process has to be improved to achieve a higher copper surface area and subsequently a higher conversion.

4.3.3 Pyrolytic decomposition of Zn[Cu(CN)$_3$]

In order to improve the specific surface area of CuO/ZnO and subsequently the catalytic activity, two alternative thermolysis methods were tested, i. e., the decomposition in a fluidized-bed reactor and the shock pyrolysis in a drop-tube reactor.
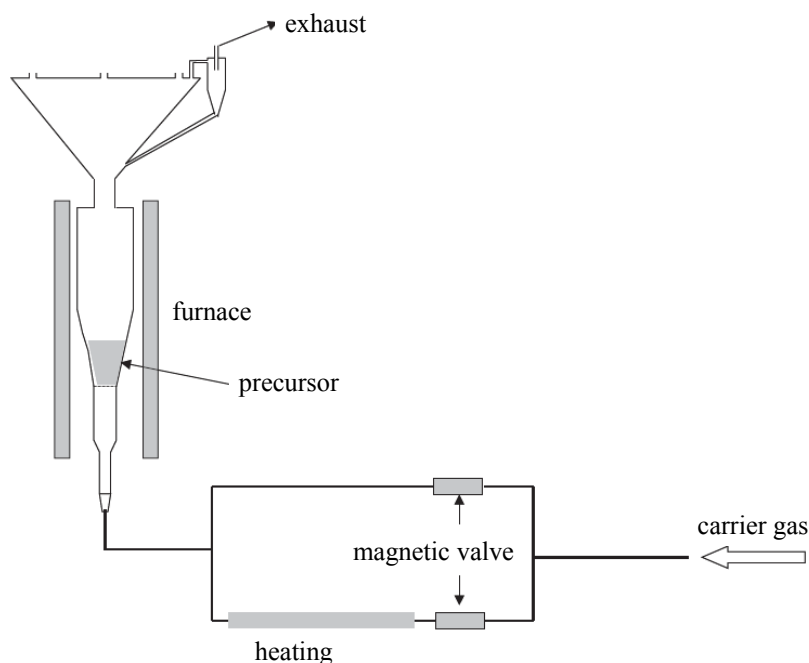
Fig. 4-15: Schematic illustration of the set-up of the fluidization reactor.

The fluidized-bed reactor is shown in Fig. 4-15. Two reaction routes are applied based on the fluidization technique.

(1) The precursor sample is first fluidized by passing synthetic air (20.5 vol% oxygen in nitrogen) through the reactor at room temperature. The furnace is then quickly heated to over 300 °C at a rate of ca. 30 K min^{-1}.

(2) Pre-heated hot air (400-500 °C) is introduced to the reactor and the particle precursor is fluidized and decomposed in a short period of time.

The fluidization can be realized in a conical reactor at a gas flow rate starting from 400 ml min^{-1}, whereas other reactor geometries require a higher gas flow. The fluidization is stable at 300 °C. However, further increase of the temperature, e. g., to 310 °C, will lead to sintering within less than half a minute. As a result, the fluidization cannot proceed. Thus-obtained solid product is not completely decomposed, even after pyrolysis at 400 °C for 2 h. Similar results were observed for the direct heating with a hot air. The variation of temperature and gas flow rate did not give a noticeable improvement of the decomposition, as shown by the XRD results (Fig. 4-16).
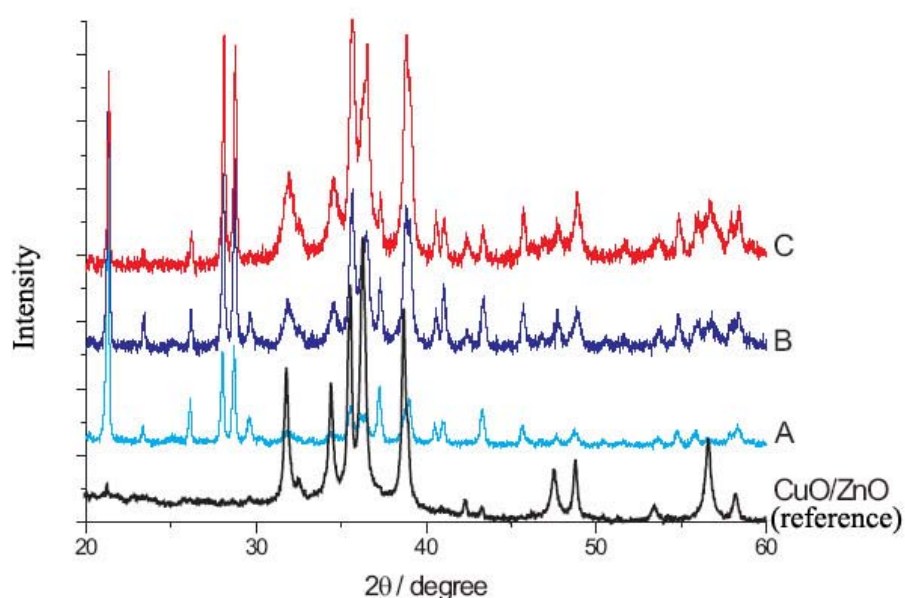
Fig. 4-16: XRD patterns of the reference CuO/ZnO and products thermolysed by the fluidization reactor, A: fluidized at 400 °C; B: fluidized at 300 °C; C: fluidized with hot air of 400 °C.

The drop-tube reactor is schematically illustrated in Fig 4-17. The powdered precursor is fed into the gas stream from a container with a rotating metal brush, by which a continuous and controlled feeding process with a low feeding rate is achieved. In order to avoid the adhesion of the precursor particles on the brush, a high gas flow rate of not less than 33.3 L min^{-1} is needed. Such a high flow rate leads to a residence time of as low as 0.5 s, which is too low for the pyrolysis. A T-fitting is thus introduced to by-pass part of the gas stream, through which a residence time of 10 s is achieved. The T-fitting directs approximately 5 % of the gas stream into the reactor, with the rest 95 % directly to the exhaust.
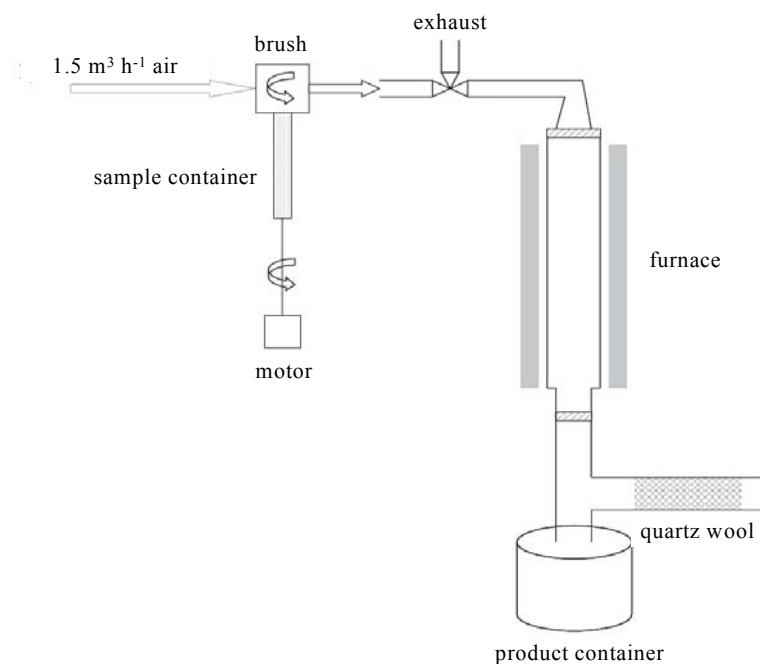
Fig. 4-17: Schematic illustration of the set-up of the drop-tube reactor.

The particle precursor in the gas stream is subsequently fed into a vertical quartz-tube reactor with an inner diameter of 30 mm and a length of 70 cm, at a temperature of 1100 °C. The feeding of the particles varied from 10 to 100 mg min^{-1}, and the carrier gas was set to 1500 ml min^{-1} constantly. However, it was found that the feeding of the precursor was difficult to maintain at a constant rate due to strong interactions between the precursor particles. The formed particles were collected and the exhaust gases were filtered by quartz wool. Table 4-5 showed the elemental analysis results of the products. The samples were not completely decomposed, despite the variation of process parameters. Nevertheless, it was found that a slower feeding of precursor could lead to a higher conversion. As a whole, the temperature of shock pyrolysis needs to be even higher to get a complete decomposition.

Table 4-5: Elemental analysis results of the products obtained by the drop-tube reactor.

Sample	C wt%	N wt%
Zn[Cu(CN)$_3$] precursor	17.4	20.3
900 °C, 10 mg min^{-1}	15.5	18.0
900 °C, 50 mg min^{-1}	16.7	19.3
1000 °C, 10 mg min^{-1}	10.9	12.7
1000 °C, 50 mg min^{-1}	13.0	15.0

4.3.4 CuO/ZnO/Al$_2$O$_3$

Al$_2$O$_3$ is known to be a promoter for Cu/ZnO catalysts inhibiting the thermal sintering of the Cu crystallites [108]. The Cu/ZnO/Al$_2$O$_3$ catalysts turned out to be far more active than the binary Cu/ZnO catalysts [57]. Kurtz et al. [57] found that the Cu/ZnO/Al$_2$O$_3$ catalyst exhibited a three to four times higher catalytic activity than the Cu/ZnO catalyst, although both catalysts had nearly the same specific Cu surface area. Al$_2$O$_3$ can also be regarded as a stabilizer for Cu crystallites, preventing them from sintering.

Using Al$_2$O$_3$ powder as Al$_2$O$_3$ source

With this synthesis method, Al$_2$O$_3$ powder was added to an aqueous solution of Cu^{2+}, [Zn(CN)$_4$]$^{2-}$ solution was added under stirring, the Cu-Zn cyanide complex Zn[Cu(CN)$_3$] was then formed on Al$_2$O$_3$. After thermolysis under air at 300 °C for 3 h, CuO/ZnO/Al$_2$O$_3$ samples with different Cu:Zn:Al ratios were obtained. Fig. 4-18 shows an SEM image of CuO/ZnO/Al$_2$O$_3$ (molar ratio Cu:Zn:Al=1:1:4). It can be seen that CuO/ZnO nanoparticles were formed on the surface of Al$_2$O$_3$.

An XRD pattern of the same sample is shown in Fig. 4-19. The presence of copper and zinc oxides is detected by the corresponding peaks in the spectra, whereas Al$_2$O$_3$ is X-ray amorphous.
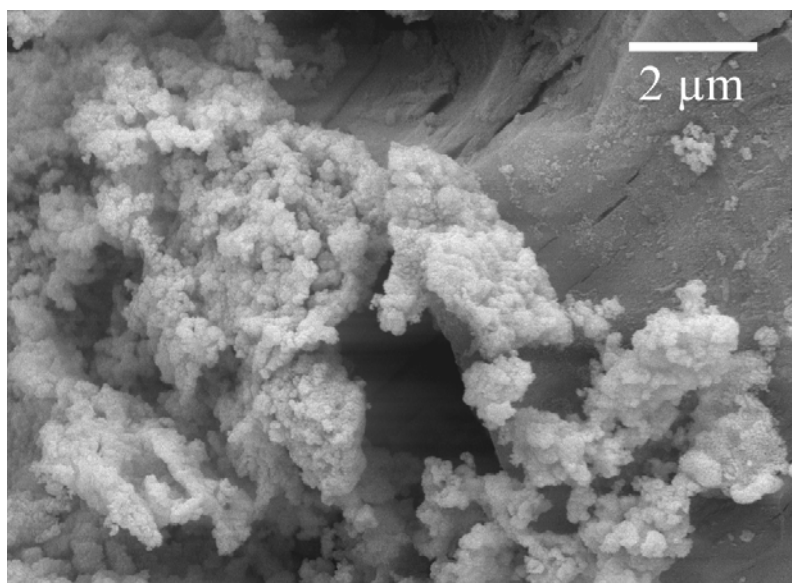
Fig. 4-18: SEM image of CuO/ZnO/Al$_2$O$_3$ (molar ratio Cu:Zn:Al=1:1:4) obtained from the thermolysis of Zn[Cu(CN)$_3$]/Al$_2$O$_3$ under air at 300 °C.
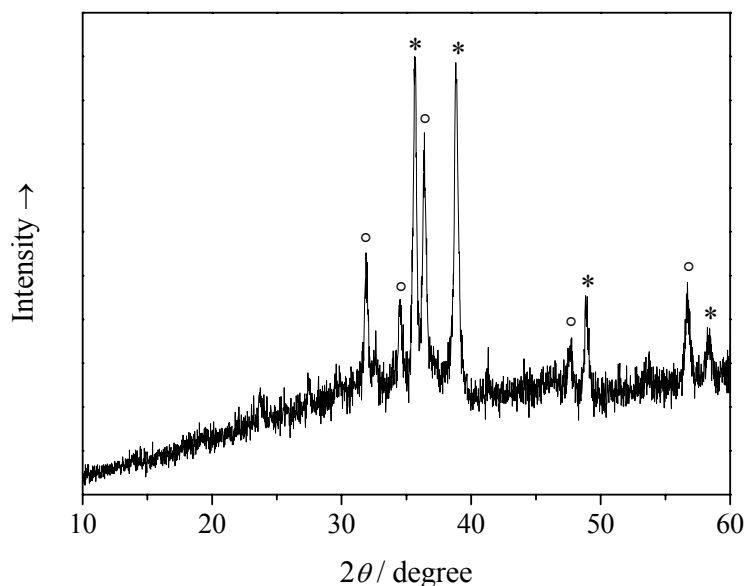
Fig. 4-19: XRD pattern of $CuO/ZnO/Al_2O_3$ (molar ratio Cu:Zn:Al=1:1:4) obtained from thermolysis of $Zn[Cu(CN)_3]/Al_2O_3$ under air at 300 °C. The marked peaks correspond to ZnO (o) and CuO (*).

The oxide samples were used as catalysts for the synthesis of methanol from $CO/CO_2/H_2$ in a 49-channel parallel flow multitubular reactor. Note that $CuO/ZnO/Al_2O_3$ was reduced prior to the catalytic test in order to obtain the active catalyst $Cu/ZnO/Al_2O_3$. This was done in-situ in the reactor. Because the absolute catalytic performance strongly depends on the specific conditions, all activities were related to an industrial benchmark catalyst (ICI Katalco 51-8), whose activity was set to 100 %. Table 4-6 showed the catalytic activity of the Cu-Zn-Al oxides with different amount of Al_2O_3. The presence of Al_2O_3 can enhance the catalytic activity for methanol synthesis. The $CuO/ZnO/Al_2O_3$ (molar ratio Cu:Zn:Al=1:1:4) sample has nearly 10 % of the activity of the ICI Katalco 51-8.

Table 4-6: Catalytic activity of $CuO/ZnO/Al_2O_3$.

Sample	MeOH	Catalytic activity
$CuO/ZnO/Al_2O_3$ (Cu:Zn:Al=1:1:2)	0.27 mol kg^{-1} h^{-1}	0.52 % ICI
$CuO/ZnO/Al_2O_3$ (Cu:Zn:Al=1:1:4)	4.95 mol kg^{-1} h^{-1}	9.6 % ICI

Using Al(OH)$_3$ as Al$_2$O$_3$ source

In order to improve the metal-support interaction of Cu-Zn-Al oxides, an Al(OH)$_3$ sol was used as Al$_2$O$_3$ source in stead of Al$_2$O$_3$ powder. In this method, the Al(OH)$_3$ sol was obtained at pH = 7. Cu^{2+} and [Zn(CN)$_4$]$^{2-}$ were then simultaneously added and a Zn[Cu(CN)$_3$] precipitate was formed on Al(OH)$_3$. After thermolysis under air at 300 °C for 3 h, CuO/ZnO/Al$_2$O$_3$ was obtained, which was shown in the SEM image in Fig. 4-20. The crystal structure of the oxides was studied by XRD (Fig. 4-21). CuO and ZnO are present as crystalline phases, whereas Al$_2$O$_3$ is X-ray amorphous and not present in the spectrum.

The oxide samples with different Cu:Zn:Al ratios were tested as catalysts for the synthesis of methanol from CO/CO$_2$/H$_2$ in a 49-channel parallel flow multi-tubular reactor. The results are shown in Table 4-7. The catalytic activities were about 7 % and 14 % when the Cu:Zn:Al ratio was 1:1:1 and 1:1:2, respectively. The Cu-Zn-Al catalysts prepared by thermolysis of the Zn[Cu(CN)$_3$]/Al(OH)$_3$ had a much higher catalytic activity than the binary Cu/ZnO catalysts and the thermolysis products of Zn[Cu(CN)$_3$]/Al$_2$O$_3$, indicating a better mixing of the oxides, an improved metal-substrate interaction and a higher dispersion of Cu, which is favourable in catalysis.
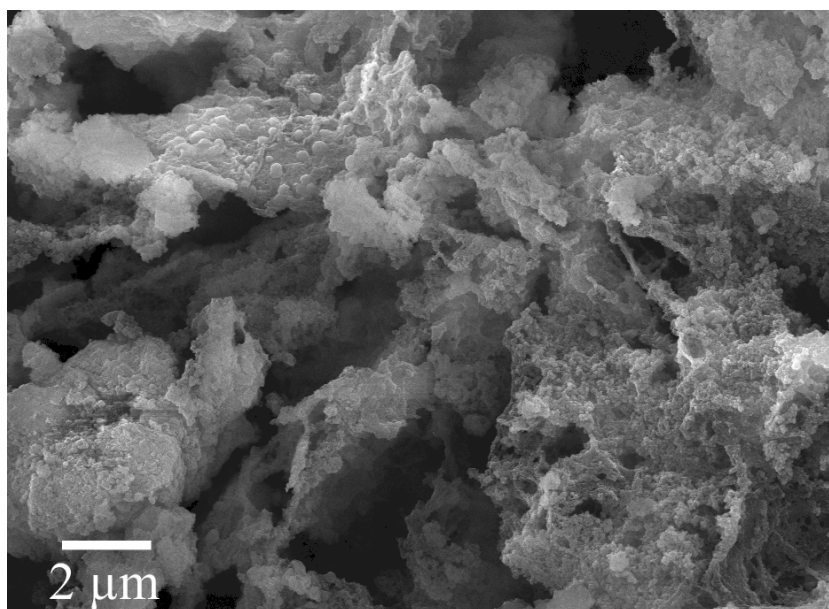
Fig. 4-20: SEM image of CuO/ZnO/Al$_2$O$_3$ obtained from thermolysis of Zn[Cu(CN)$_3$]/Al(OH)$_3$ under air at 300 °C.
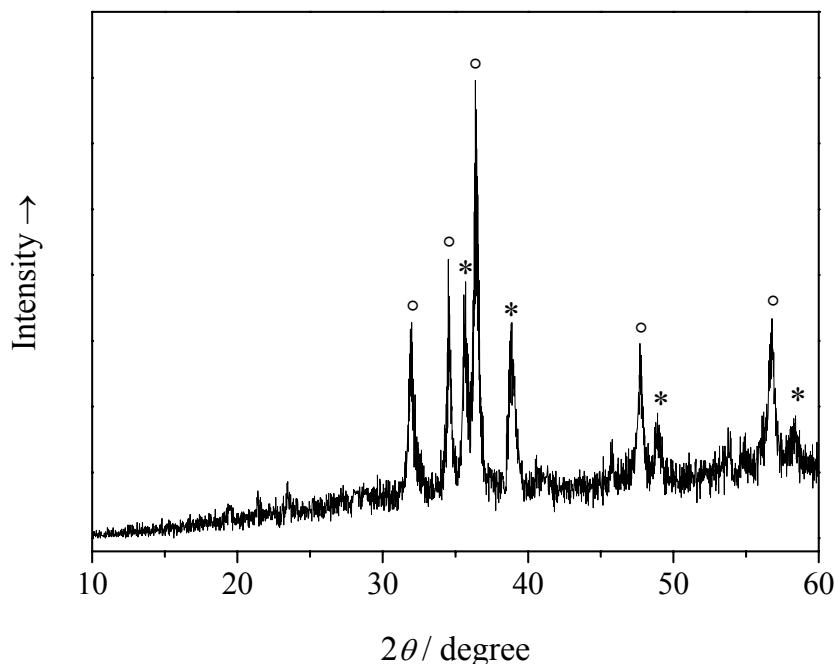
Fig. 4-21: XRD pattern of the CuO/ZnO/Al$_2$O$_3$ obtained from thermolysis of Zn[Cu(CN)$_3$]/Al(OH)$_3$. The marked peaks correspond to ZnO (o) and CuO (*).

Table 4-7: Catalytic activities of CuO/ZnO/Al$_2$O$_3$.

Sample	MeOH	Catalytic activity
CuO/ZnO/0.5Al$_2$O$_3$ (Cu:Zn:Al=1:1:1)	1.94 mol kg^{-1} h^{-1}	7.3 % ICI
CuO/ZnO/Al$_2$O$_3$ (Cu:Zn:Al=1:1:2)	3.69 mol kg^{-1} h^{-1}	13.9 % ICI

4.4 Conclusions

In summary, a batch-wise and a continuous synthesis method were applied to the precipitation of the copper–zinc coordination compound Zn[Cu(CN)$_3$]. Structurally, this compound consists of Cu–C–N–Zn units that bridge Cu and Zn centers. With the continuous overflow precipitation method, fine spherical particles were obtained at high solution concentration and short residence time (or a high flow rate). The thermolysis of the cyanides was studied in-situ

by TG-IR and TG-MS. Under oxidizing conditions, cyanogen was lost only at lower temperature whereas at higher temperature, thermal decomposition to carbon and nitrogen oxides occurred. The product of CuO and ZnO is an oxide mixture, which was reduced to Cu/ZnO and used as catalyst for methanol synthesis. The ternary oxide mixtures $CuO/ZnO/Al_2O_3$ were prepared by thermolysis of the precipitates of Cu-Zn-Al. A higher catalytic activity was observed in methanol synthesis for the precipitated samples on $Al(OH)_3$, which can be attributed to improved metal-substrate interaction and a higher dispersion of Cu.

5 [Zn(en)₃][Zn(CN)₄] and Zn(CN)₂: precursors for nanoscale ZnO

5.1 Introduction

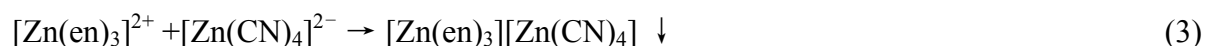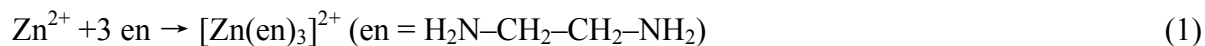Zinc oxide nanostructures have been the subject of intense interest due to their potential wide-range applications [124, 125]. Zinc oxide is a wide band gap semiconductor which is used, e.g., in electronics, photoelectrochemistry, and sensor technology [126-128]. In catalysis, a mixed catalyst containing copper and zinc oxide is used in methanol synthesis. Recent studies indicate that the Cu–ZnO interface plays an important role under reducing reaction conditions [129]. Nanostructured ZnO with various morphologies such as nanorods, nanowires, nanotubes, nanosheets and nanodiscs were prepared by different synthetic methods [130-135]. Vapour phase growth at high temperature is the major physical method to prepare ZnO nanostructures [136]. The wet-chemical synthesis is generally carried out with solutions of zinc salts in water or alcohols, to which hydroxide is added, which leads to the precipitation of ZnO [137]. The preparation of ZnO nanostructures by thermolysis of organometallic [138] or molecular precursors [139] was also reported.

Metal oxides can be obtained by thermolysis of metal cyanide coordination compounds under mild conditions [80, 81, 140-142]. In the work presented here, zinc oxide was prepared by thermolysis of [Zn(en)₃][Zn(CN)₄] and Zn(CN)₂. [Zn(en)₃][Zn(CN)₄] is a binuclear complex that decomposes to zinc oxide at moderate temperatures under oxidizing conditions. The thermolysis processes were followed by thermogravimetry and the product was characterized with respect to its crystallinity and morphology. It is of interest, e.g., for heterogeneous catalysis, whether the loss of the ligands would lead to a fine particulate ZnO phase. The neutral ligand ethylenediamine should be a good leaving group as well as the cyanide which may be released as cyanogen, (CN)₂ or undergo oxidative combustion [141].

5.2 Experimental

The binuclear coordination compound [Zn(en)₃][Zn(CN)₄] was prepared by coordinating Zn^{2+} (zinc nitrate) with ethylenediamine, giving a cationic complex, and by coordinating Zn^{2+} (zinc nitrate) with cyanide (KCN), giving an anionic complex, respectively. Mixing of both

solutions in equal amounts led to a white precipitate of the binuclear compound. The total concentration of zinc was 0.4 mol L^{-1}. All chemicals were used in stoichiometric amounts according to Eqs. (1)–(3). All reactions were carried out in water at room temperature.

$$Zn^{2+} + 3\ en \rightarrow [Zn(en)_3]^{2+}\ (en = H_2N–CH_2–CH_2–NH_2) \qquad (1)$$

$$Zn^{2+} + 4\ CN^- \rightarrow [Zn(CN)_4]^{2-} \qquad (2)$$

$$[Zn(en)_3]^{2+} + [Zn(CN)_4]^{2-} \rightarrow [Zn(en)_3][Zn(CN)_4] \downarrow \qquad (3)$$

Zinc cyanide Zn(CN)$_2$ was prepared by mixing aqueous solutions of Zn(NO$_3$)$_2$ and KCN in stoichiometric amounts as shown in Eq.(4). Zn(CN)$_2$ was formed as white precipitate.

$$Zn^{2+} + 2\ CN^- \rightarrow Zn(CN)_2 \downarrow \qquad (4)$$

The controlled thermolysis of the cyanides was carried out under air at 400 and 500 °C for 3 hours in a horizontal quartz tube reactor with an inner diameter of 30 mm.

Thermogravimetry was carried out with a Netzsch STA 409 TG-DTA apparatus. Samples were heated from room temperature to 1000 °C at a rate of 5 K min^{-1} under dynamic O$_2$ atmosphere at a flow rate of 50 mL min^{-1}. IR characterization of the products was performed with a Bruker Vertex 70 instrument in KBr pellets. High-resolution X-ray powder diffractometry was carried out in transmission geometry at beamline B2 at HASYLAB/DESY, Hamburg, Germany. Scanning electron microscopy was carried out with a Leo 420 instrument on gold-sputtered samples.

5.3 Results and discussion

5.3.1 Thermolysis of [Zn(en)$_3$][Zn(CN)$_4$]

Elemental analysis of [Zn(en)$_3$][Zn(CN)$_4$] gave 29.74 wt% Zn (calculated: 31.50 wt%), 28.14 wt% C (calculated: 28.93 wt%), 5.37 wt% H (calculated: 5.83 wt%), and 32.39 wt% N (calculated: 33.74 wt%). Zn was determined by atomic absorption spectroscopy, and carbon, hydrogen and nitrogen by combustion analysis.

The infrared spectrum of the zinc complex is shown in Fig. 5-1. All expected IR bands are visible: 3359 cm^{-1}/3365 cm^{-1}/3294 cm^{-1} (NH$_2$ valence), 2956 cm^{-1}/2893 cm^{-1} (CH$_2$ valence),

2144 cm^{-1} (C≡N valence), 1589 cm^{-1} (N−H deformation), 1467 cm^{-1} (C−H deformation), 1328 cm^{-1}/1278 cm^{-1} (C−H), and 1045 cm^{-1}/1001 cm^{-1}/ 959 cm^{-1} (C−C valence).
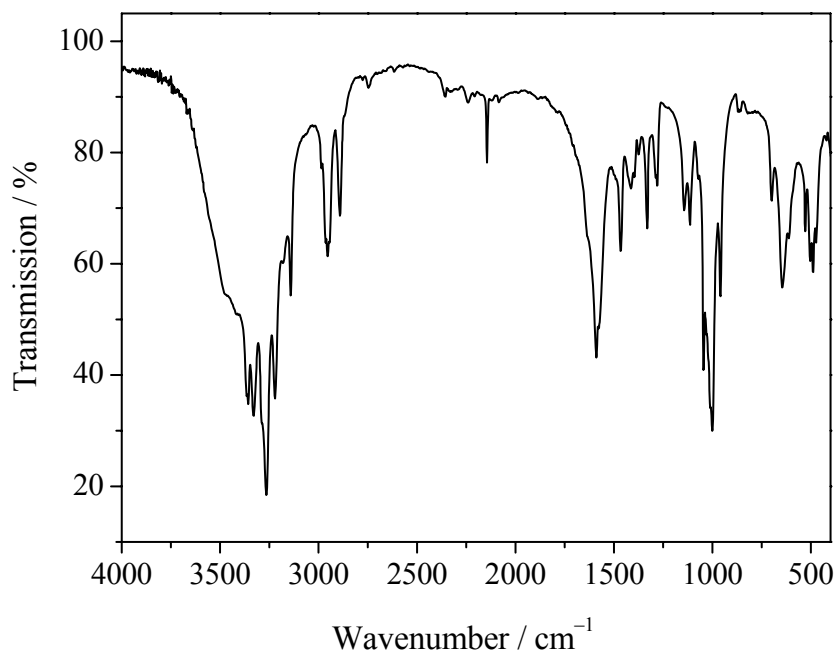
Fig. 5-1: Infrared spectrum of tris(ethylenediamine)zinc tetracyanozincate.

The thermolysis of [Zn(en)$_3$][Zn(CN)$_4$] under oxygen occurs in a multi-step process (Fig. 5-2). First, probably a part of the ethylenediamine is released without combustion in an endothermic process at around 150 ° C. Above about 200 ° C this is followed by the exothermic decomposition (combustion) of the remaining ethylenediamine and the cyanide which ceases close to 500 ° C. The observed total mass loss of 55.1 wt% (using the maximum weight as reference) was smaller than the expected value of 60.7 wt% for the reaction product ZnO. Because the residue after thermogravimetry was clearly identified as pure ZnO by X-ray diffraction (see also below) and crystalline side products can be ruled out, a possible explanation could be a deviation of the stoichiometry of the initial zinc complex from its ideal formula, e.g., it might have contained less than three ethylenediamine ligands (note that the thermobalance was evacuated before the experiment, i.e., before flooding it with oxygen).
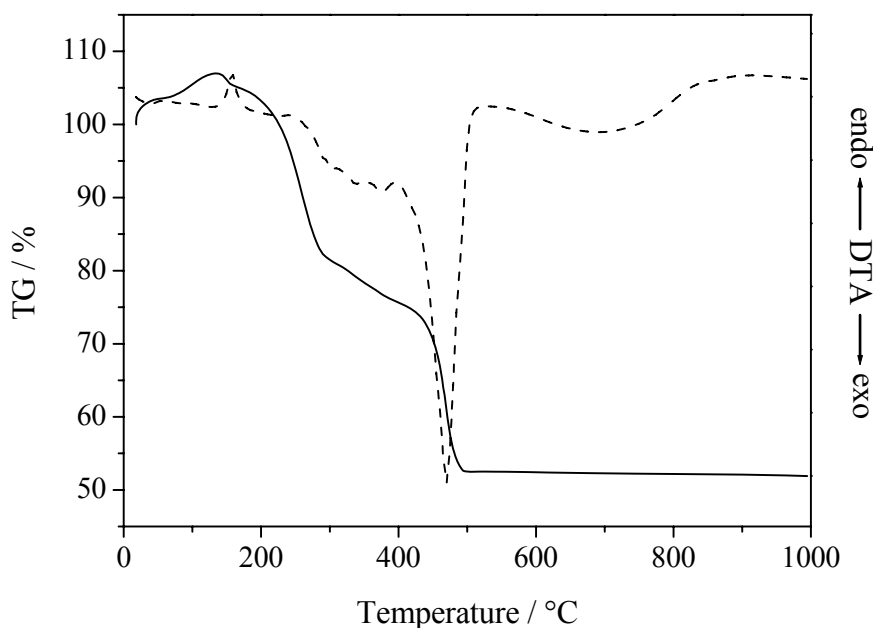
Fig. 5-2: Thermogravimetry of tris(ethylenediamine)zinc tetracyanozincate under dynamic oxygen atmosphere.

It was reported earlier that ethylenediamine was the first leaving group during the thermal decomposition of [Zn(en)$_3$][Ni(CN)$_4$] [143]. In our case, a weight loss of 37.6 wt% was observed up to the step in the TG curve at 430 °C, being close to an expected weight loss of 43.4 wt% from [Zn(en)$_3$][Zn(CN)$_4$] to Zn[Zn(CN)$_4$] = Zn(CN)$_2$. This suggests that the leaving of ethylenediamine dominates the first step of the decomposition, in agreement with the literature.

When heated in a furnace under air at 400 or 500 ° C for 3 h, the precursor fully decomposed to zinc oxide. Note that this temperature is the lowest which was possible for complete decomposition, and that it was chosen to avoid thermal sintering of the formed ZnO. This was shown by X-ray diffraction data (Fig. 5-3). No other crystalline phases were found.

Zinc oxide was obtained in the form of nanoparticles with a typical particle size of 200 nm, with no difference between a thermolysis at 400 or 500 °C (Fig. 5-4). The rhombohedral morphology of the precursor compound was fully destroyed during thermolysis, i.e., no topotactic or topochemical reaction [144] occurred.
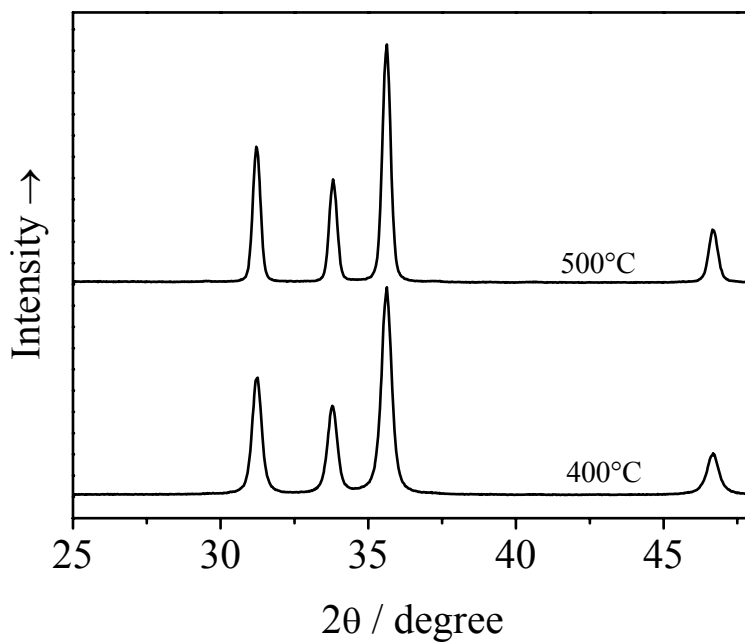
Fig. 5-3: XRD patterns of ZnO obtained from thermolysis of [Zn(en)$_3$][Zn(CN)$_4$] under air at 400 °C and 500 °C.
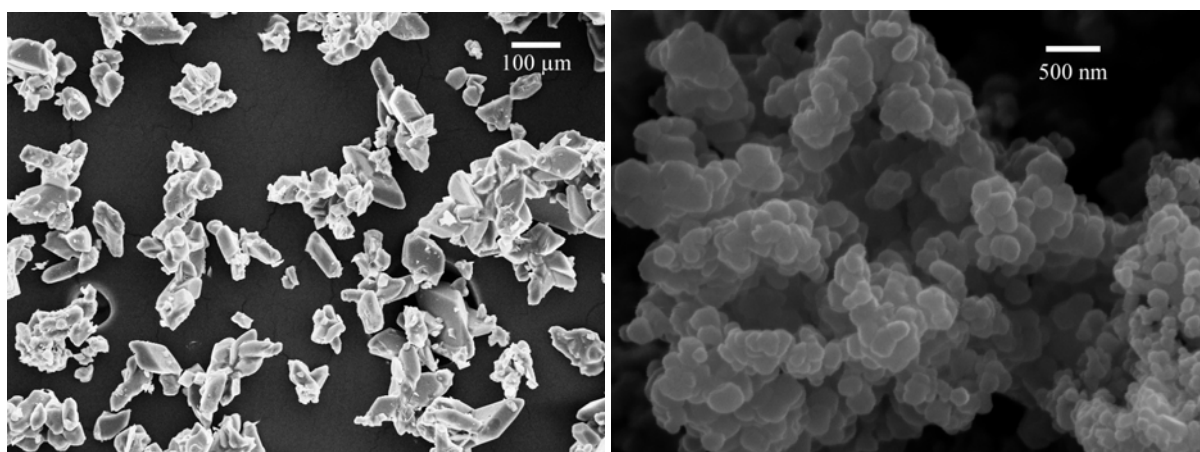
Fig. 5-4: Scanning electron micrographs of crystals of the precursor tris(ethylenediamine)zinc tetracyanozincate, and of the reaction product ZnO after thermolysis at 500 °C.

5.3.2 Thermolysis of Zn(CN)₂

Elemental analysis of $Zn(CN)_2$ gave 51.7 wt% Zn (calculated: 55.7 wt%), 17.7 wt% C (calculated: 20.4 wt%), 20.9 wt% N (calculated: 23.9 wt%) and 0.3 wt% H (calculated: 0 wt%). Zn was determined by atomic absorption spectroscopy, and carbon, hydrogen and nitrogen by combustion analysis. The presence of H indicates that crystal water may exist in the product.

The IR spectrum of zinc cyanide is shown in Fig. 5-5. The strong peak at 2216 cm^{-1} is the contribution of the CN bond (C≡N valence). Peaks at 3450 cm^{-1} and 1643 cm^{-1} can be attributed to water.
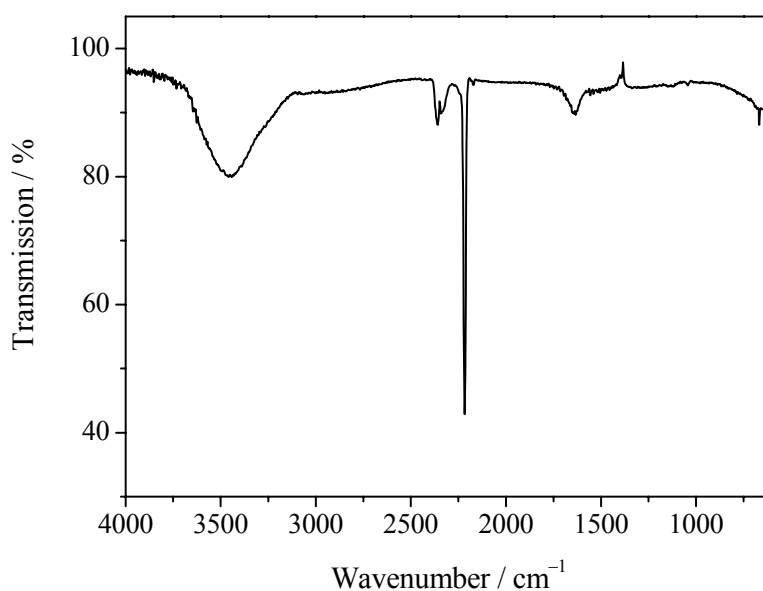
Fig. 5-5: Infrared spectrum of $Zn(CN)_2$.

The thermolysis of the $Zn(CN)_2$ was studied by thermogravimetric analysis coupled with infrared spectroscopy (TG-IR). The sample was heated under oxygen atmosphere. Fig. 5-6 (a) shows that there is a slight weight loss below 110°C, which is apparently due to the loss of water. After that, the decomposition of the $Zn(CN)_2$ occurs in one step from 530 °C to 610 °C. The observed total mass loss was 33.2 wt%, indicating the loss of CN and the formation of oxide.
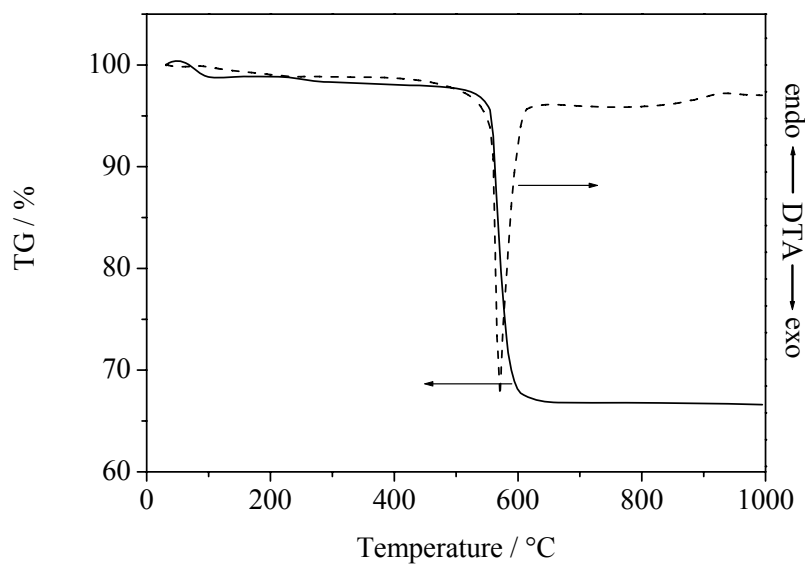
(a)
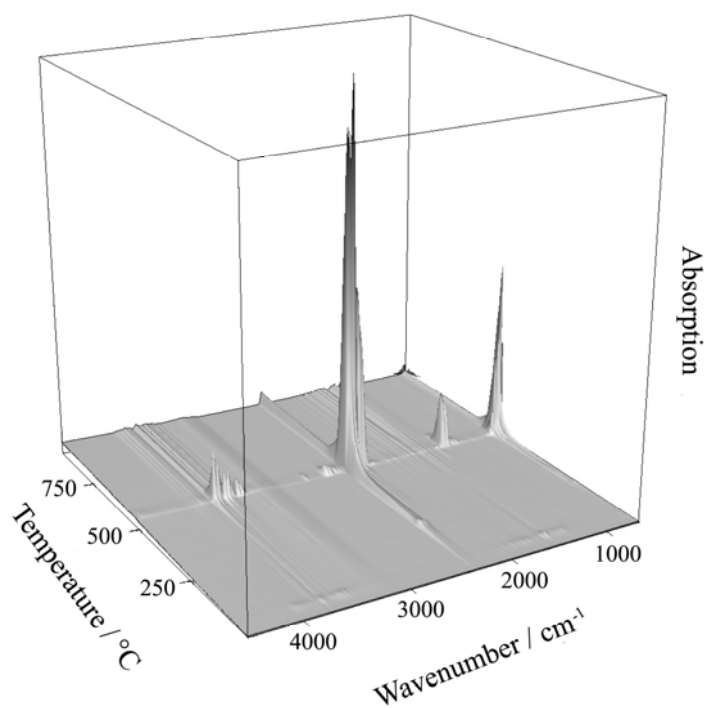
(b)

Fig. 5-6: Thermogravimetry of Zn(CN)$_2$ under dynamic oxygen atmosphere (a), and the corresponding time-resolved infrared spectra of the released gases during heating (b) (heating rate 5 K min^{-1}).

The infrared spectra in Fig. 5-6 (b) correspond to the evolved gas phase during heating. The release of a small amount of cyanogen $(CN)_2$ is reflected by the weak peak at 2343 cm^{-1}, which appeared first. Carbon dioxide (four bands from 3740 cm^{-1} to 3590 cm^{-1}, and bands at 2360 cm^{-1}, 2312 cm^{-1} and 671 cm^{-1}) and nitrogen monoxide (at about 1600 cm^{-1}) were subsequently released at elevated temperature.

X-ray diffraction shows that the cyanide precursor fully decomposed to zinc oxide when thermolyzed under air at 400 or 500 ° C for 3 h (Fig. 5-7). No other crystalline phases were detected.
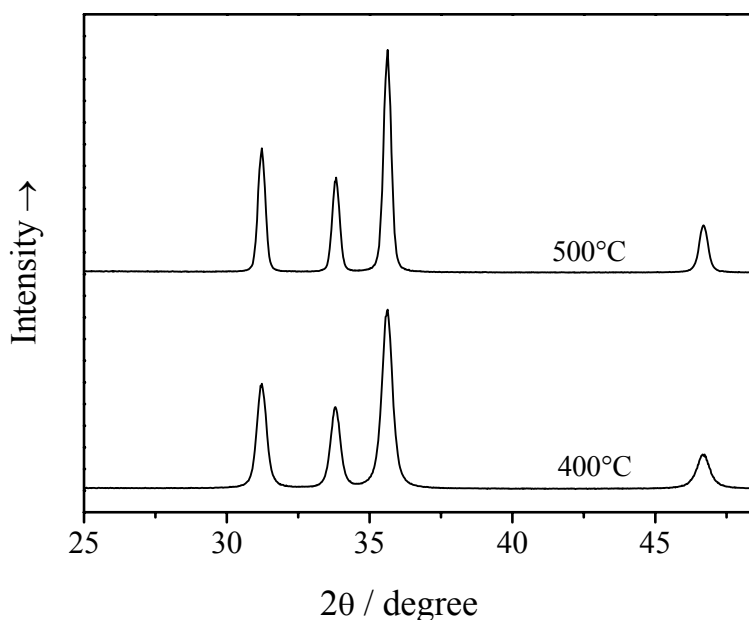
Fig. 5-7: XRD patterns of ZnO obtained from thermolysis of Zn(CN)₂ under air at 400 °C and 500 °C.

The SEM images of zinc cyanide and its oxidation product ZnO (thermolyzed at 500 °C) are shown in Fig. 5-8. The initial zinc cyanide crystallized as sub-micron octahedra. Zinc oxide was obtained in the form of nanoparticles with a typical particle size of 100-200 nm. The structure of the precursor compound was fully destroyed during thermolysis.

(a)   (b)
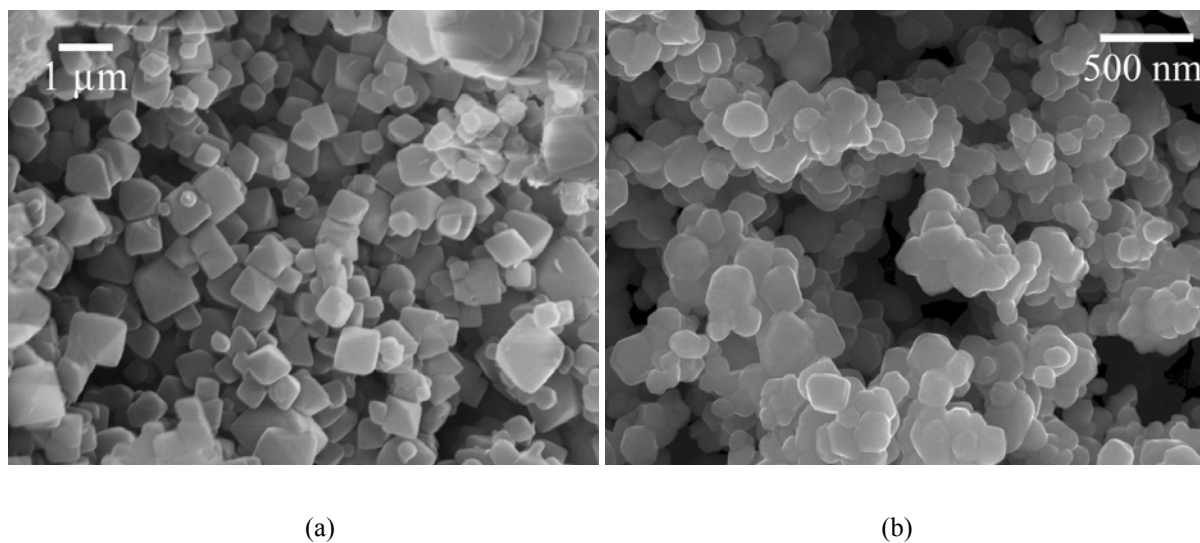
Fig. 5-8: Scanning electron micrographs of crystals of the precursor $Zn(CN)_2$ (a), and of the reaction product ZnO after thermolysis at 500 °C (b).

5.4 Conclusions

The binuclear complex of $[Zn(en)_3][Zn(CN)_4]$ and the uninuclear compound of $Zn(CN)_2$ were prepared. Under oxygen, the thermolysis of both complexes leads to ZnO nanoparticles with a size of 100–200 nm. There is no apparent correlation between the morphology of the crystals of the parent compound and the ZnO particles, i.e., the structure completely breaks down during thermolysis. It was found that under oxygen the decomposition of the $[Zn(en)_3][Zn(CN)_4]$ occurs in multi-steps in the range of 150–500 °C, whereas that of the $Zn(CN)_2$ occurs in one-step between 530 and 610 °C. The thermolysis of these Zn-based compounds is a useful route to synthesize nano-scale ZnO.

6 Sol-gel synthesis of porous ZnO/Al$_2$O$_3$

6.1 Introduction

Cu/ZnO/Al$_2$O$_3$ catalysts are widely used for industrial methanol synthesis and for the water-gas shift reaction, and therefore have been intensively investigated in the last decades [40, 145]. ZnO/Al$_2$O$_3$ is an active component of this catalyst, and it also acts as a convenient support for other metals or metal oxides [146]. Jensen et al. [147] synthesized ZnO/Al$_2$O$_3$ mixture with high surface area by composite combustion of their volatilized acetylacetonate precursors in a premixed air-methane flame. Otero Areán and coworkers [148] prepared spinel-type Al$_2$O$_3$-ZnAl$_2$O$_4$ mixed metal oxides by controlled hydrolysis of mixed metal alkoxides, followed by calcination of the resulting gels.

The sol-gel method is widely used to synthesize high-surface-area Al$_2$O$_3$. Sol-gel derived aluminas are typically prepared by catalysed hydrolysis and condensation of aluminum alkoxide precursors, such as aluminum isopropoxide or aluminum butoxide [149-152]. Baumann et al.[153] reported a new sol-gel technique for the preparation of alumina. In this method, alumina aerogels were prepared by the addition of propylene oxide to aqueous or ethanolic solutions of hydrated aluminum salts, followed by drying with supercritical CO$_2$. This technique gave low density, high-surface-area alumina aerogels without the use of alkoxide precursors. This alkoxide-free sol-gel synthesis technique was also used to prepare various metal oxides, such as Fe$_2$O$_3$, Cr$_2$O$_3$, Ga$_2$O$_3$ and ZrO$_2$ [60, 154, 155], as well as a variety of binary metal oxide systems [61, 156, 157]. Through the use of an organic epoxide that acts as a proton scavenger, solutions of common hydrated metal salts undergo hydrolysis and condensation reactions to form metal oxide sol-gel materials, as shown in Scheme 6-1.

In this chapter, the synthesis of bimetallic porous ZnO/Al$_2$O$_3$ xerogels using propylene oxide is discussed. Nanostructured ZnO/Al$_2$O$_3$ was obtained with a high specific surface area and a narrow pore size distribution, where ZnO was highly dispersed in Al$_2$O$_3$ in an atomic scale. The nanocomposite is expected to be an active support for transition metal catalysts such as copper in methanol synthesis.
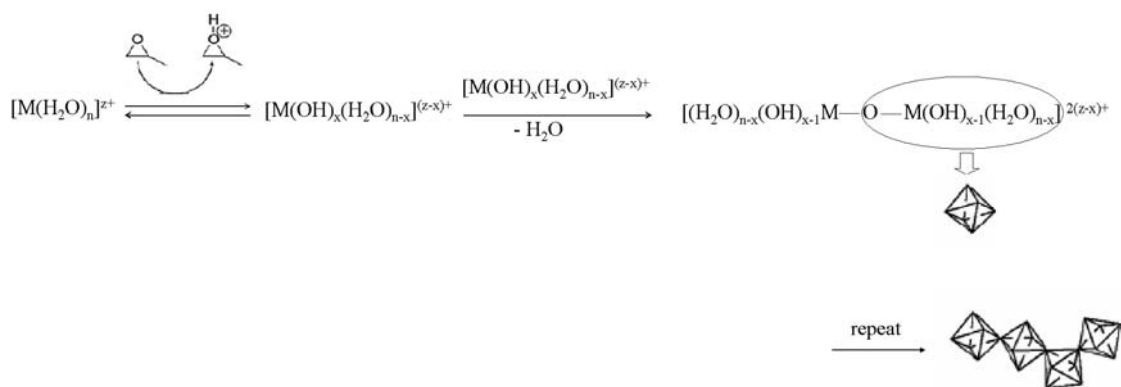
Scheme 6-1: General reaction scheme for the epoxide-addition sol-gel process [61].

6.2 Experimental

In a typical reaction for the synthesis, Al(NO$_3$)$_3$·9 H$_2$O and Zn(NO$_3$)$_2$·6 H$_2$O in different molar ratios were dissolved in ethanol to give a clear solution ([Zn^{2+}]+[Al^{3+}]=1 mol L^{-1}). Propylene oxide was then added to the solution. The molar ratio of propylene oxide to the sum of the two metals was 10:1. After stirring for 10 min at room temperature, the reaction mixture was transferred into a closed vessel. A white gel formed within 30 min. This wet gel was allowed to age at room temperature for 24 h in a closed vessel and then soaked in a bath of absolute ethanol for 24 h to exchange the water (originating from the crystal water of the starting salts) from the pores of the gel. The xerogel was obtained after drying under air for 3-4 days. For calcination the xerogel was heated up to 400 °C at a rate of 5 K min^{-1} under dynamic air in a tube furnace. The reactor was held at that temperature for 3 h before cooling.

Thermogravimetry (TG) was carried out with a Netzsch STA 409 TG-DTA apparatus in the temperature range of 25-1000 °C under flowing oxygen using a heating rate of 5 K min^{-1}. The evolved gases were monitored in-situ by infrared spectroscopy (IR) with a Bruker Vertex system. The structure of the resulting ZnO/Al$_2$O$_3$ was studied by transmission electron microscopy (TEM) with a Philips CM 200 FEG instrument. X-ray powder diffraction (XRD) was carried out at room temperature in transmission mode at beamline B2 at HASYLAB with monochromatic radiation. Extended X-ray absorption fine structure (EXAFS) spectroscopy was performed at beamline E4 at HASYLAB in transmission mode at 77 K. The specific surface area was determined by nitrogen physisorption at 77 K (BET method). The pore size distribution was obtained using the BJH method from the desorption branch of the isotherms.

6.3 Results and discussion
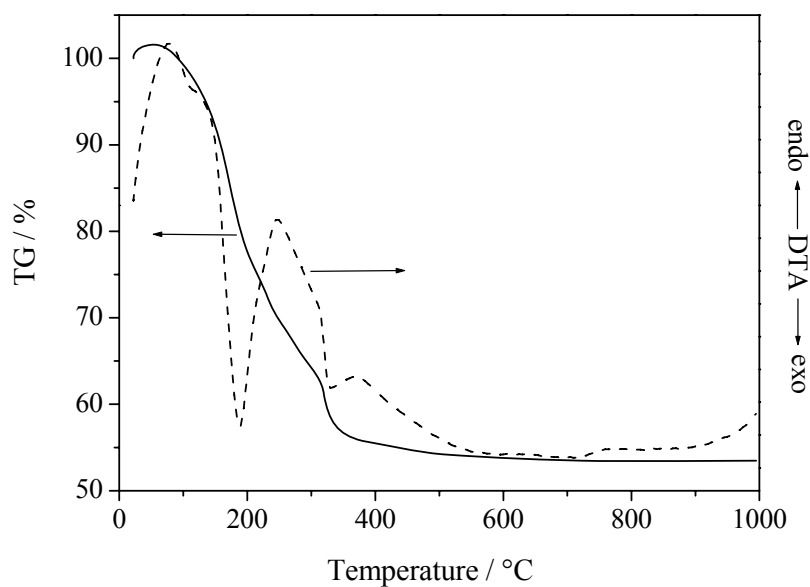
(a)
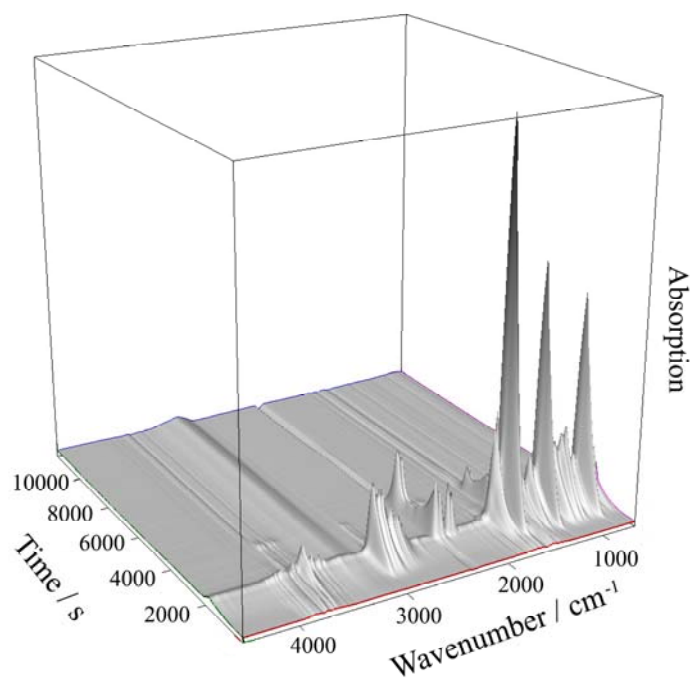
(b)

Fig. 6-1: Thermogravimetry of air-dried Zn-Al xerogel under oxygen atmosphere (a), and the corresponding time-resolved infrared spectra of the released gases during heating (b) (heating rate 5 K min^{-1}).

The thermolysis of the air-dried Zn-Al xerogel was studied by thermogravimetric analysis coupled with infrared spectroscopy (TG-IR). When heated up under oxygen, the decomposition of the xerogel occurred in a multi-step process (Fig. 6-1 a). The weight loss started at about 70 °C and ceased at about 500 °C. The first exothermic peak appeared at about 190 °C, which can be attributed to the release of water and residual organics from the gel preparation. The second peak at about 330 °C is due to the oxidation of residual organic compounds. Carbon dioxide (at 2360, 2312, and 671 cm^{-1}) and nitrogen oxide (at 1618 cm^{-1}) were detected from the evolved gas phase during heating (Fig. 6-1 b). The total weight loss was about 48 %.

TEM images of the porous calcined ZnO/Al$_2$O$_3$ xerogel with different Zn to Al ratios are shown in Fig. 6-2. The particles in Fig. 6-2 a&b had a typical particle diameter of up to 10 nm. When the Zn to Al ratio was increased to 2:1, the homogeneity decreased with particles as big as 30 nm (Fig. 6-2 c).
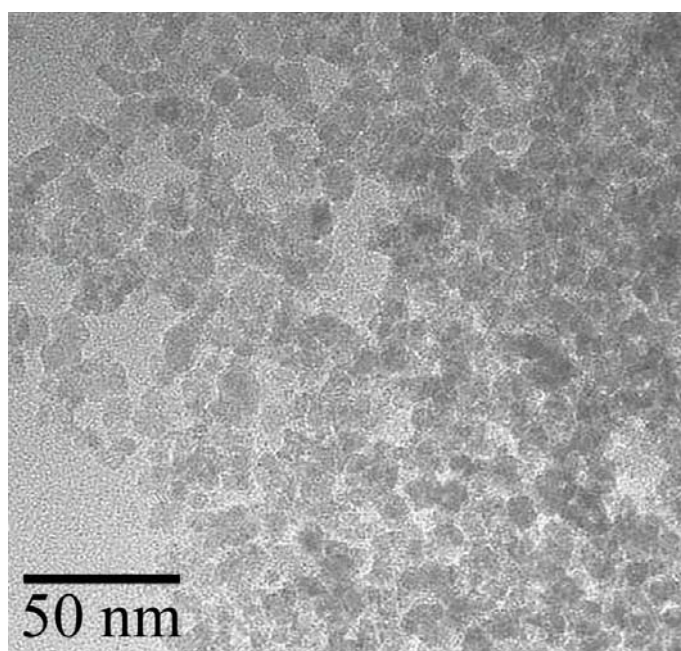
(a)
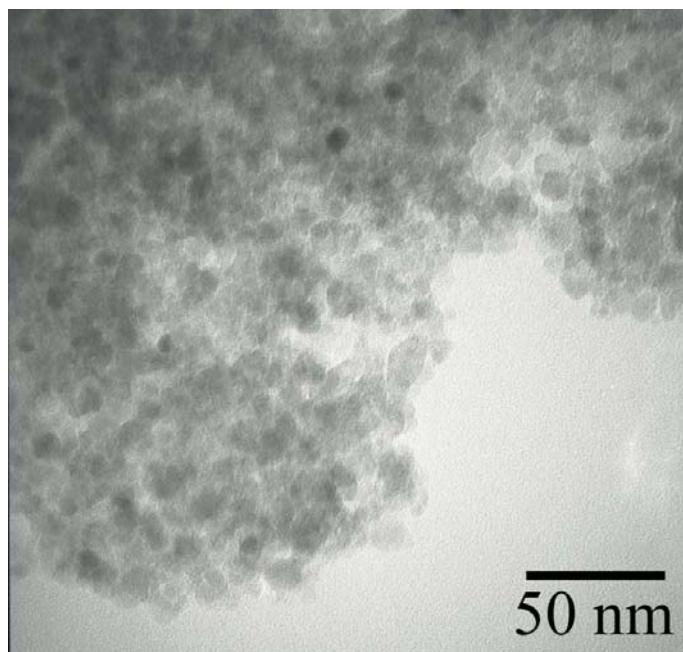
(b)
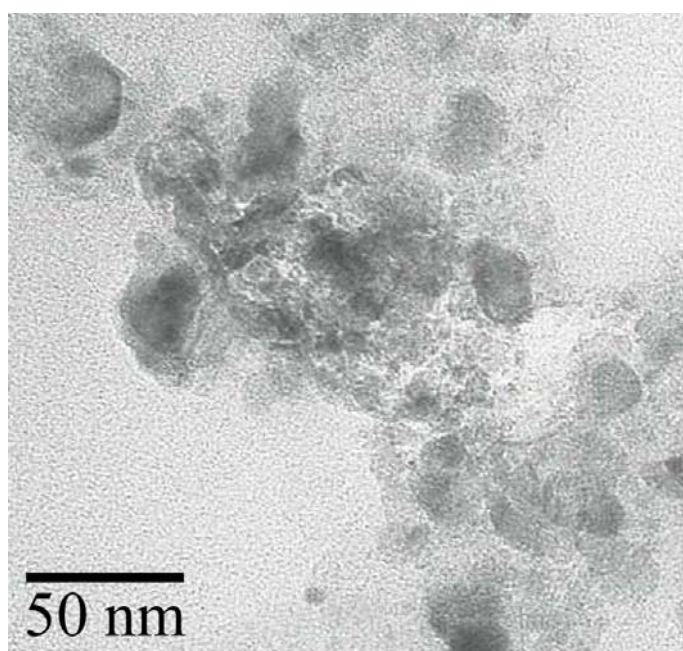
(c)

Fig. 6-2: TEM images of ZnO/Al$_2$O$_3$ calcined xerogel with different Zn:Al molar ratios. (a) Zn:Al = 1:2, (b) Zn:Al = 1:1, (c) Zn:Al = 2:1.

The crystal structure of the Zn-Al oxides as determined by XRD was also strongly affected by the Zn:Al ratio. ZnO/Al$_2$O$_3$ was X-ray amorphous for Zn:Al ratios of 1:2 and 1:1, indicating

the absence of long range order. However, for the ratio of 2:1, the ZnO crystallinity was significantly increased as indicated by peaks originating from ZnO nanocrystals (Fig. 6-3), corresponding to the presence of large particles in the TEM image. The Al$_2$O$_3$ phase was always X-ray amorphous.
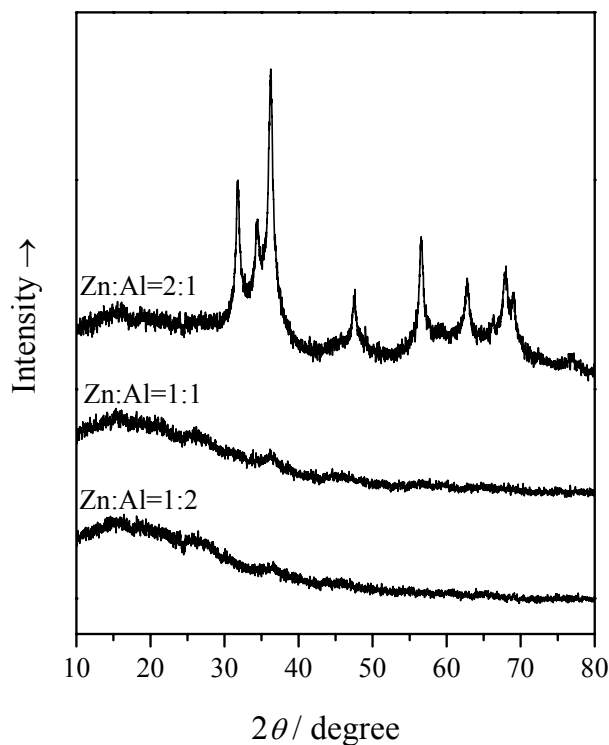
Fig. 6-3: XRD patterns of ZnO/Al$_2$O$_3$ calcined xerogel with different Zn:Al molar ratios.

A closer look to the structure of the ZnO/Al$_2$O$_3$ was obtained by X-ray absorption spectroscopy (EXAFS; Fig. 6-4 and Table 6-1). In the Zn K-edge Fourier transform magnitudes, the first shell of Zn−O in ZnO is clearly present in all three samples. The Zn−Zn shells at about 3 Å were different for different Zn:Al ratios. For the sample of Zn:Al=1:2, the Zn-Zn peak is invisible. A weak Zn-Zn peak is observed for Zn:Al=1:1. The absence of Zn neighbors around Zn suggests a dispersion of ZnO in Al$_2$O$_3$ on the atomic length scale, which can be beneficial when the bimetallic oxides are used as support for Cu catalysts in methanol synthesis. The Zn−Zn peak was much stronger for the 2:1 sample, indicating the presence of ZnO nanocrystals, in good agreement with the XRD results. It can be seen that an appropriate

concentration of Al$_2$O$_3$ can effectively disperse ZnO and inhibit the formation of crystalline ZnO.

(a)   (b)
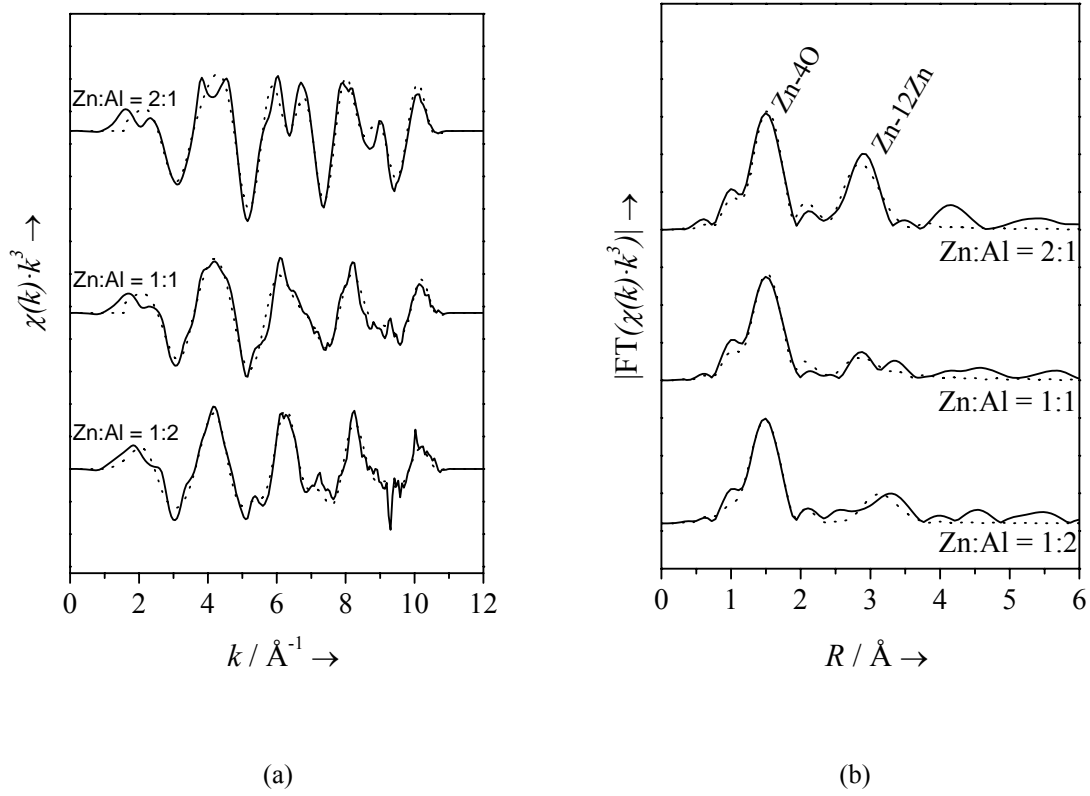
Fig. 6-4: Zn K-edge EXAFS raw data (a) and Fourier transform magnitudes (b) of ZnO/Al$_2$O$_3$ calcined xerogel with different Zn:Al molar ratios. Solid line: experimental data, dotted line: fit data.

Table 6-1: Fit parameters for the Zn K-edge EXAFS spectra of ZnO/Al$_2$O$_3$ with different Zn:Al molar ratios.

ZnO/Al$_2$O$_3$ Zn:Al	R(Zn-O) /Å	N(Zn-O)	σ^2(Zn-O) /Å$^2 \cdot 10^3$	R(Zn-Zn) /Å	N(Zn-Zn)	σ^2(Zn-Zn) /Å$^2 \cdot 10^3$
1:2	1.95	3.5	7.7	3.52	0.6	1.97
1:1	1.95	3.0	6.1	3.49	5.6	17.3
2:1	1.96	3.7	6.1	3.21	7.3	13.2
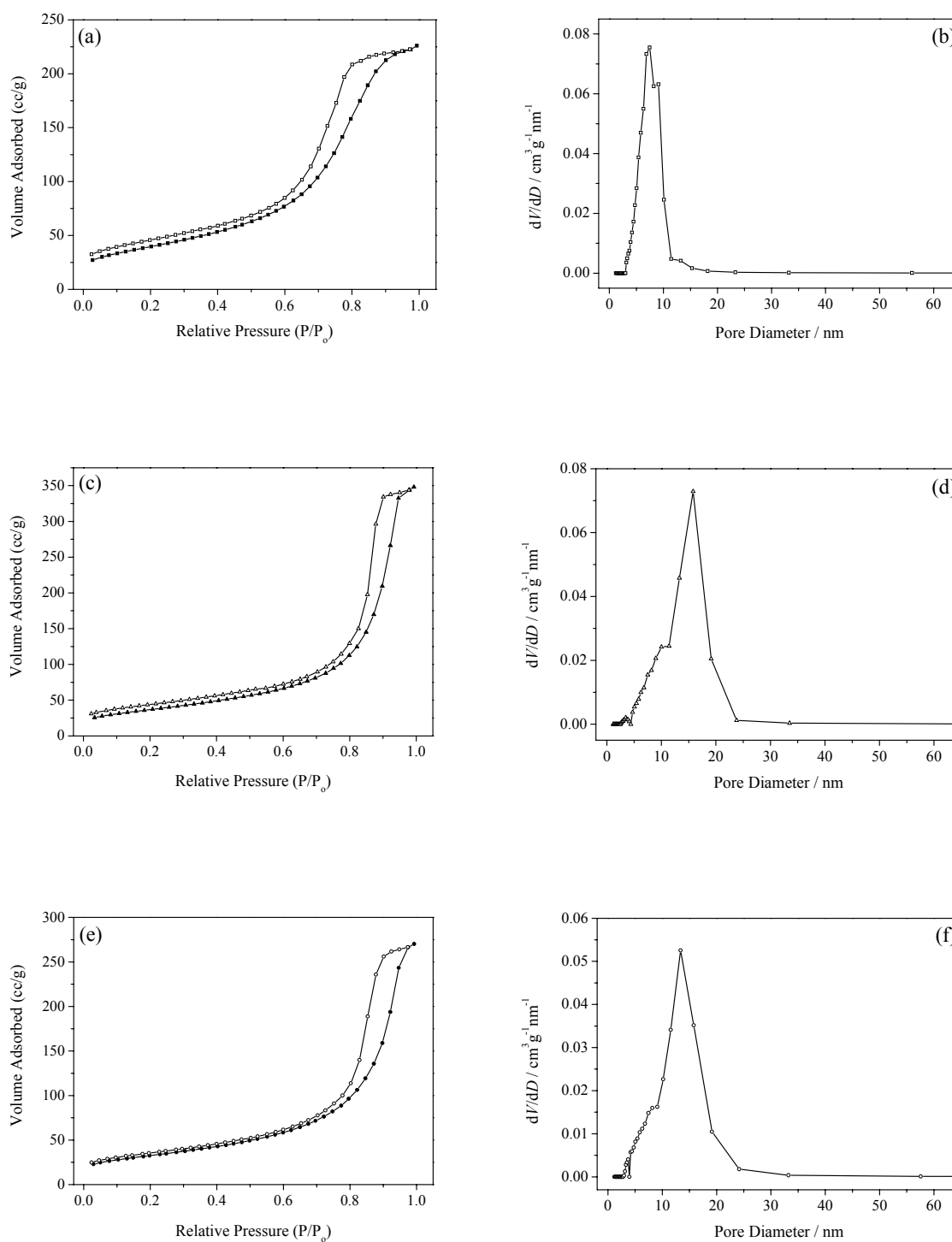
Fig. 6-5: Nitrogen physisorption isotherms and the corresponding pore size distribution of porous ZnO/Al$_2$O$_3$ calcined xerogels with different Zn to Al ratios. (a)&(b), Zn:Al = 1:2; (c)&(d), Zn:Al = 1:1; (e)&(f), Zn:Al = 2:1.

Nitrogen physisorption isotherms and the corresponding pore size distribution of porous ZnO/Al$_2$O$_3$ samples are shown in Fig. 6-5. The isotherms of all the three samples have significant hysteresis loops, which are associated with the filling and emptying of mesopores by the condensate. It is shown that the ZnO/Al$_2$O$_3$ with Zn to Al ratio of 1:2 has the smallest pore size and the narrowest pore size distribution (Fig. 6-5 b). The pore sizes are in the range of 5-10 nm. With increasing Zn concentration, the pore size increased and the distribution was considerably broadened. When the Zn to Al ratio is 1:1 and 2:1, the pore sizes are in the range of 5-25 nm.

The BET surface area and the pore size distribution derived from nitrogen physisorption are listed in Table 6-2. It can be seen that the increase of Zn concentration leads to a decrease of the BET surface area. A maximum surface area of 144 m^2 g^{-1} was obtained for ZnO/Al$_2$O$_3$ of Zn:Al=1:2, which also exhibited the smallest pore size and the most narrow size distribution. The maximum pore volume is exhibited by the sample of Zn:Al=1:1 (Table 6-2).

Table 6-2: Characteristic of the porous ZnO/Al$_2$O$_3$ with different Zn to Al ratios.

ZnO / Al$_2$O$_3$ (Zn:Al)	BET surface area (m^2 g^{-1})	Pore volume (cm^3 g^{-1})
1:2	144	0.36
1:1	134	0.54
2:1	116	0.42

6.4 Conclusions

In conclusion, a sol-gel route was developed to prepare nanostructured porous ZnO/Al$_2$O$_3$. It was found that ZnO can be atomically dispersed in Al$_2$O$_3$ in a wide range of Zn concentrations. A high Al$_2$O$_3$ content leads to amorphous ZnO with a high specific surface area and small pores. However, the maximum pore volume was obtained at a Zn:Al ratio of 1:1. As a result, the nanostructure of the oxides can be fine-tuned by the Zn to Al ratio. The obtained atomically-mixed bi-metallic oxides are very promising as supports for metal catalysts such as Cu.

7 CuO/Al$_2$O$_3$, Cu/ZnO/Al$_2$O$_3$ xerogel and aerogel

7.1 Introduction

The synthesis of methanol from CO$_2$/CO/H$_2$ using Cu/ZnO/Al$_2$O$_3$ catalysts is an important industrial process [33]. Conventionally, such catalysts are prepared by thermolysis of co-precipitated carbonates or oxalates [158]. Chemical vapor deposition (CVD) was also used to prepare Cu/ZnO catalysts for methanol synthesis. The sol-gel method is widely used for the preparation of high-surface-area metal oxide catalysts. A novel sol-gel technique using epoxides as gelation initiators was reported for the preparation of transition and main-group metal oxide aerogels, xerogels and nanocomposites, such as Fe$_2$O$_3$, Al$_2$O$_3$ and Cr$_2$O$_3$ [155, 60, 153]. This chapter presents the preparation of Cu/ZnO/Al$_2$O$_3$ xerogel and aerogel catalysts by the sol-gel route with propylene oxide as gelation initiator.

7.2 Experimental

7.2.1 Preparation of CuO/Al$_2$O$_3$ and CuO/ZnO/Al$_2$O$_3$ xerogels and aerogels

Preparation of wet gels

Cu(NO$_3$)$_2$·3 H$_2$O, Zn(NO$_3$)$_2$·6 H$_2$O, and Al(NO$_3$)$_3$·9 H$_2$O were used as metal precursors and propylene oxide was used as the gelation initiator. Metal nitrates of different compositions were dissolved in ethanol or a mixture of ethanol and water (1:1, volume ratio) to give a clear solution of total metal ion concentration of 1 mol L^{-1}. Propylene oxide was then added to the solution. The molar ratio of propylene oxide to the sum of the metal ions was 10:1. After stirring for 10 min at room temperature, the reaction mixture was transferred into a closed vessel. A blue gel formed in 30-60 min depending on the type of the solvent, i.e., ethanol or its mixture with water. This wet gel was allowed to age at room temperature for 24 h in the closed vessel.

Preparation of air-dried xerogels

The obtained wet gel was soaked in a bath of absolute ethanol for 24 h to exchange the water from the pores of the gel. In addition to the water used as solvent, water was also generated from the crystal water of the starting salts. The exchange of water with ethanol was performed

twice. The xerogels was then obtained after drying of the gel under air for 5-6 days at room temperature.

Preparation of CO$_2$-dried aerogels

For the preparation of the aerogel, the obtained wet gel was soaked in a bath of acetone for 24 h to exchange the ethanol and water from the pores. The exchange was repeated twice. A CO$_2$ critical point drier (BAL-TEC, CPD 030) was then used to dry the wet gel. The acetone in the pores was extracted with liquid CO$_2$ for 6-8 times at 10 °C and 5.0 MPa. After that, the temperature was increased to 40 °C and the pressure to 7.5 MPa to give supercritical CO$_2$. The autoclave was then depressurized in about 1 h to give the blue aerogel.

Calcination of the xerogels and aerogels

The dried xerogels and aerogels were calcined under dynamic air in a tubular furnace to obtain the corresponding metal oxide mixtures. The samples were heated to 400 °C at a rate of 5 K min^{-1}. The calcination was performed for 3 h and then the furnace was allowed to cool freely to room temperature.

7.2.2 Characterisation

Thermogravimetry (TG) was carried out in the temperature range of 25-1000°C under oxygen atmosphere using a heating rate of 5 K min^{-1}. The evolved gases were monitored online by infrared spectroscopy (IR). The morphology of the thermolysis products was studied by scanning electron microscopy (LEO 420). The structure of the resulting metal oxides was studied by transmission electron microscopy (TEM) with a Philips CM 200 FEG instrument. X-ray powder diffraction (XRD) was carried out at room temperature at beamline B2 in HASYLAB. Extended X-ray absorption fine structure (EXAFS) spectroscopy was carried out at beamline E4 at HASYLAB/DESY in transmission mode at 77 K.

Temperature-programmed reduction (TPR) was carried out for the calcined xerogels. About 0.1 g of the calcined sample was placed in a quartz reactor. The reduction was performed under flowing H$_2$ (4.2 vol% H$_2$ in He) by increasing the temperature up to 240 °C with 1 K min^{-1} and maintaining for 1 h. The active surface area of Cu was determined by N$_2$O reactive frontal chromatography at 300 K [116].

7.2.3 Catalytic activity measurements

Catalytic measurements were performed in a high-throughput 49-parallel channel reactor [117]. The material (100 mg diluted with 200 mg quartz per well) was placed in a sample holder consisting of a stainless steel cartridge closed at the bottom by a stainless-steel sinter metal frit. Prior to the catalytic measurements the materials were reduced with H_2 at 518 K following the procedure for the commercial benchmark catalyst ICI Katalco 51-8. Before measuring the catalytic activity, all samples were equilibrated for 3 h (reaction pressure 4.5 MPa, reaction temperature 518 K, analytic flow 20 mL min^{-1}). The reaction gas consisted of 70 vol% H_2, 24 vol% CO, and 6 vol% CO_2. A double GC system (HP GC 6890) equipped with a methanizer FID was used for online gas analysis. Oxo-product separation (H_3COH, $HCOOCH_3$, $H_3CCOOCH_3$, H_3CCH_2OH) was carried out on a SuppelcoWAX 0.53 mm column and CO, CO_2 and CH_4 were separated on a Carboxen 1006 column. The methanol productivities of all measured samples were compared to the productivity of the industrial benchmark catalyst ICI Katalco 51-8.

7.3 Results and discussion

7.3.1 CuO/Al₂O₃ xerogels

The thermolysis of the copper-aluminum compounds was studied by thermogravimetric analysis coupled with infrared spectroscopy (TG-IR). When heated under oxygen, the decomposition of copper-aluminum compounds started at about 100 °C (Fig. 7.1a). Two steps at about 170 °C and 270 °C can be derived from the TG weight loss curve. The weight loss ceased at about 300 °C. Two exothermal peaks appeared in the DTA curve correspond to the two steps in the weight loss curve, indicating the combined loss of water and residual organics and the oxidative combustion of organic compounds, respectively. The total weight loss was about 60 %. The infrared spectra in Fig. 7-1b correspond to the evolved gas phase during heating. The gases were released in two steps corresponding to the TG results. The release of water (several bands from 3800 to 3500 cm^{-1} and bands from 1800 to 1400 cm^{-1}) and some small molecular hydrocarbons (with C-H bands at around 3000 cm^{-1} and about 1500 cm^{-1}) was detected before 2000 s (about 190 °C). Carbon dioxide (four bands from 3740 to 3590 cm^{-1} and several other bands from 2560 to 2310 cm^{-1}) was detected at elevated temperatures.
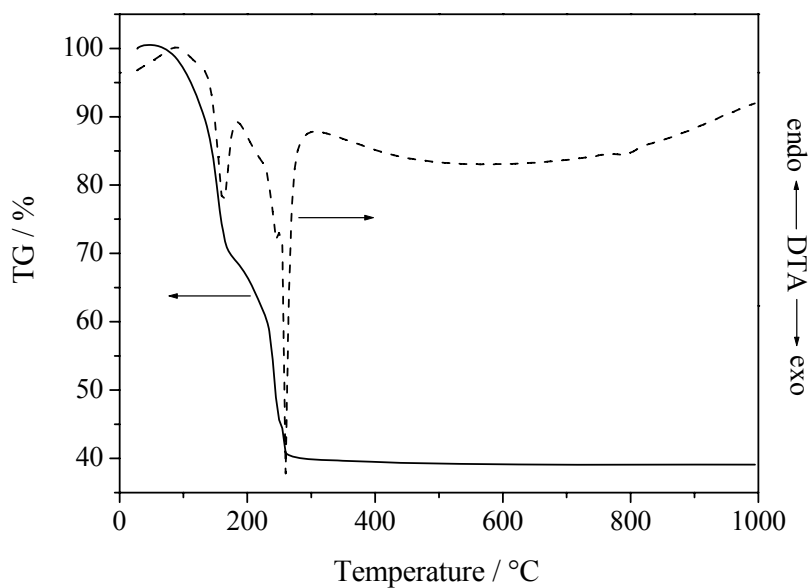
(a)
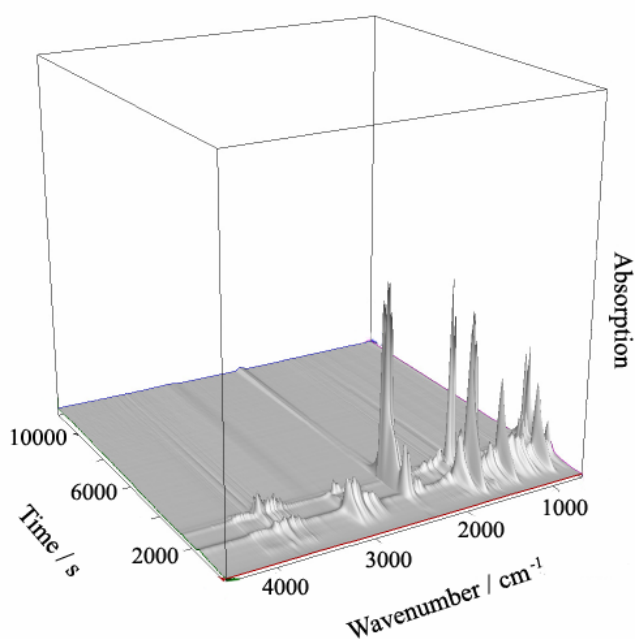
(b)

Fig. 7-1: Thermogravimetry of copper-aluminum compound under oxygen atmosphere (a), and the corresponding time-resolved infrared spectra of the released gases during heating (b) (heating rate 5 K min^{-1}).

The morphology of the CuO/Al$_2$O$_3$ xerogel was studied by scanning electron microscopy. Energy-dispersive X-ray spectrometry (EDX) was performed for elemental analysis (Fig. 7-2). In the Cu/Al$_2$O$_3$ sample, flower-like structures were formed as well as stone-like structures. The EDX results show that CuO dominates in the flower-like structure, whereas Al$_2$O$_3$ is the main component in the stone-like structure.
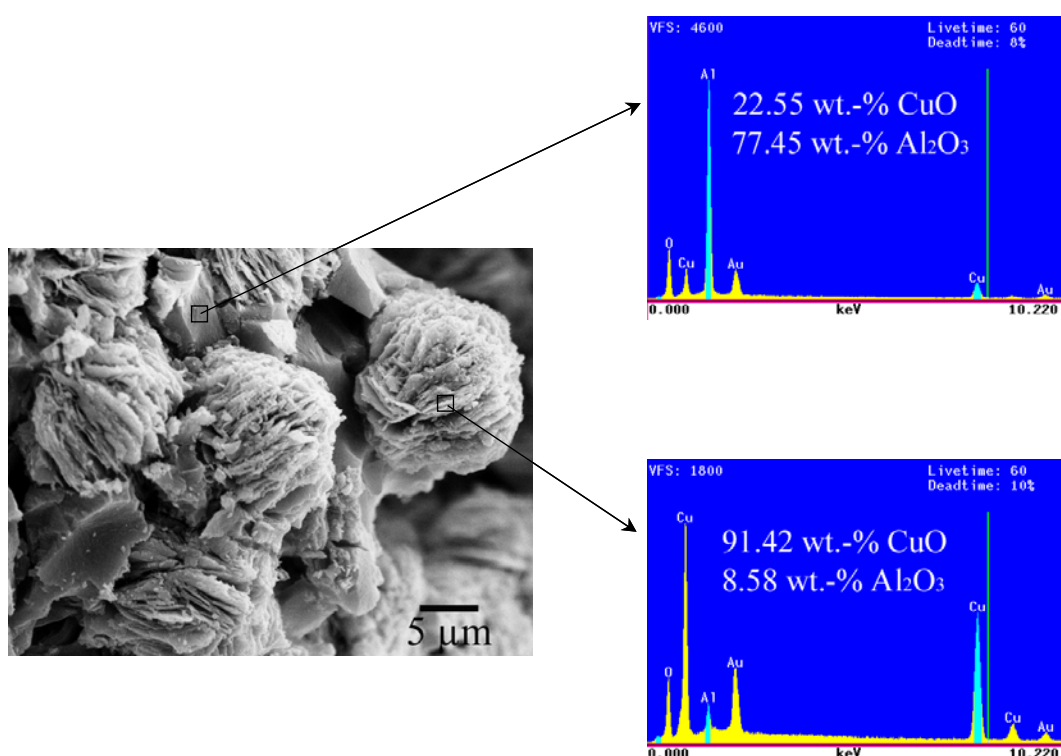
Fig. 7-2: SEM image and EDX results of a CuO/Al$_2$O$_3$ calcined xerogel with a Cu:Al ratio of 1:1.

The XRD patterns of the CuO/Al$_2$O$_3$ xerogels are shown in Fig. 7-3. The increase of CuO concentration was reflected by the increase of the intensities of the peaks corresponding to the crystalline CuO phase. The Al$_2$O$_3$ phase is X-ray amorphous and was not detectable by XRD.
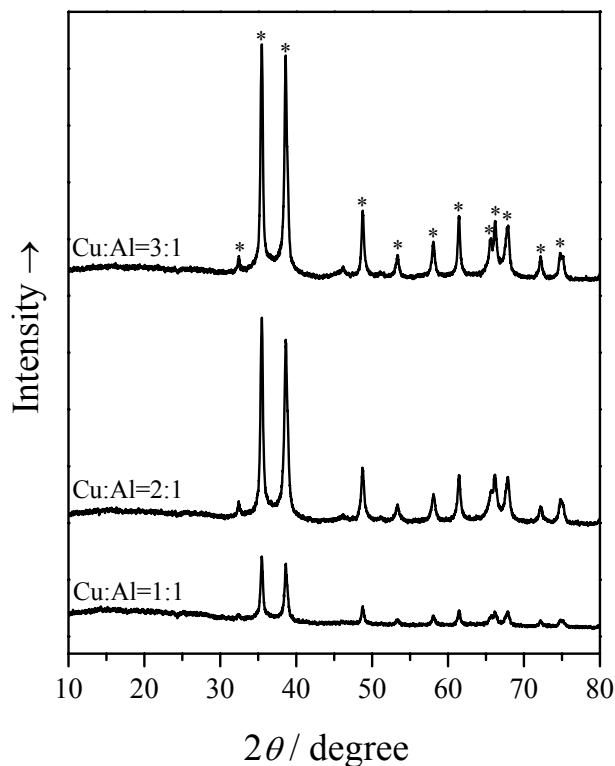
Fig. 7-3: XRD patterns of CuO/Al$_2$O$_3$ calcined xerogels with different Cu:Al ratios. The peaks of CuO are marked by (*).

Table 7-1: Fit parameters of the Cu K-edge EXAFS spectra of CuO/Al$_2$O$_3$ with different Cu:Al molar ratios.

CuO/Al$_2$O$_3$	Cu – 4 O			Cu – 8 Cu		
Cu:Al	R / Å	N	$\sigma^2 \cdot 10^3$ / Å^2	R / Å	N	$\sigma^2 \cdot 10^3$ / Å^2
1:1	1.93	2.9	2.2	2.86	5.7	20.9
2:1	1.94	2.9	0.5	2.87	9.2	25.1
3:1	1.95	2.5	3.5	2.87	7.9	23.7

EXAFS analysis was performed to investigate the short range structure of the CuO/Al$_2$O$_3$ xerogels. Fig. 7-4 shows the Cu K-edge EXAFS raw data and the Fourier transform

magnitudes (FTs) of the oxide mixtures. The first Cu–O shell is present at 1.93–1.95 Å (Table 7-1), with a coordination number of about 3. The Cu–Cu shell is determined at 2.86–2.87 Å (bulk copper oxide about 2.9 Å) [122].

(a)   (b)
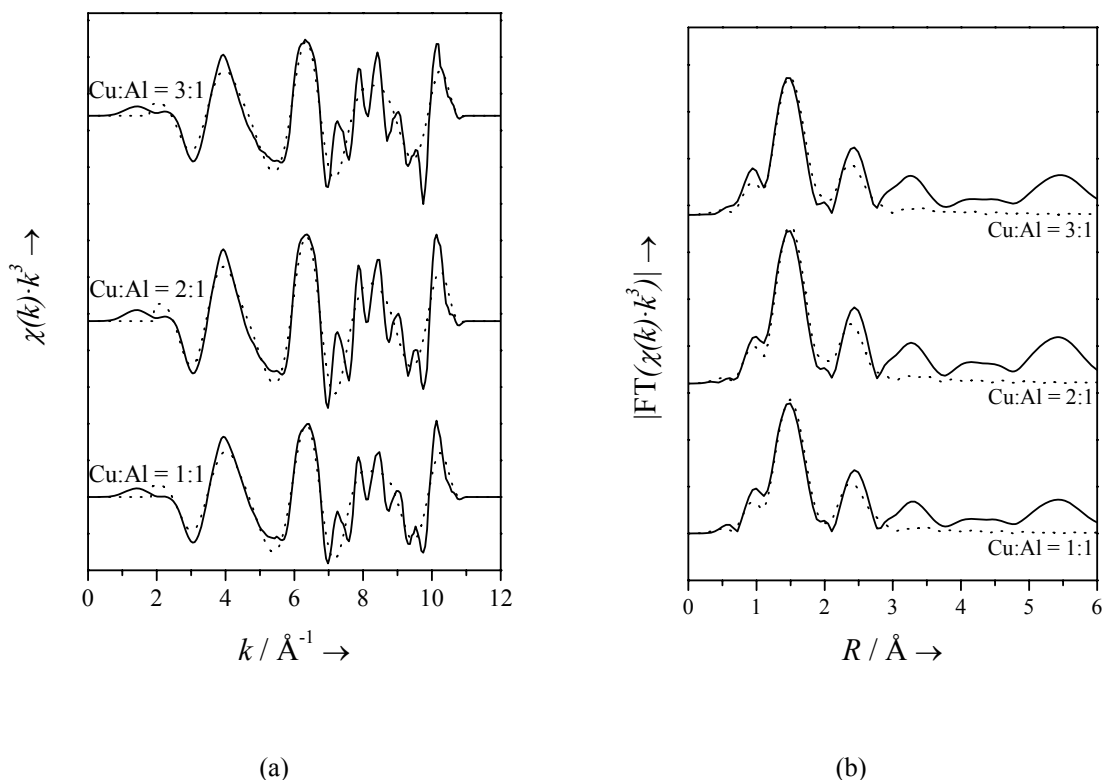
Fig. 7-4: Cu K-edge EXAFS raw data (a) and Fourier transform magnitudes (b) of CuO/Al$_2$O$_3$ with different Cu:Al molar ratios. Solid line: experimental data, dotted line: fit data.

The supported copper oxide with a Cu:Al ratio of 1:1 was examined by temperature-programmed reduction (TPR) in hydrogen. The reduction result is shown in Fig. 7-5. The TPR pattern contains two peaks, indicating two steps in the reduction, presumably from CuO to Cu$_2$O as the first step, and then to Cu as the second step. Table 7-2 shows the Cu-surface area and the catalytic activity of the CuO/Al$_2$O$_3$ sample. The Cu-surface area with Cu:Al ratio of 1:1 was 3.72 m^2 g^{-1}, indicating a low dispersion of Cu on Al$_2$O$_3$. In addition, a lack of a metal-support interaction may account for the low activity for methanol synthesis.
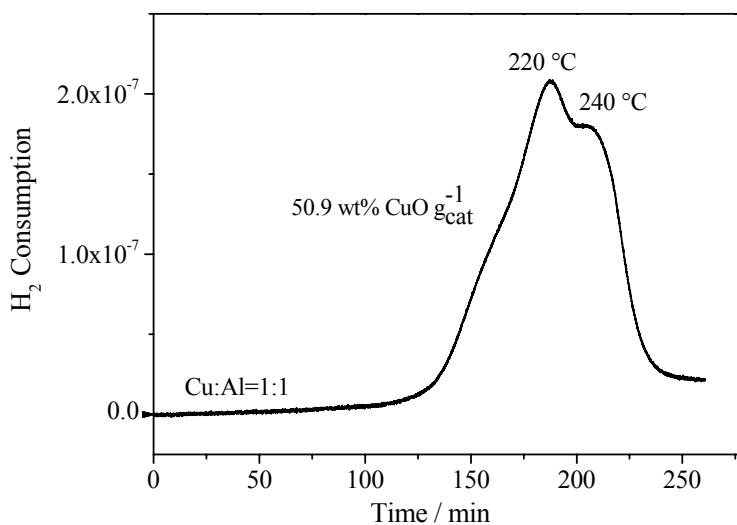
Fig. 7-5: TPR spectra of CuO/Al$_2$O$_3$ calcined xerogels with a Cu to Al molar ratio of 1:1.

Table 7-2: Specific Cu-surface area and catalytic activity of reduced CuO/ Al$_2$O$_3$ calcined xerogel. The activity of the industrial benchmark catalyst (ICI Katalco 51-8) was used as reference and set to 100 %.

CuO/Al$_2$O$_3$	Cu-surface area	Catalytic activity
Cu:Al = 1:1	3.72 m^2 g^{-1}	2.0 % ICI

7.3.2 CuO/ZnO/Al$_2$O$_3$ xerogels

Using ethanol as solvent

The thermolysis of the air-dried Cu-Zn-Al xerogel prepared with ethanol as solvent was studied by TG-IR. When heated under oxygen, the decomposition of the xerogel started at about 100°C and ceased around 300 °C with a total weight loss of about 60 % (Fig. 7-6 a). Two exothermal peaks in the DTA curve correspond to the two steps in the weight loss curve. The first peak appeared at about 160 °C, which can probably be attributed to the combined release of water and small molecular organic molecules like ethanol from the gel preparation. The second exothermal peak at around 260°C is due to the oxidative combustion of residual organic compounds accompanied by the release of carbon oxides.
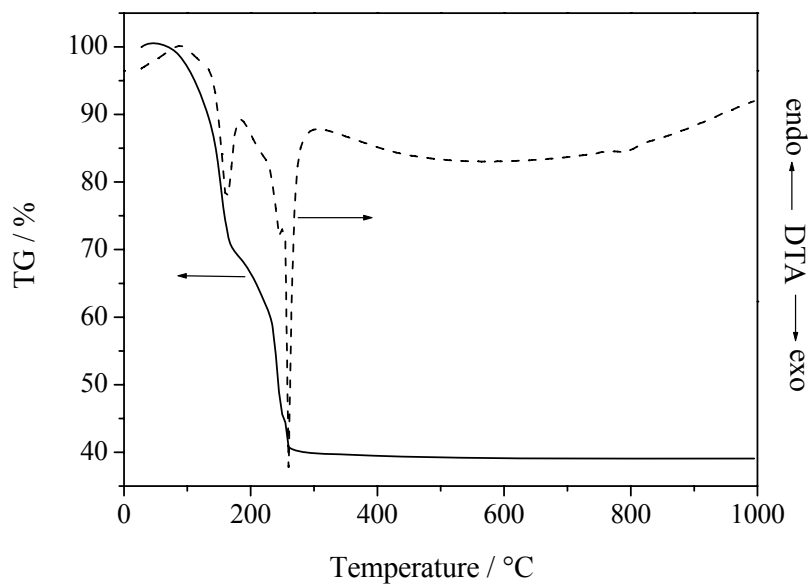
(a)
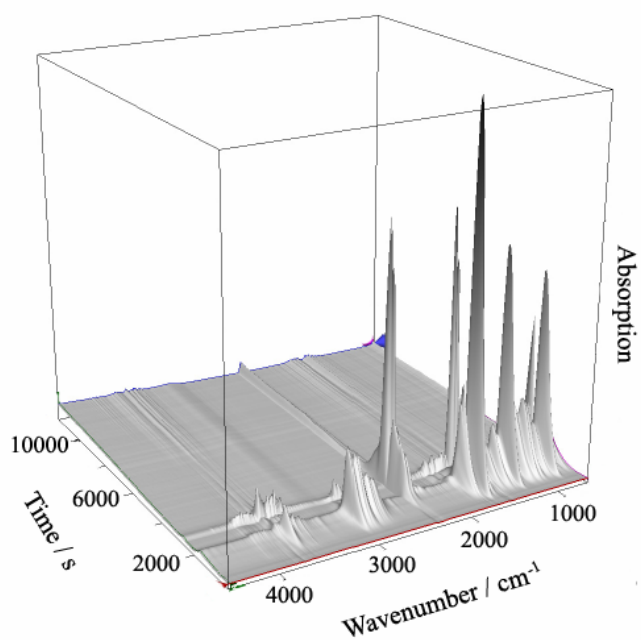
(b)

Fig 7-6: Thermogravimetry of air-dried Cu-Zn-Al xerogel prepared with ethanol as solvent under oxygen atmosphere (a), and the corresponding time-resolved IR spectra of the released gases during the heating with a rate of 5 K min^{-1} (b).

The evolved gas phase during heating was detected by infrared spectroscopy (Fig. 7-6b). The release of gases shows two steps: Before 2000 s (190 °C) the release of water was detected as indicated by bands between 3500 cm^{-1} and 3800 cm^{-1}, as well as bands between 1400 cm^{-1} and 1800 cm^{-1}. Some small molecular weight hydrocarbons appeared also in the first step as indicated by the contributions of C-H at around 3000 and 1500 cm^{-1}. Carbon dioxide (four bands from 3590 cm^{-1} to 3740 cm^{-1} and several bands from 2310 cm^{-1} to 2560 cm^{-1}) and nitrogen oxides (bands at around 2200 cm^{-1}, 1800 cm^{-1}, 1600 cm^{-1} and 1200 cm^{-1}) were subsequently released at elevated temperature.

An SEM image and the EDX analysis of the CuO/ZnO/Al$_2$O$_3$ xerogel calcined at 400 °C are shown in Fig. 7-7. Similar to the CuO/Al$_2$O$_3$ xerogels, two different morphologies were formed in the CuO/ZnO/Al$_2$O$_3$ xerogel, i. e., the flower-like structures as well as stone-like structures. The EDX results show that CuO dominates in the flower-like areas, while ZnO and Al$_2$O$_3$ were the main component in the stone-like areas.
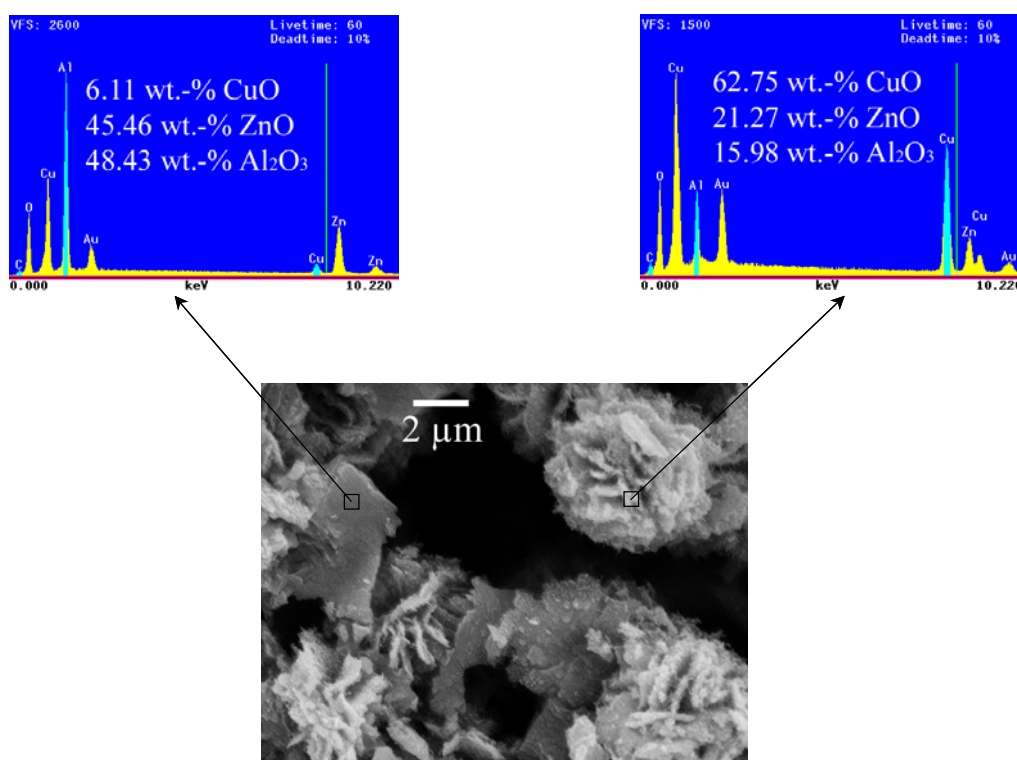
Fig. 7-7: SEM image and EDX results of a CuO/ZnO/Al$_2$O$_3$ calcined xerogel with a Cu:Zn:Al molar ratio of 14:6:10.

The results of XRD studies of the Cu-Zn-Al oxides are shown in Fig. 7-8. In both samples, crystalline copper(II) oxide and zinc oxide were detected, and the Al$_2$O$_3$ phase was X-ray amorphous. With the increase of the amount of Zn, the ZnO peaks become stronger.
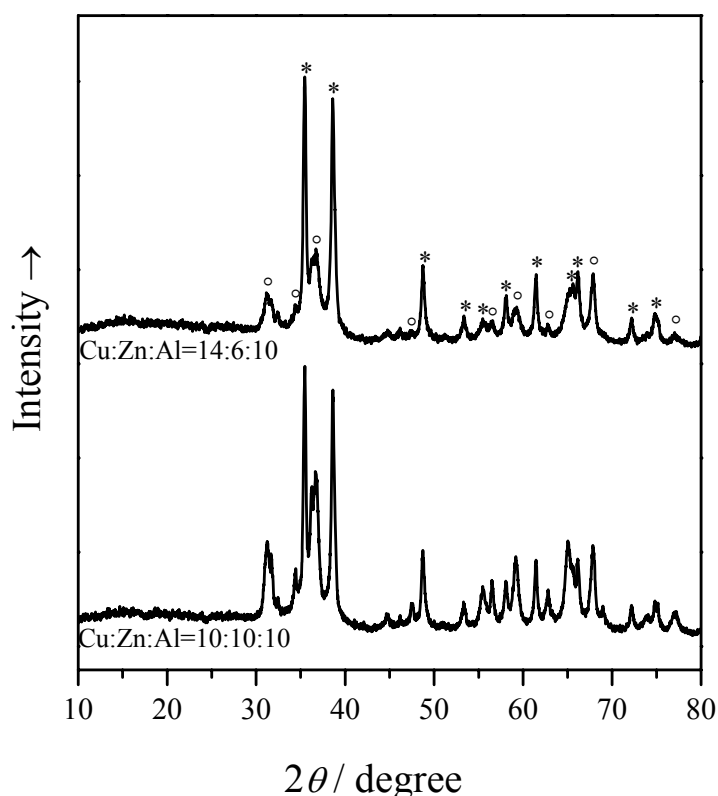
Fig. 7-8: XRD patterns of CuO/ZnO/Al$_2$O$_3$ calcined xerogels with different Cu:Zn:Al ratios prepared with ethanol as solvent. The peaks of CuO are marked by (*), and that of ZnO by (o).

A closer look into the structure of the CuO in CuO/ZnO/Al$_2$O$_3$ samples was obtained by X-ray absorption spectroscopy (EXAFS; Fig. 7-9 and Table 7-3). In the Cu K-edge Fourier transform magnitudes, the shell of Cu–O is detected at 1.95 Å (Table 7-3), with a coordination number of about 2-3. The Cu–Cu shells are determined at 2.87 Å, which are in agreement with that of the bulk copper oxide (about 2.9 Å) [122].

(a)   (b)
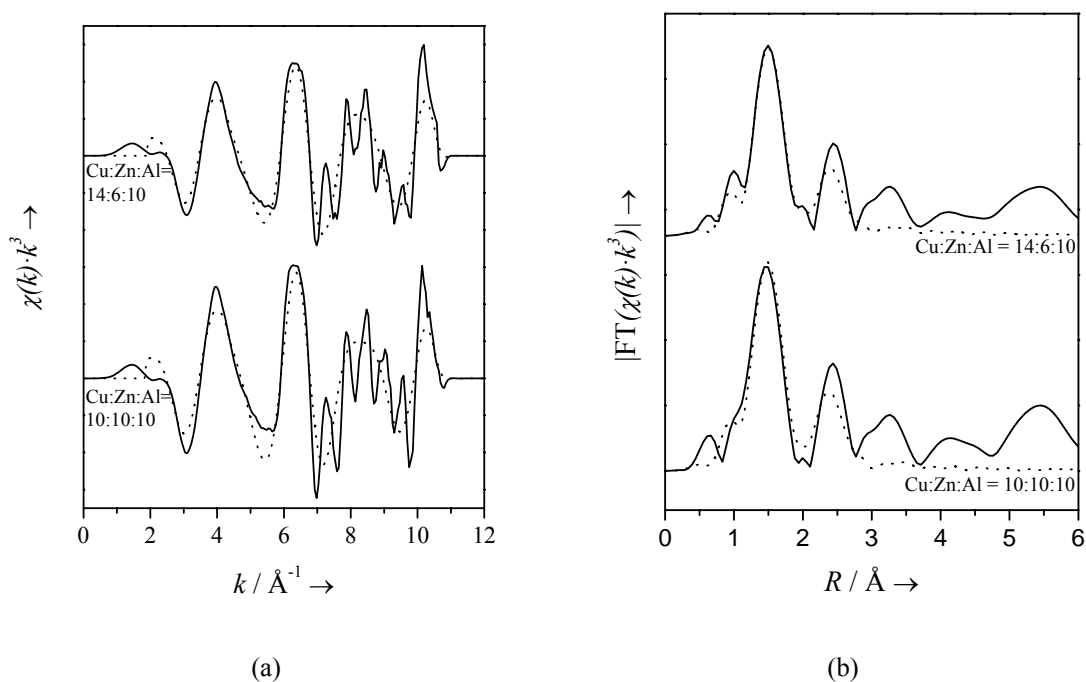
Fig. 7-9: Cu K-edge EXAFS raw data (a) and Fourier transform magnitudes (b) of CuO/ZnO/Al$_2$O$_3$ calcined xerogels with different Cu:Zn:Al molar ratios, prepared with ethanol as solvent. Solid line: experimental data, dotted line: fit data.

Table 7-3: Fit parameters for the Cu K-edge EXAFS spectra of CuO/ZnO/Al$_2$O$_3$ calcined xerogels with different Cu:Zn:Al molar ratios.

CuO/ZnO/Al$_2$O$_3$ Cu:Zn:Al	Cu – 4 O			Cu – 8 Cu		
	R / Å	N	$\sigma^2 \cdot 10^3$ / Å^2	R / Å	N	$\sigma^2 \cdot 10^3$ / Å^2
10:10:10	1.95	3.2	1.6	2.87	9.2	23.4
14:6:10	1.95	2.5	2.2	2.87	10.3	26.9

The EXAFS studies of ZnO in CuO/ZnO/Al$_2$O$_3$ are displayed in Fig. 7-10. In the Zn K-edge Fourier transform magnitudes, the shells of Zn–O are present at 1.93-1.94 Å (Table 7-4), with a coordination number of about 3.5-3.6. The Zn–Zn shells are determined at about 3.5 Å. The coordination numbers of both Zn–O and Zn–Zn were smaller than the crystallographic value

of 4 and 12 [159], which indicates small particles of ZnO. The fraction of surface zinc atoms increases with decreasing particle size, and these surface atoms 'see' less neighbors [129].

(a)   (b)

Fig. 7-10: Zn K-edge EXAFS raw data (a) and Fourier transform magnitudes (b) of CuO/ZnO/Al$_2$O$_3$ calcined xerogels with different Cu:Zn:Al molar ratios, prepared with ethanol as solvent. Solid line: experimental data, dotted line: fit data.

Table 7-4: Fit parameters for the Zn K-edge EXAFS spectra of CuO/ZnO/Al$_2$O$_3$ calcined xerogels with different Cu:Zn:Al molar ratio.

CuO/ZnO/Al$_2$O	Zn – 4 O			Zn – 12 Zn		
Cu:Zn:Al	R/Å	N	$\sigma^2 \cdot 10^3$/Å^2	R/Å	N	$\sigma^2 \cdot 10^3$/Å^2
10:10:10	1.93	3.6	8.1	3.51	2.6	4.9
14:6:10	1.94	3.5	3.9	3.52	8.0	11.5

TPR studies were carried out to determine the reduction behaviour of the oxides with different Cu concentrations. Fig. 7-11 showed the reduction results of the two CuO/ZnO/Al$_2$O$_3$ samples. The TPR patterns of both samples show similar reduction peaks at 197 °C and similar areas under the curve. The increased copper concentration was reflected by the broadened reduction peak, indicating the increase of CuO particle size.
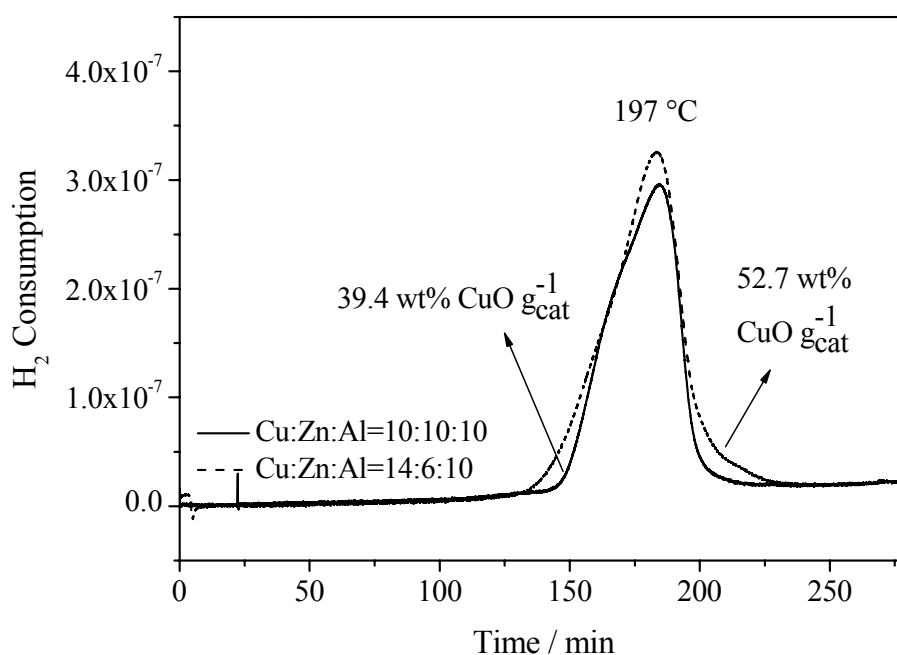
Fig. 7-11: TPR spectra of CuO/ZnO/Al$_2$O$_3$ calcined xerogels with different Cu:Zn:Al molar ratios.

The Cu-Zn-Al oxides were reduced and used as catalysts for methanol synthesis. Table 7-4 shows the specific Cu-surface areas determined by N$_2$O chemisorption and the catalytic activities of the oxide catalysts as compared to industrial methanol synthesis catalysts. A higher catalytic activity is observed compared to the CuO/Al$_2$O$_3$ catalyst, although the Cu surface area is slightly smaller. The presence of ZnO enhanced the metal-support interaction and subsequently increased the catalytic activity. A modest increase of conversion was observed with the increase of copper concentration, although the measured copper surface area was similar.

Table 7-5: Specific Cu-surface areas and catalytic activities of the CuO/ZnO/Al$_2$O$_3$ xerogels. The activity of the industrial benchmark catalyst (ICI Katalco 51-8) was used as reference and set at 100 %.

CuO/ZnO/Al$_2$O$_3$	Specific Cu-surface area	Catalytic activity
Cu:Zn:Al = 10:10:10	2.63 m^2 g^{-1}	4.9 % ICI
Cu:Zn:Al = 14:6:10	2.58 m^2 g^{-1}	5.8 % ICI

Using ethanol and water as solvents

The thermolysis of the copper-zinc-aluminum compound prepared with ethanol and water as solvents was studied by TG-IR. A similar behavior was observed with the sample obtained with ethanol as solvent (see Fig.7.6). The morphology of the CuO/ZnO/Al$_2$O$_3$ xerogel was studied by scanning electron microscopy (Fig. 7-12). As discussed above, the morphology of crystalline (CuO and ZnO) and amorphous (Al$_2$O$_3$) phases can be easily detected in CuO/ZnO/Al$_2$O$_3$ prepared using ethanol as solvent. However, the different phases cannot be detected directly under the microscope for the samples prepared using a ethanol and water as solvent.
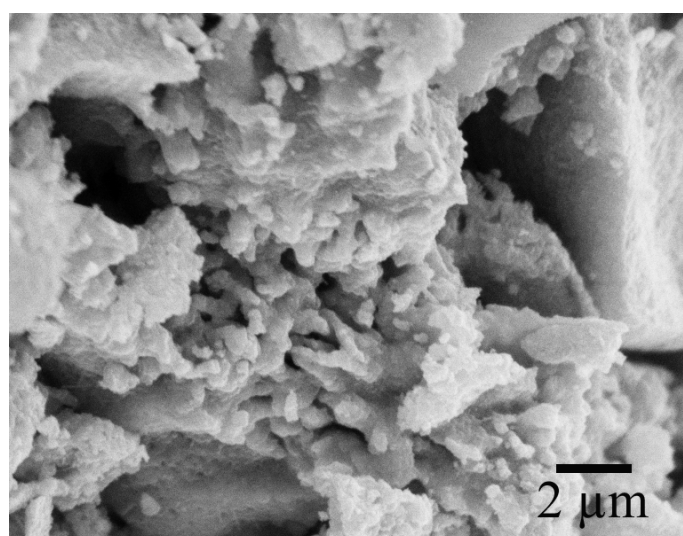
Fig. 7-12: SEM image of CuO/ZnO/Al$_2$O$_3$ calcined xerogel with a Cu:Zn:Al ratio of 2:1:1.
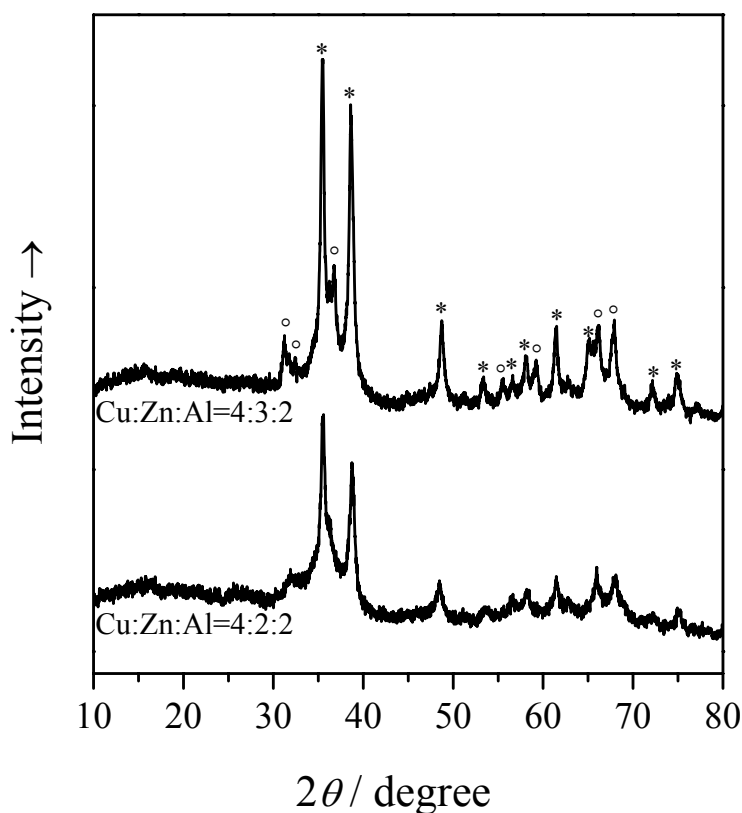
Fig. 7-13: XRD patterns of CuO/ZnO/Al$_2$O$_3$ calcined xerogels with different Cu:Zn:Al ratios, prepared with ethanol and water as solvents. The peaks of CuO are denoted by (*), and those of ZnO by (o).

The phase composition of the Cu-Zn-Al oxides was determined by XRD (Fig. 7-13). The Al$_2$O$_3$ phase was X-ray amorphous and could not be detected by XRD. In both samples, the presence of crystalline copper(II)oxide and zinc oxide was observed. The sample of Cu:Zn:Al=4:2:2 shows very weak and broad ZnO peaks, indicating a very small particle size. The intensities of the peaks of both oxides increased with increasing zinc concentration, as seen in the sample of Cu:Zn:Al=4:3:2.

Fig. 7-14 shows the Cu K-edge EXAFS raw data and the Fourier transform magnitudes (FTs) of the oxide mixtures. The Cu–O shell is found at 1.95 Å (Table 7-6), with a coordination number of about 3. The Cu–Cu shells are determined at 2.87 Å, which is in agreement with that of the bulk copper oxide (about 2.9 Å) [122].
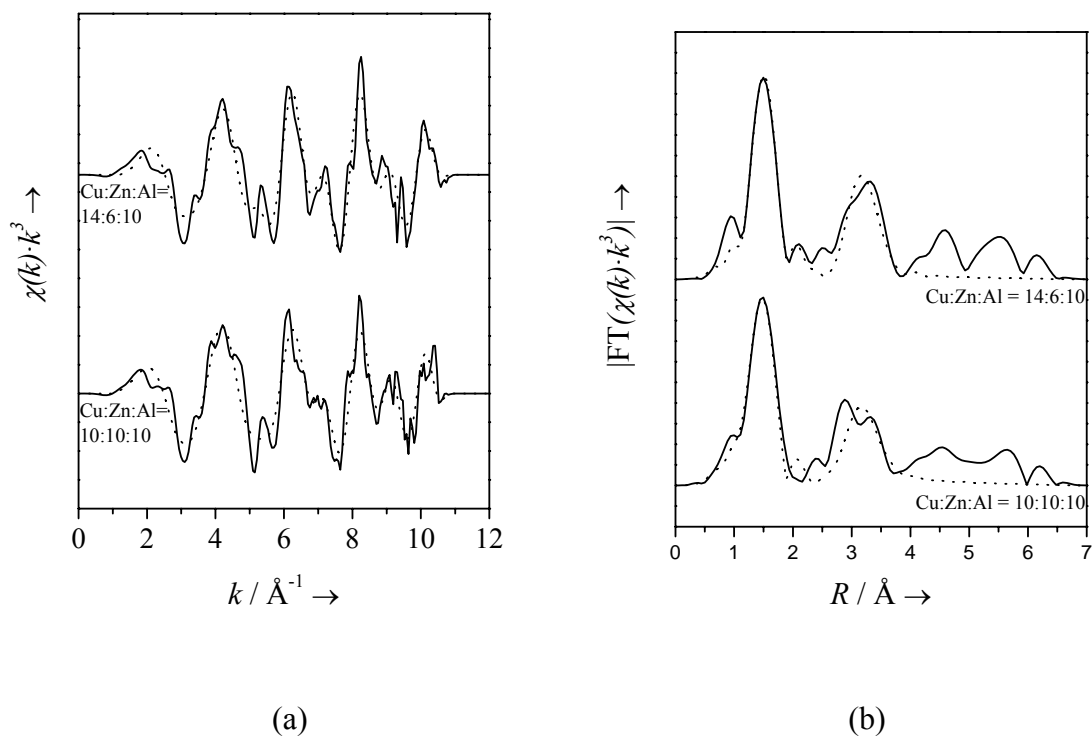
(a) (b)
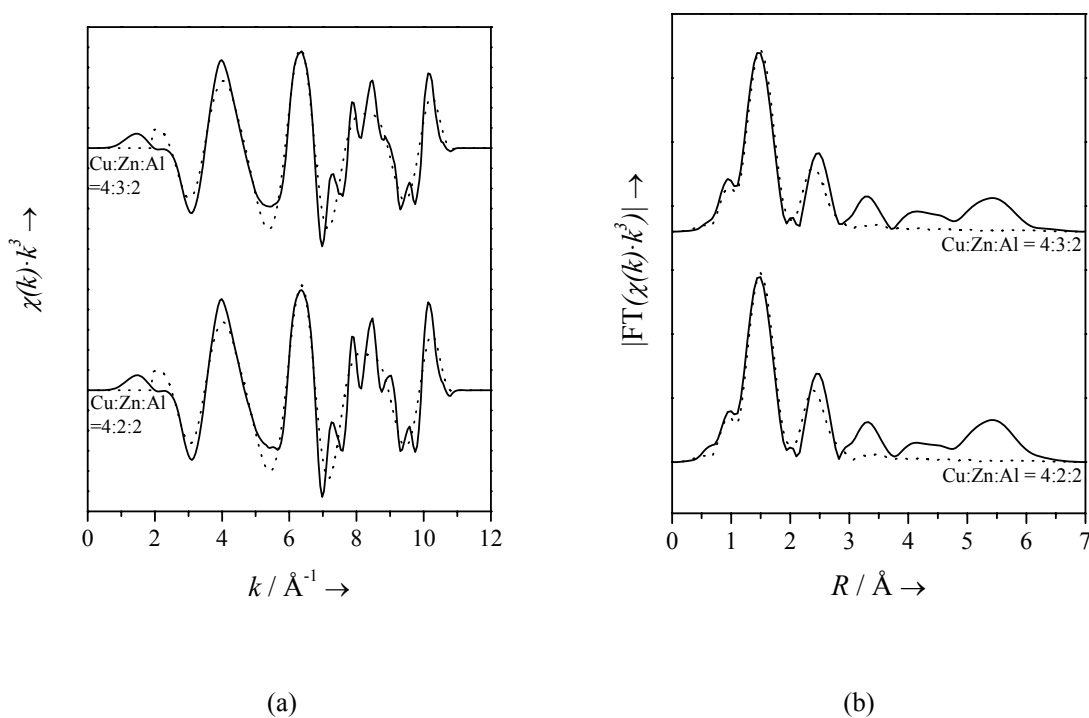
Fig. 7-14: Cu K-edge EXAFS raw data (a) and Fourier transform magnitudes (b) of CuO/ZnO/Al₂O₃ calcined xerogels with different Cu:Zn:Al molar ratios, prepared with ethanol and water as solvents. Solid line: experimental data, dotted line: fit data.

Table 7-6: Fit parameters for the Cu K-edge EXAFS spectra of CuO/ZnO/Al₂O₃ calcined xerogels with different Cu:Zn:Al molar ratios.

CuO/ZnO/Al₂O₃	Cu – 4 O			Cu – 8 Cu		
Cu:Zn:Al	R / Å	N	$\sigma^2 \cdot 10^3$ / Å²	R / Å	N	$\sigma^2 \cdot 10^3$ / Å²
4:2:2	1.95	2.8	1.0	2.87	6.0	20.4
4:3:2	1.95	2.9	1.6	2.87	6.7	23.4

In the Zn K-edge Fourier transform magnitudes, the shells of Zn−O are present at 1.93-1.94 Å (Table 7-7), with a coordination number of about 3.5-4.2. The Zn−Zn shells are determined at about 3.1-3.2 Å. The coordination number of the second shell is 0.8 and 5.0 for the two samples with low and high zinc concentrations, respectively. Both coordination numbers are

much smaller than the crystallographic value of 12 [159], which indicates the small particle size of ZnO.

(a)   (b)
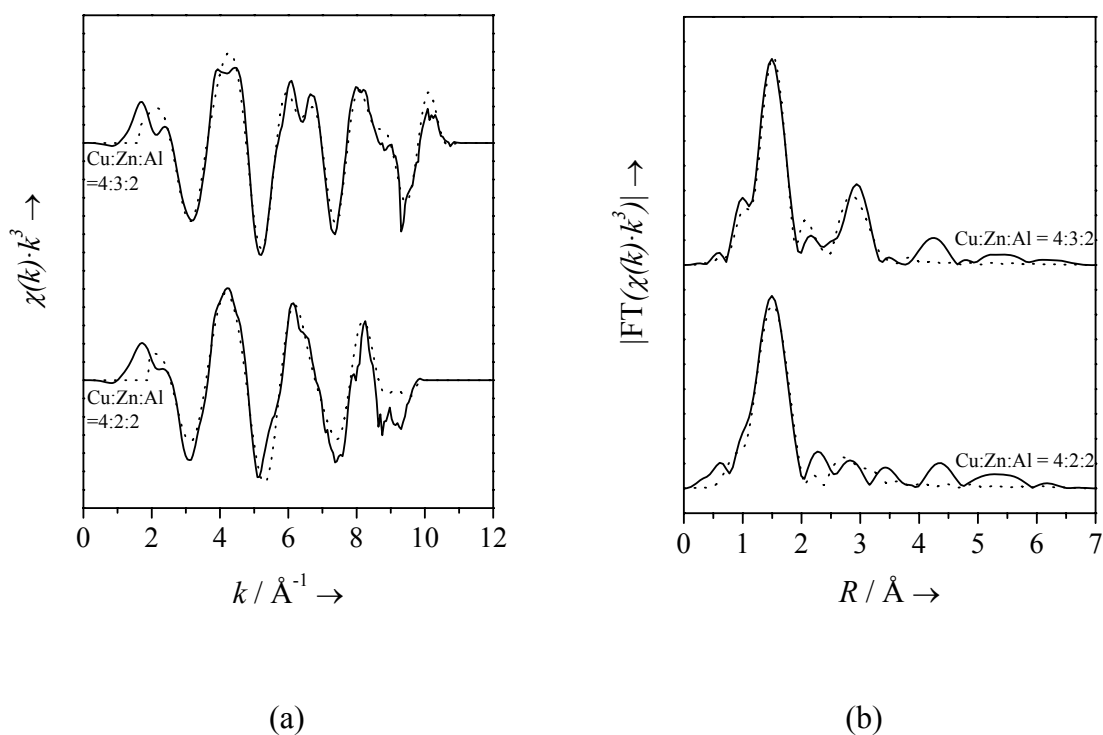
Fig. 7-15: Zn K-edge EXAFS raw data (a) and Fourier transform magnitudes (b) of CuO/ZnO/Al$_2$O$_3$ calcined xerogels with different Cu:Zn:Al molar ratios, prepared with ethanol and water as solvents. Solid line: experimental data, dotted line: fit data.

Table 7-7: Fit parameters for the Zn K-edge EXAFS spectra of CuO/ZnO/Al$_2$O$_3$ calcined xerogel with different Cu:Zn:Al molar ratios.

CuO/ZnO/Al$_2$O$_3$	Zn – 4 O			Zn – 12 Zn		
Cu:Zn:Al	R / Å	N	$\sigma^2 \cdot 10^3$ / Å^2	R / Å	N	$\sigma^2 \cdot 10^3$ / Å^2
4:2:2	1.95	3.6	3.6	3.13	0.8	2.9
4:3:2	1.95	4.2	6.9	3.21	5.0	14.2

The CuO/ZnO/Al$_2$O$_3$ calcined xerogels were studied by TPR (Fig. 7-16). The TPR patterns of both samples contained two peaks, indicating two steps during reduction. The reduction of Cu:Zn:Al=4:2:2 starts from a lower temperature and ends at similar temperature with Cu:Zn:Al=4:3:2. A bigger particle size but narrower size distributions can be derived for the high zinc concentration sample (Cu:Zn:Al=4:3:2), as indicated by the smaller FWHM (full width at half maximum) of the reduction peaks. The samples were used as catalyst for methanol synthesis. The Cu-surface areas and catalytic activities of the CuO/ZnO/Al$_2$O$_3$ catalysts are shown in Table 7-8. Compared to the industrial catalyst, the CuO/ZnO/Al$_2$O$_3$ calcined xerogel with Cu:Zn:Al ratio of 4:2:2 has a smaller copper surface area (about 23 % of the ICI reference catalyst), but the activity related to the copper surface area is very high (around 59 % of ICI).
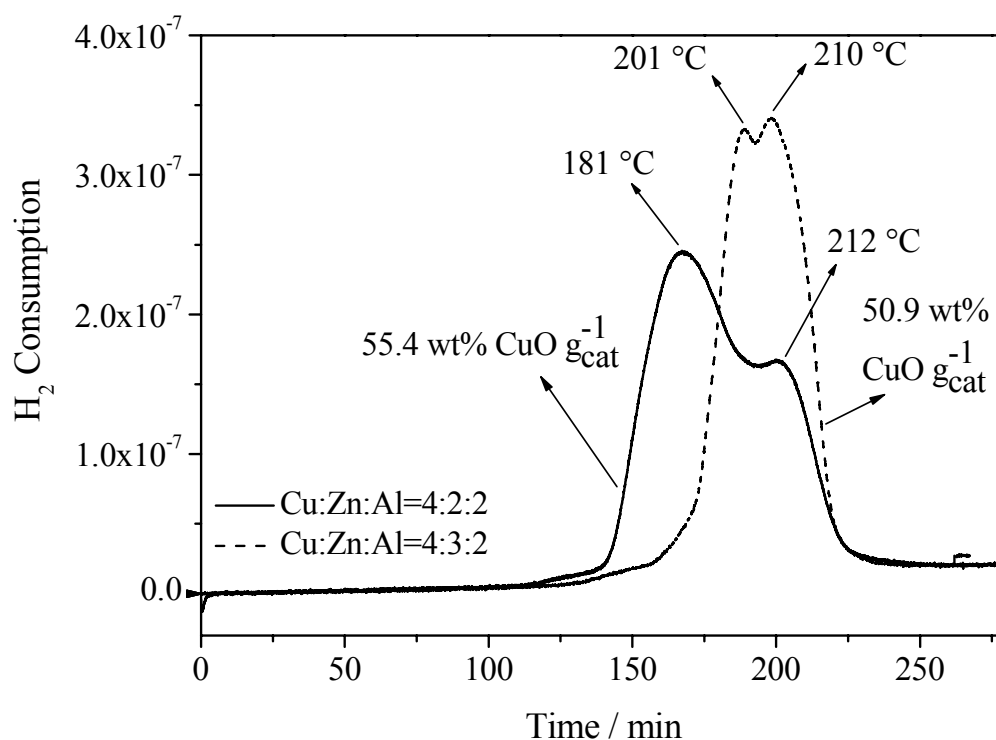
Fig. 7-16: TPR spectra of CuO/ZnO/Al$_2$O$_3$ calcined xerogels with different Cu:Zn:Al molar ratios, prepared with ethanol and water as solvents.

Table 7-8: Specific Cu-surface areas and catalytic activities of the CuO/ZnO/Al$_2$O$_3$ calcined xerogels. The activity of the industrial benchmark catalyst (ICI Katalco 51-8) was used as reference and set at 100 %.

Samples	Specific Cu-surface area	Catalytic activity
CuO/ZnO/Al$_2$O$_3$, Cu:Zn:Al = 4:2:2	4.68 m^2 g^{-1}	58.9 % ICI
CuO/ZnO/Al$_2$O$_3$, Cu:Zn:Al = 4:3:2	5.30 m^2 g^{-1}	--
Industrial reference catalyst (ICI)	23.4 m^2 g^{-1}	100 %

7.3.3 CuO/Al$_2$O$_3$ aerogel

In order to obtain the aerogel of copper-aluminum compound with a low density and a high specific surface area, the obtained wet gel was dried by supercritical CO$_2$. Drying the wet gel gave in partially monolithic blue aerogels (Fig. 7-17), which can be easily ground into powders. The effective density of the Cu-Al aerogel is about 0.9 g cm^3, indicating highly porous structure.

Fig. 7-17: Photograph of the Cu-Al dried aerogel (Cu:Al = 1:1), dried in supercritical CO$_2$.

The calcination of the Cu-Al aerogel was carried out under air at 400 °C. A black CuO/Al$_2$O$_3$ calcined aerogel was thus obtained. The morphology and structure of the CuO/Al$_2$O$_3$ calcined

aerogel were investigated by SEM and TEM (Fig. 7-18). The calcined aerogel was found to be an extended nano-particulate network with small pores. The phase composition of the aerogel was determined by XRD (Fig. 7-19). All the contributions in the XRD pattern could be attributed to crystalline CuO phase.

(a)   (b)
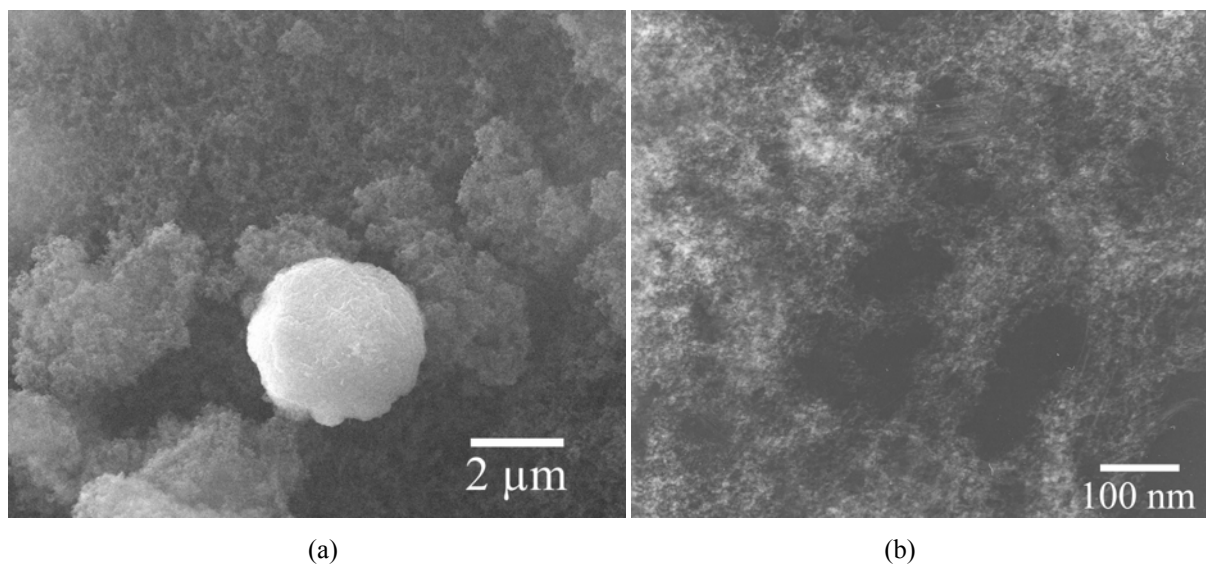
Fig. 7-18: SEM (a) and TEM (b) images of CuO/Al$_2$O$_3$ calcined aerogel (Cu:Al = 1:1).
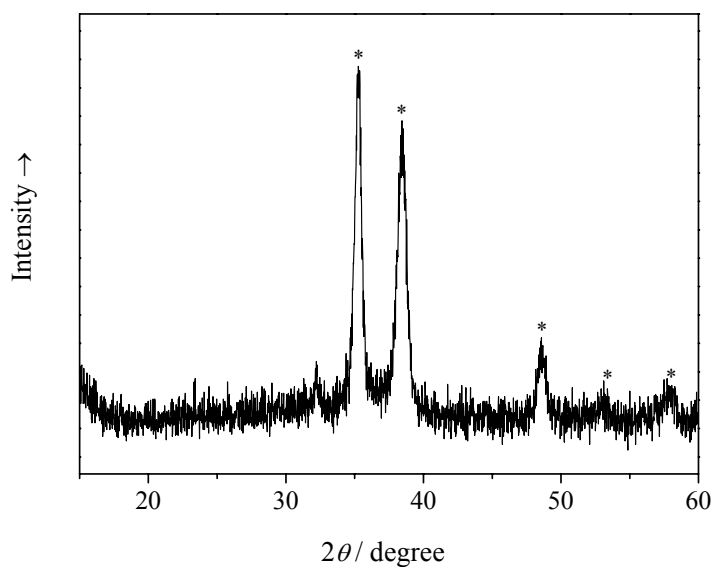
Fig. 7-19: XRD pattern of CuO/Al$_2$O$_3$ calcined aerogel (Cu:Al = 1:1). The marked peaks correspond to CuO (*).

(a)   (b)
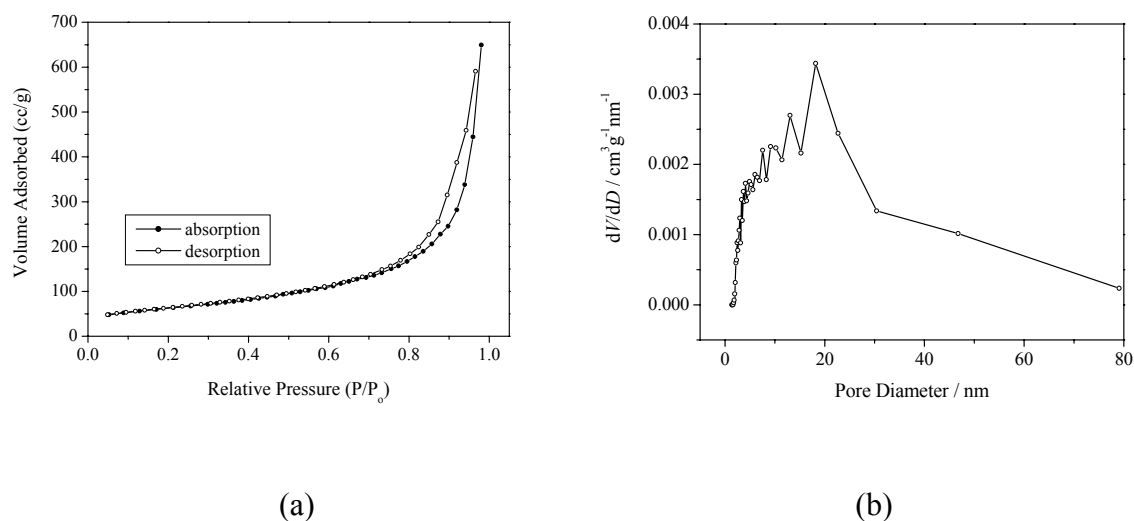
Fig. 7-20: Nitrogen physisorption isotherms (a) and the corresponding pore size distribution (b) of porous CuO/Al$_2$O$_3$ calcined aerogel (Cu:Al = 1:1).

Nitrogen physisorption isotherms and the corresponding pore size distribution of porous CuO/Al$_2$O$_3$ calcined aerogel was shown in Fig. 7-20. The isotherms of the sample have a clear hysteresis loop (Fig. 7-20 a), which is associated with the filling and emptying of the mesopores by the condensate. A relatively broad pore size distribution in the range of 2-30 nm was found (Fig. 7-20 b). The BET surface area and pore volume of the copper-aluminum oxide calcined aerogel are shown in Table 7-9.

Table 7-9: BET surface area and pore volume of the CuO/ Al$_2$O$_3$ calcined aerogel (Cu:Al = 1:1).

Sample	BET surface area	Pore volume
CuO/Al$_2$O$_3$	222.3 m^2 g^{-1}	1.03 cm^3 g^{-1}

7.3.3 CuO/ZnO/Al$_2$O$_3$ Aerogel

The obtained Cu-Zn-Al wet gel was dried by supercritical CO$_2$. The obtained monolithic blue aerogel is very soft with a very low density (Fig. 7-21). The black CuO/ZnO/Al$_2$O$_3$ calcined aerogel was obtained after the thermolysis of the Cu-Zn-Al compounds at 400 °C. A porous network extended by nano-scaled particles was obtained (Fig. 7-22).

Fig. 7-21: Photograph of the Cu-Zn-Al dried aerogel (Cu:Zn:Al = 1:1:1).

(a)   (b)
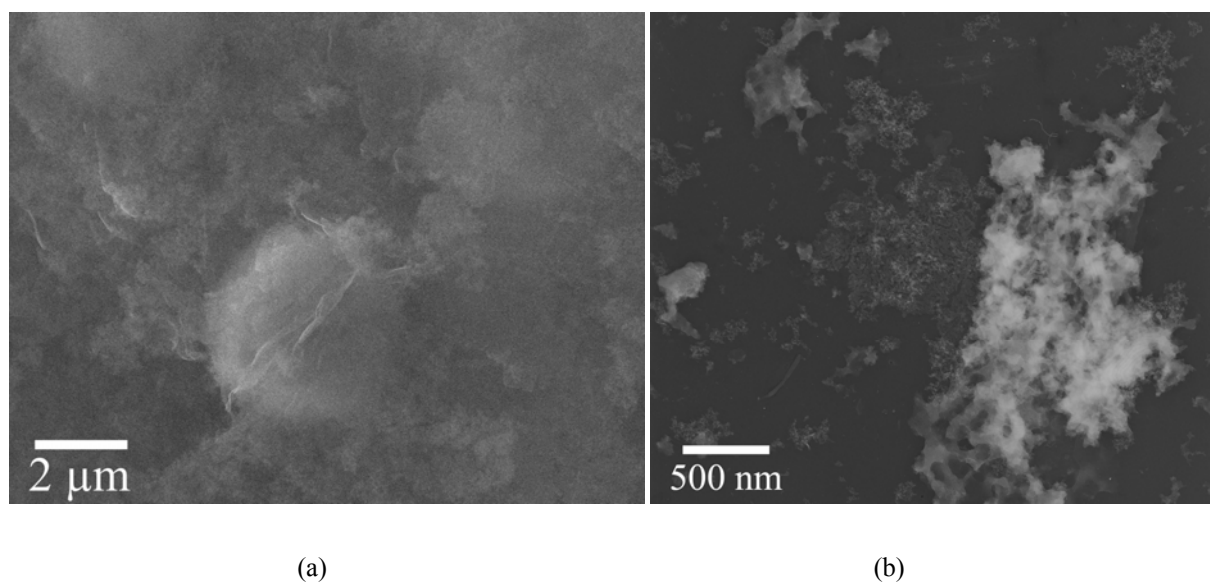
Fig. 7-22: SEM (a) and TEM (b) images of CuO/ZnO/Al$_2$O$_3$ calcined aerogel (Cu:Zn:Al = 1:1:1).

The XRD pattern of the CuO/ZnO/Al$_2$O$_3$ calcined aerogel was shown in Fig. 7-23. CuO and ZnO nanocrystals were detected with broad peaks in the XRD. Nitrogen physisorption isotherms and the corresponding pore size distribution of the CuO/ZnO/Al$_2$O$_3$ aerogel are shown in Fig. 7-24. The hysterisis of the isotherms indicates the presence of porous structures.

The pore size distribution of the calcined aerogel covers a broad range of 2-40 nm. Table 7-10 shows the results of the physisorption, chemisorption and catalytic test for methanol synthesis of the copper-zinc-aluminum oxide aerogel. Compared to the xerogel, the aerogel exhibits both a higher Cu surface area and a higher catalytic activity. The ratio of catalytic activity to Cu surface area is similar to industrial benchmark catalysts (Cu surface area: 23.4 m^2 g^{-1}) [160].
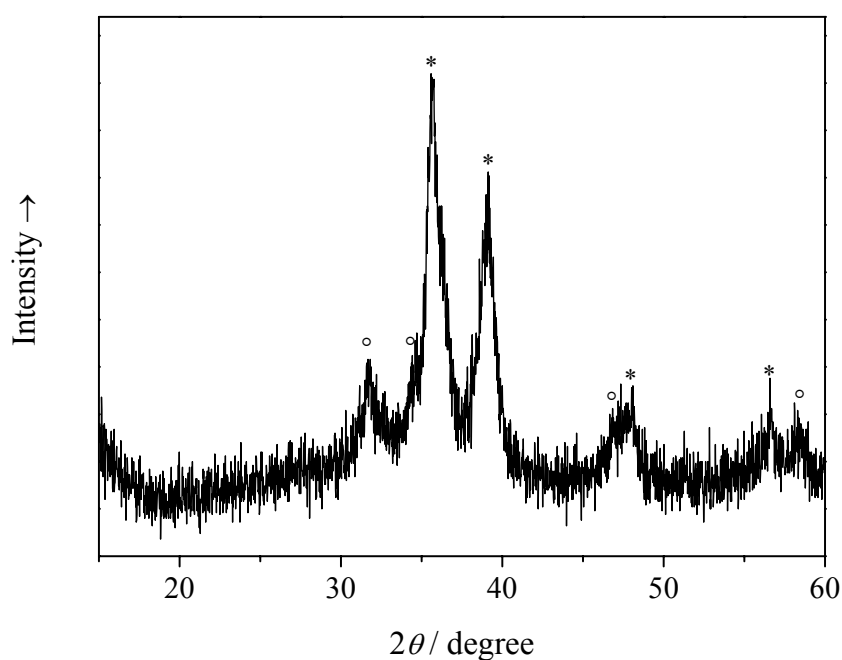
Fig. 7-23: XRD pattern of the CuO/ZnO/Al$_2$O$_3$ calcined aerogel (Cu:Zn:Al = 1:1:1). The marked peaks correspond to CuO (*) and ZnO (o).

Table 7-10: Physisorption, chemisorption and catalytic test of the CuO/ZnO/Al$_2$O$_3$ aerogel (Cu:Zn:Al =1:1:1). The activity of the industrial catalyst (ICI Katalco 51-8) was used as reference and set to 100 %.

Sample	BET surface area	Pore volume	Cu-surface area	Catalytic activity
CuO/ZnO/Al$_2$O$_3$	175.0 m^2 g^{-1}	0.851 cm^3 g^{-1}	6.0 m^2 g^{-1}	22 % ICI
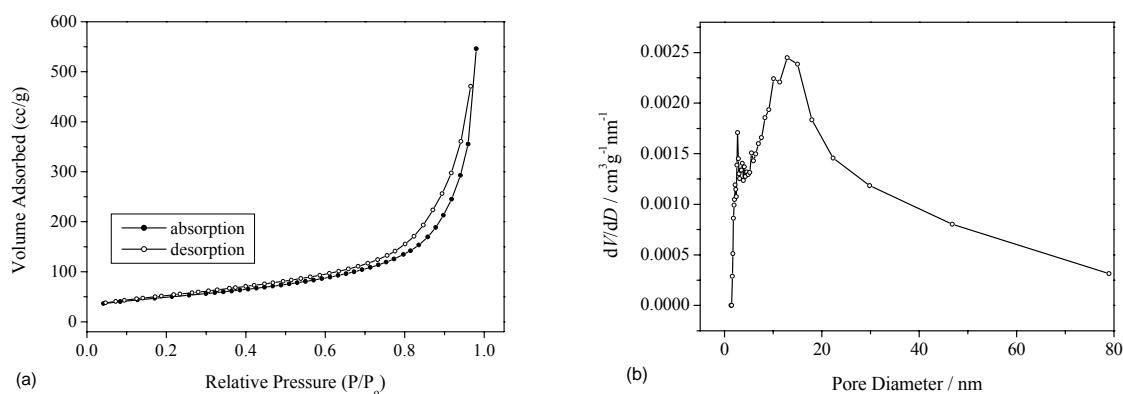
Fig. 7-24: Nitrogen physisorption isotherms (a) and the corresponding pore size distribution (b) of the porous CuO/ZnO/Al₂O₃ calcined aerogel (Cu:Zn:Al = 1:1:1).

7.4 Conclusions

In summary, a new straightforward sol-gel method was employed to prepare porous CuO/Al₂O₃ and CuO/ZnO/Al₂O₃ using propylene oxide as gelation initiator. Cu-Al and Cu-Zn-Al precursor xerogels and aerogels were prepared by drying the wet gel under air and in the supercritical carbon dioxide, respectively. After thermolysis at 400 °C, CuO/Al₂O₃ and CuO/ZnO/Al₂O₃ xerogels and aerogels were obtained, which were used as catalysts for the synthesis of methanol. The optimised CuO/ZnO/Al₂O₃ (Cu:Zn:Al=4:2:2) xerogel has a catalytic activity of about 59 % of the industrial reference catalyst. The porous aerogels prepared with this method showed a very high specific surface area.

8 Preparation of ZnO, CuO and CuO/ZnO by an easy solution route

8.1 Introduction

Zinc oxide is an important material that can be used in catalysts, sensors, pigments, electrographs, and medical materials, etc. [161]. Many methods for the synthesis of ZnO nanostructures have been reported, including chemical vapor deposition (CVD) [162, 163], sputter deposion [164], and thermal evaporation [165, 166]. Various electrochemical and homogenous precipitation processes to prepare ZnO particles and films from aqueous solution have also appeared. Perpendicularly orientated ZnO nanorods were grown on thin ZnO templates from an aqueous solution of zinc salts in the presence of hexamethylenetetramine [167]. Uekawa et al. [124] reported a method of preparing ZnO crystallites by heating aqueous solutions containing $Zn(OH)_4^{2-}$ ions at 348 or 368 K. One dimensional needle-like ZnO nanowhiskers were synthesized directly from aqueous solution of $Zn(OH)_4^{2-}$ in the presence of sodium dodecyl sulfate (SDS) [168]. A homogenous aqueous solution containing $Zn(OH)_4^{2-}$ ions is formed from $Zn(OH)_2$ under strongly basic conditions. Li et al. [169] considered that $Zn(OH)_4^{2-}$ is one of the intermediate species of the transition from $Zn(OH)_2$ to ZnO. Thus, solutions which contain $Zn(OH)_4^{2-}$ ions can be suitable precursors of zinc oxide particles and films.

CuO has been widely used for various applications such as heterogeneous catalysts, gas sensors, magnetic storage media, solar-energy transformation, and field emission emitters [170-173]. In the past decades, many efforts have been made on the fabrication of nanostructured CuO. Particularly, a variety of CuO nanostructures were synthesized by high temperature approaches [174, 175] and low temperature wet chemical methods [176, 177]. $Cu(OH)_2$ has been frequently used as the precursors for the preparation of CuO nanostructures. Lu et al. [178] reported the preparation of CuO nanostructures, such as CuO nanoplatelets, nanoleaflets, and nanowires by thermal dehydration of the $Cu(OH)_2$ in solution and in solid state.

Reverse microemulsions formulated with sodium bis(2-ethylhexyl) solfosuccinate (NaAOT) have been extensively used for the synthesis of inorganic nanoparticles, such as barium chromate, calcium sulfate, and silica [179-182]. Li et al.[183] studied the growth of crystalline micrometer-long $BaSO_4$ fibers prepared with NAOT. The growth mechanism was proposed

and shown in Fig. 8-1. Initially, intramicellar nucleation leads to self-limiting fusion and exchange through reductions in membrane fluidity due to surface adsorption. This controls the size and monodispersity of the surfactant-encapsulated amorphous $BaSO_4$ nanoparticles and enhances their intermicellar association into loosely associated aggregates that slowly transform internally into coaligned bundles of 5-nm-wide nanofilaments. The filaments grow through the linear coalesence and fusion of the primary nanoparticles building blocks, which results in displacement of AOT molecules and formation of a surfactant bilayer between the $BaSO_4$ threads. The high anisotropy could be driven by strong coupling of lattice and curvature energies especially for linear association, and propagated by differences in the ease of displacement of bound and unbound surfactant molecules along the edges and tips of the developing filament.
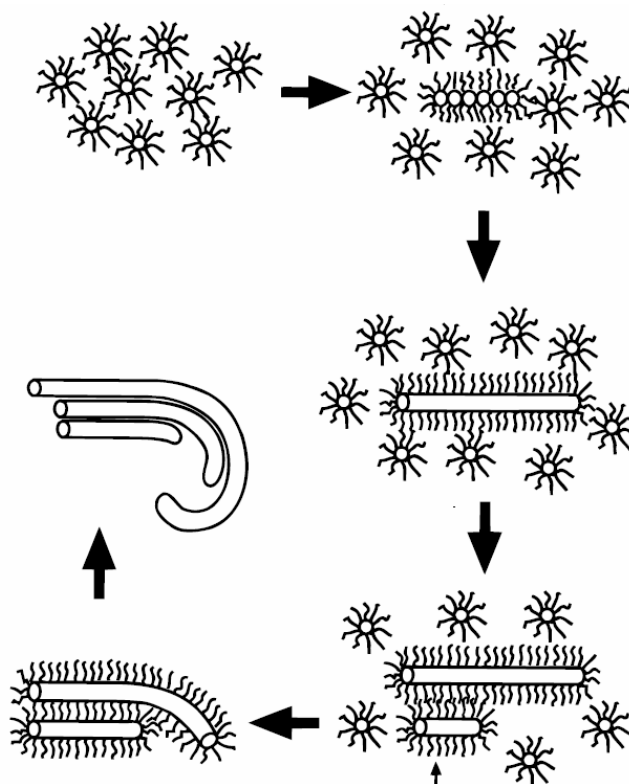
Fig. 8-1: Proposed model for the formation of the $BaSO_4$ nanofilament bundles [183].

In the work presented here, copper oxide, zinc oxide and copper-zinc bimetallic oxides were prepared by heating the respective metal hydrate aqueous solutions at low temperature. The effect of NaAOT and the influence of solvents on the morphology of the products was investigated.

8.2 Experimental

8.2.1 Preparation of CuO

Without NaAOT

The aqueous solutions of $CuSO_4$ and NaOH with concentrations from 0.025 to 0.2 mol L^{-1} were pumped into a stirred precipitation vessel at room temperature (Fig. 8-2). A blue $Cu(OH)_2$ precipitation was formed immediately. After 3 min of further stirring, the solution was transferred to a sealed vessel followed by heat treatment at 80 °C for 3 h. After that, the black precipitate was filtered off, washed with water, and then dried in air for 24 h.
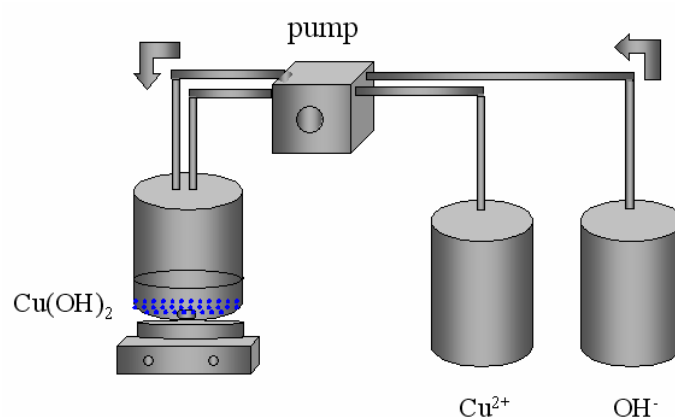
Fig. 8-2: Schematic illustration of the setup for the precipitation of $Cu(OH)_2$.

In the presence of NaAOT

$Cu(NO_3)_2 \cdot 3\ H_2O$ was dissolved in deionised water to form an aqueous solution with a concentration of 0.05 mol L^{-1}. NaAOT was dissolved in water or butanol to form a solution of 0.05 mol L^{-1}. These two solutions were mixed with the volume ratio of 5:1, followed by stirring for 1 h at room temperature. A NaOH solution of 2 mol L^{-1} was added dropwise to the well-stirred solution ($[Cu^{2+}]:[OH^-] = 1:4$). Stirring was continued for further 2 h at room temperature. The resulting solution with blue precipitates was subsequently kept in a sealed vessel at 90 °C for 24 h. After that, the black precipitate was filtered off, washed with water, and then dried in air.

8.2.2 Preparation of ZnO nanostructures

$Zn(NO_3)_2 \cdot 6 H_2O$ was dissolved in deionised water to form a clear aqueous solution of 0.05 mol L^{-1}. NaAOT was dissolved in water or butanol to form a solution of 0.05 mol L^{-1}. These two solutions were mixed with a volume ratio of 5:1, followed by stirring for 1 h at room temperature. A NaOH solution of 2 mol L^{-1} was added dropwise to the well-stirred solution ($[Zn^{2+}]:[OH^-] = 1:4$). After addition, stirring was continued for 2 h at room temperature. The resulting solution was subsequently kept in a sealed vessel at 90 °C for 24 h. The precipitate was then filtered off, washed with water and dried in air.

8.2.3 Preparation of CuO/ZnO nanostructures

$Cu(NO_3)_2 \cdot 3 H_2O$ and $Zn(NO_3)_2 \cdot 6 H_2O$ of different amounts were dissolved in water to give a clear solution with a total metal ion concentration of 0.4 mol L^{-1}. Aqueous solutions of 0.1 mol L^{-1} NaAOT and 2 mol L^{-1} sodium hydroxide were added under stirring, respectively. The solution was stirred continuously for 1.5 h at room temperature, transferred to a sealed vessel, and aged at 90 °C for 5 h. The obtained precipitate was filtered off, washed with water and then dried in air.

8.2.4 Characterization

The morphology of the products was studied by scanning electron microscopy (LEO 420). X-ray diffraction was carried out at room temperature. Extended X-ray absorption fine structure (EXAFS) spectroscopy was performed at 77 K. Both XRD and EXAFS were performed at the Hamburger Synchrotronstrahlungslabor (HASYLAB).

8.3 Results and discussion

8.3.1 CuO

Without NaAOT

CuO nanoleaflets were obtained by thermal dehydration of $Cu(OH)_2$ in solution at low temperature. Fig. 8-3 showed SEM images of the CuO products, which were prepared with different Cu^{2+} and OH^- concentrations. The small particles on the surface of the samples were the sputtered gold particles for SEM measurements. The typical length of the CuO nanoleaflets was about 200-300 nm. The morphology of the CuO samples can be controlled

by changing the ion concentrations of the solutions during the preparation of the $Cu(OH)_2$. With the increase of the concentrations of Cu^{2+} and OH^-, the obtained CuO nanoleaflets became longer and narrower.

(a)   (b)

(c)   (d)
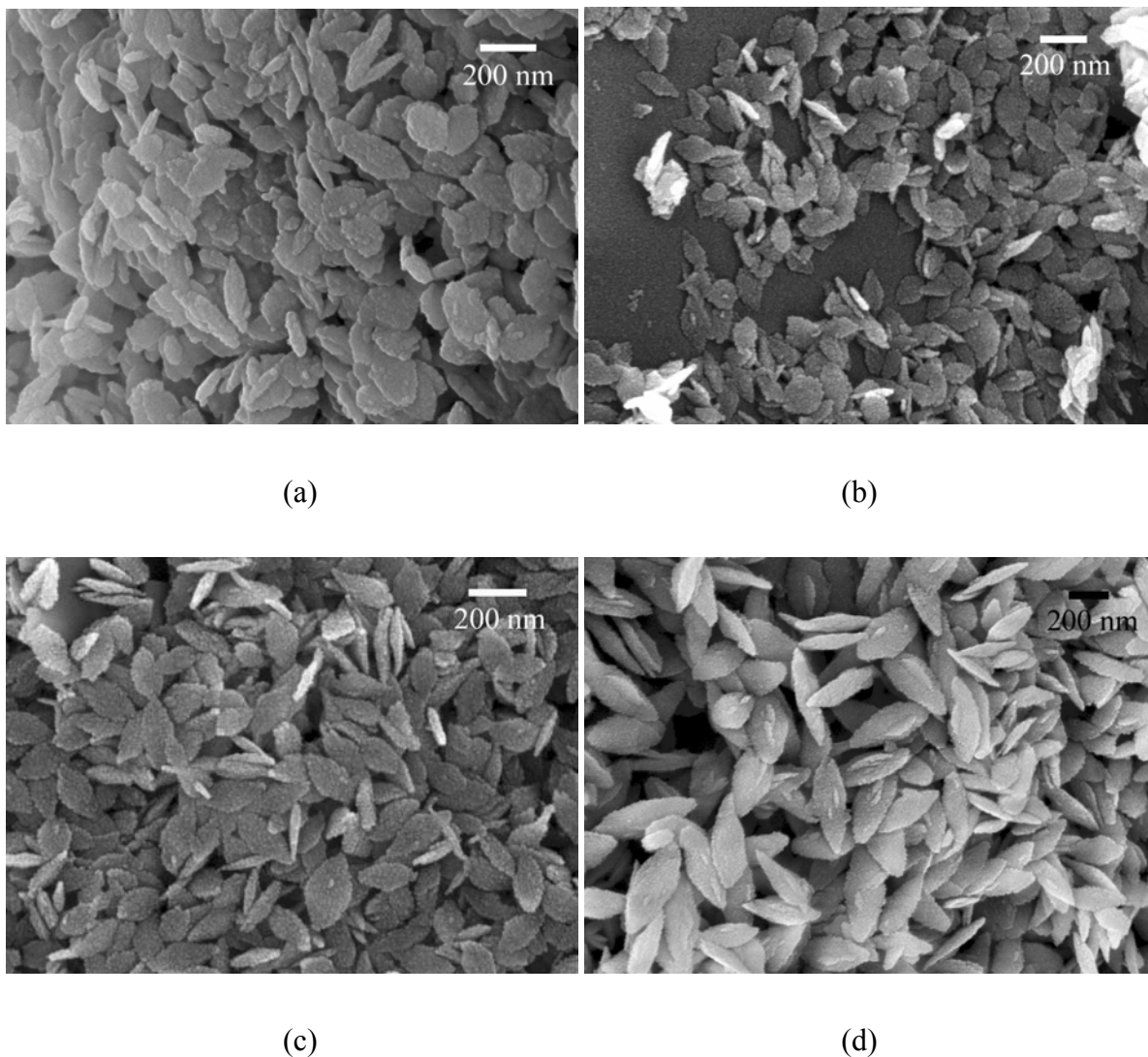
Fig. 8-3: SEM images of CuO nanoleaflets prepared in aqueous solutions with different Cu^{2+} and OH^- concentrations: (a) 0.025 mol L^{-1}, (b) 0.05 mol L^{-1}, (c) 0.1 mol L^{-1}, (d) 0.2 mol L^{-1}.

In the presence of NaAOT

CuO with different morphologies was prepared in different solvents when NaAOT was used during the preparation of $Cu(OH)_2$ precursors. It was found that the solvent had a significant effect on the morphology of the CuO products. CuO platelets of sub-micron dimensions were obtained in aqueous solution (Fig. 8-4 a). When the reaction was carried out in the mixture of water and butanol, CuO crystallized as spherical particles as observed in the SEM image in

Fig. 8-4 b. The principal reason for using microemulsions is that particle sizes and corresponding size distributions can be easily controlled by reaction confinement. The synthesis of inorganic nanoparticles in the presence of NaAOT can produce a variety of multi-length scale superstructures depending on the degree of interaction between the incipient inorganic nucleus and surrounding AOT molecules [184].

(a)   (b)
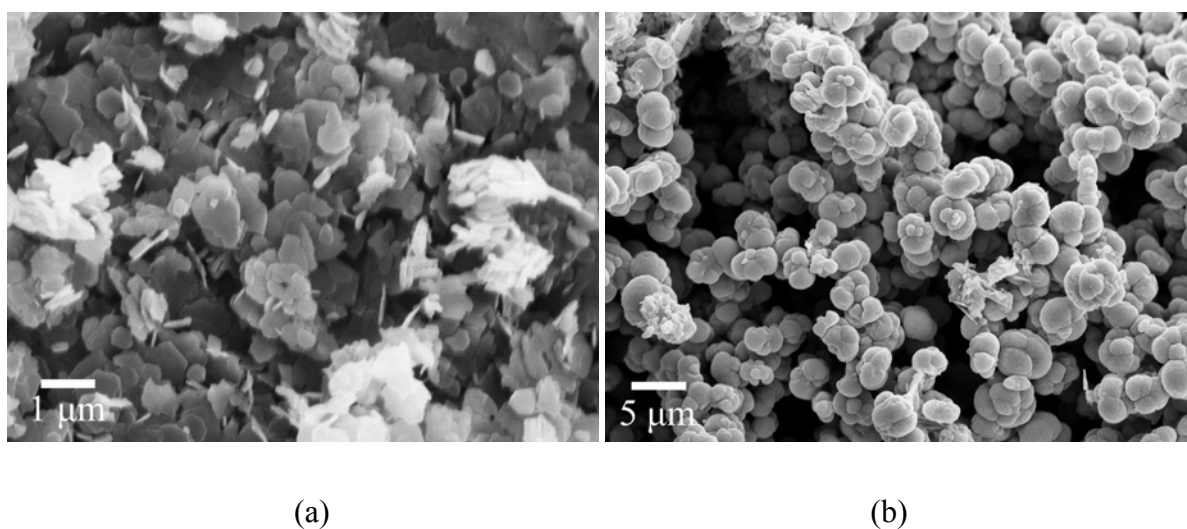
Fig. 8-4: SEM images of CuO prepared in water (a) and in water and butanol (b) in the presence of NaAOT.

8.3.2 ZnO

(a)   (b)
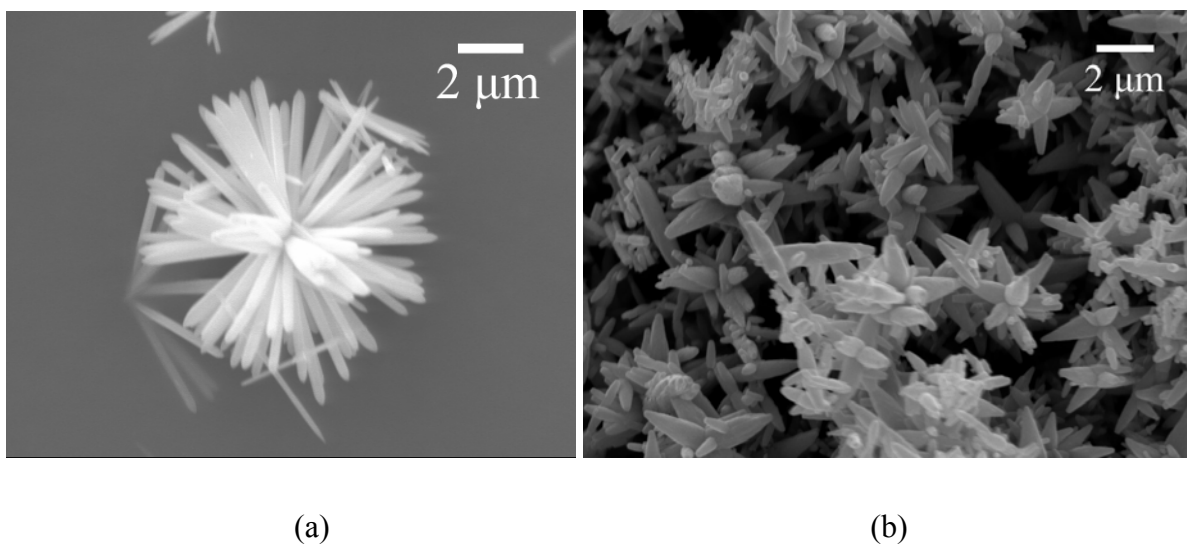
Fig. 8-5: SEM images of ZnO prepared in water (a) and in water and butanol (b) in the presence of NaAOT.

Flower-like ZnO nanostructures consisting of nanorods were obtained by heat treatment of solutions containing $Zn(OH)_4^{2-}$ ions and NaAOT. The morphology of the nanorods can be significantly affected by the solvent. Fig. 8-5 showed the morphology of the flower-like ZnO prepared in water and in a mixture of water and butanol in the presence of NaAOT. Flower-like ZnO consisting of nanorods with a typical length of about 4 μm was obtained in the aqueous solution (Fig. 8-5 a), whereas in water and butanol solution thicker and shorter nanorods with a length of about 2 μm were formed (Fig. 8-5 b). Obviously the nature of the solvent changed the interaction between the inorganic nucleus and the surrounding AOT, and the crystal growth was subsequently affected.

8.3.3 CuO/ZnO

(a) (b)

(c)
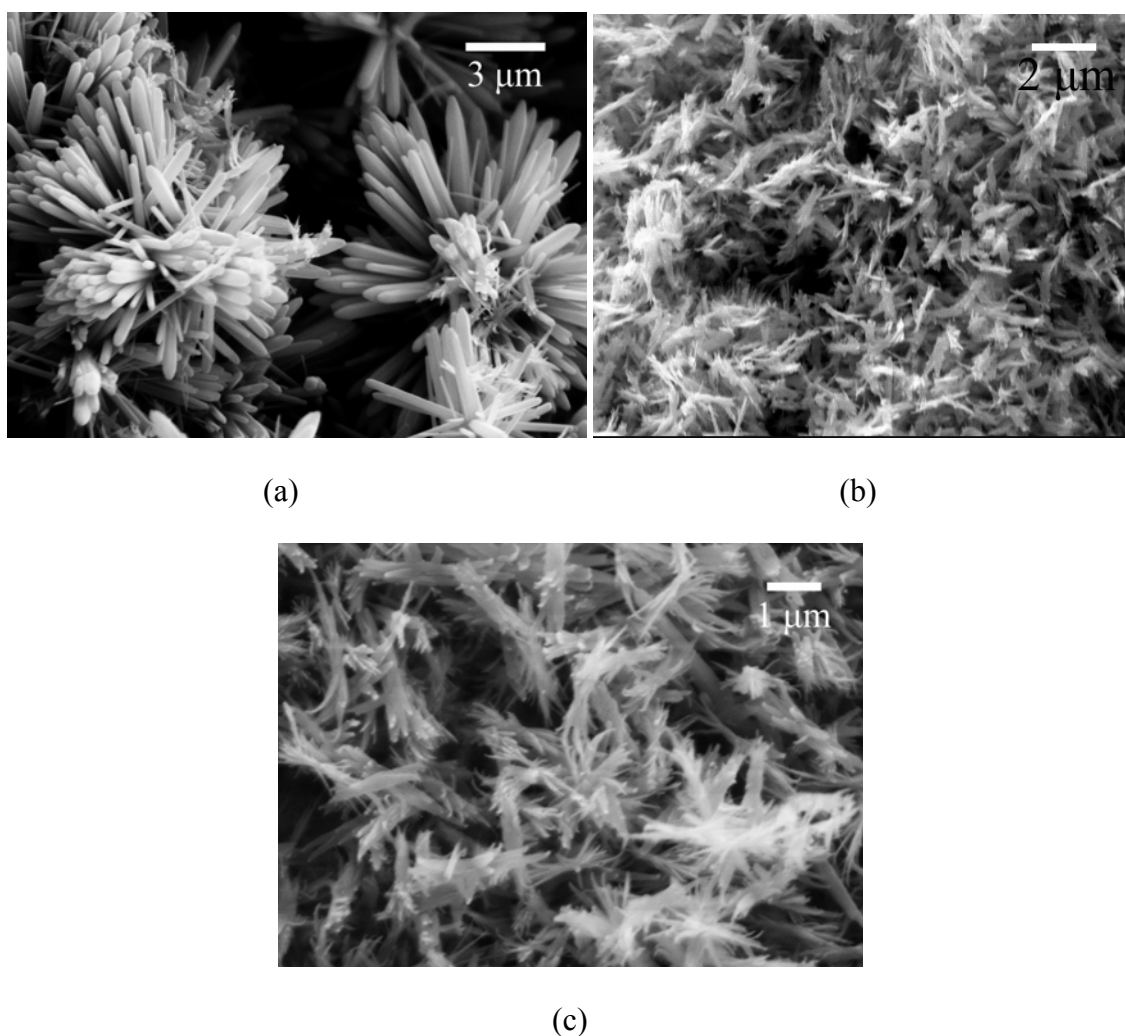
Fig. 8-6: SEM images of CuO/ZnO prepared in the presence of NaAOT with different Cu:Zn ratios: (a) Cu:Zn=3:7, (b) Cu:Zn=1:1, (c) Cu:Zn=7:3.

Cu-Zn bimetallic oxides were also prepared by heat-treatment at 90 °C of the hydroxide solutions in the presence of NaAOT. The Cu:Zn ratio can be changed in solution, by which oxides with controllable compositions can be easily prepared. The SEM images of the obtained CuO/ZnO samples with different Cu:Zn ratios are shown in Fig. 8-6. When the ratio was 3:7, flower-like ZnO rods dominated in the sample. CuO formed small rods on the ZnO crystals (Fig. 8-6 a). When the copper composition was increased to 50 mol% (Cu:Zn=1:1), the sample exhibited mixed morphologies consisting of flower-like ZnO and dispersed CuO rods (Fig. 8-6 b). With further increase of Cu:Zn ratio of 7:3, ZnO was dispersed by CuO and the flower-like structure of ZnO could not be observed anymore (Fig. 8-6 c).

XRD patterns of the CuO/ZnO samples with different Cu:Zn ratio are shown in Fig. 8-7. Copper and zinc oxide were detected in all the 3 samples. The change of the Cu:Zn ratio is reflected by the variation of intensities in the spectra of the two oxides. With the increase of the amount of ZnO, the ZnO contributions become stronger, corresponding to the decrease of the intensities of the CuO peaks.
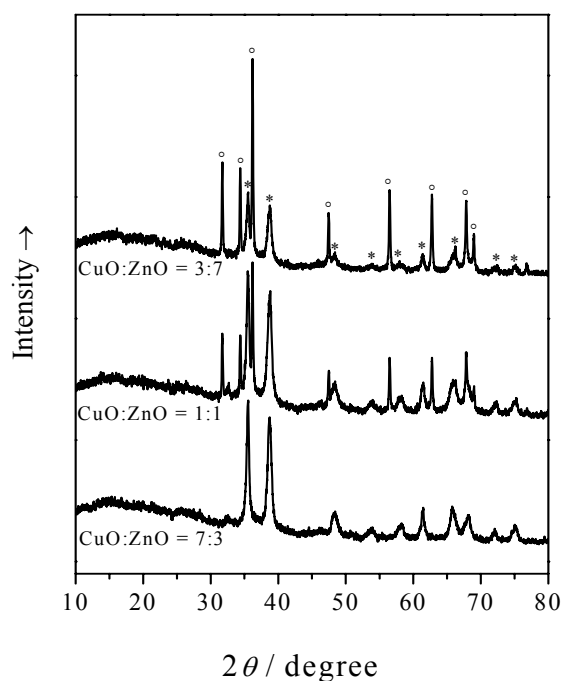
Fig. 8-7: XRD patterns of CuO/ZnO with different Cu:Zn ratios prepared in the presence of NaAOT. The marked peaks correspond to ZnO (o) and CuO (*), respectively.

(a)   (b)
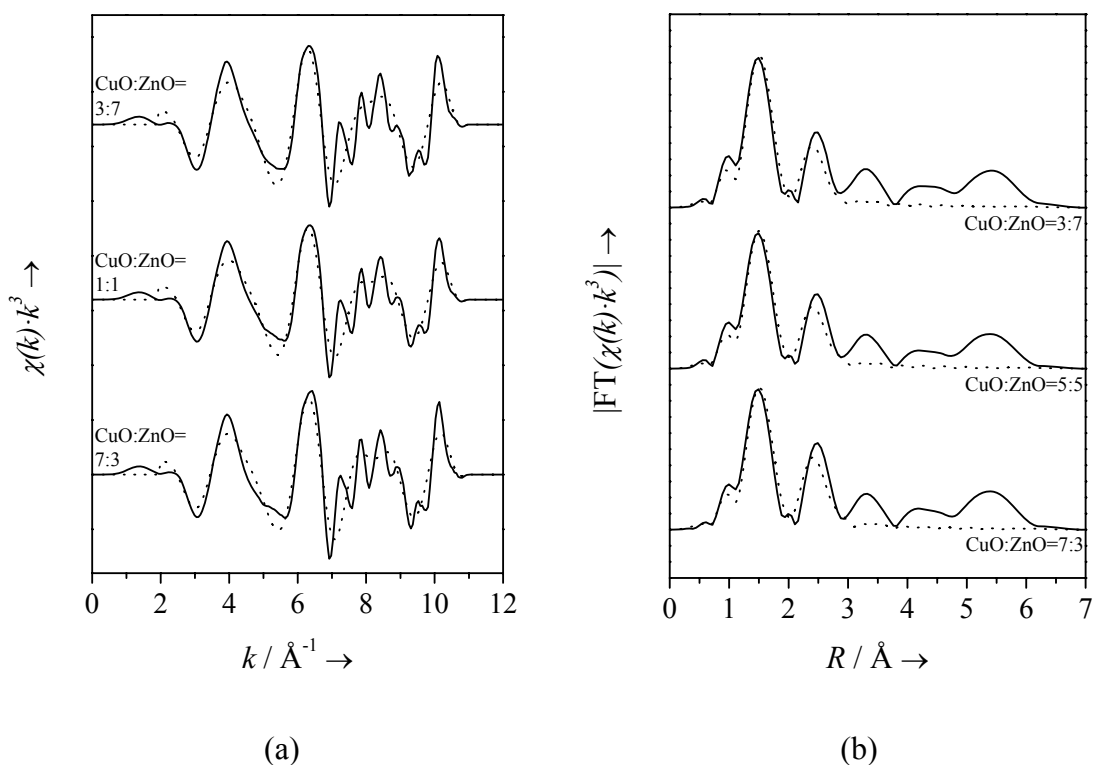
Fig. 8-8: Cu K-edge EXAFS raw data (a) and Fourier transform magnitudes (b) of CuO/ZnO with different Cu:Zn molar ratios prepared in the presence of NaAOT. Solid line: experimental data, dotted line: fit data.

Table 8-1: Fit parameters for the Cu K-edge EXAFS spectra of CuO/ZnO with different Cu:Zn molar ratios.

CuO/ZnO	Cu – 4 O			Cu – 8 Cu		
Cu:Zn	R / Å	N	$\sigma^2 \cdot 10^3$ / Å^2	R / Å	N	$\sigma^2 \cdot 10^3$ / Å^2
3:7	1.96	3.6	1.0	2.91	7.8	18.8
1:1	1.96	3.3	1.0	2.91	7.3	18.1
7:3	1.96	3.3	0.7	2.90	7.6	16.7

EXAFS analysis was performed to investigate the crystal structure of CuO in the oxide mixtures (CuO/ZnO). In the Cu K-edge raw data and FTs of the CuO/ZnO mixture (Fig. 8-8, part a-b), the shells of Cu–O and Cu–Cu in CuO are clearly present. Table 8-1 shows the fit parameters for the Cu K-edge EXAFS spectra. The Cu–O distances of the first shell are at 1.96 Å, which fit well to that of the bulk copper oxide. The second Cu–Cu shells are at the

distance of 2.90-2.91 Å and with the coordination number of 7.3-7.8, which are also in agreement with the crystallographic values of copper oxide [122].

The short-range structure of ZnO in the mixed oxides (CuO/ZnO) was also determined by X-ray absorption spectroscopy (EXAFS, Fig. 8-9 and Table 8-2). In the Zn K-edge raw data and FTs of the CuO/ZnO mixture, the shells of Zn–O and Zn–Zn in ZnO are clearly present. Table 8-2 shows the fit parameters for the Zn K-edge EXAFS spectra. The Zn–O distances of the first shell are at 1.96 Å. The coordination numbers are about 4. The results agree well with those of crystalline zinc oxide. The second Zn–Zn shell is in a distance of 3.23 Å with coordination numbers of around 12, which are also in agreement with the crystallographic values of zinc oxide [159].

(a)   (b)
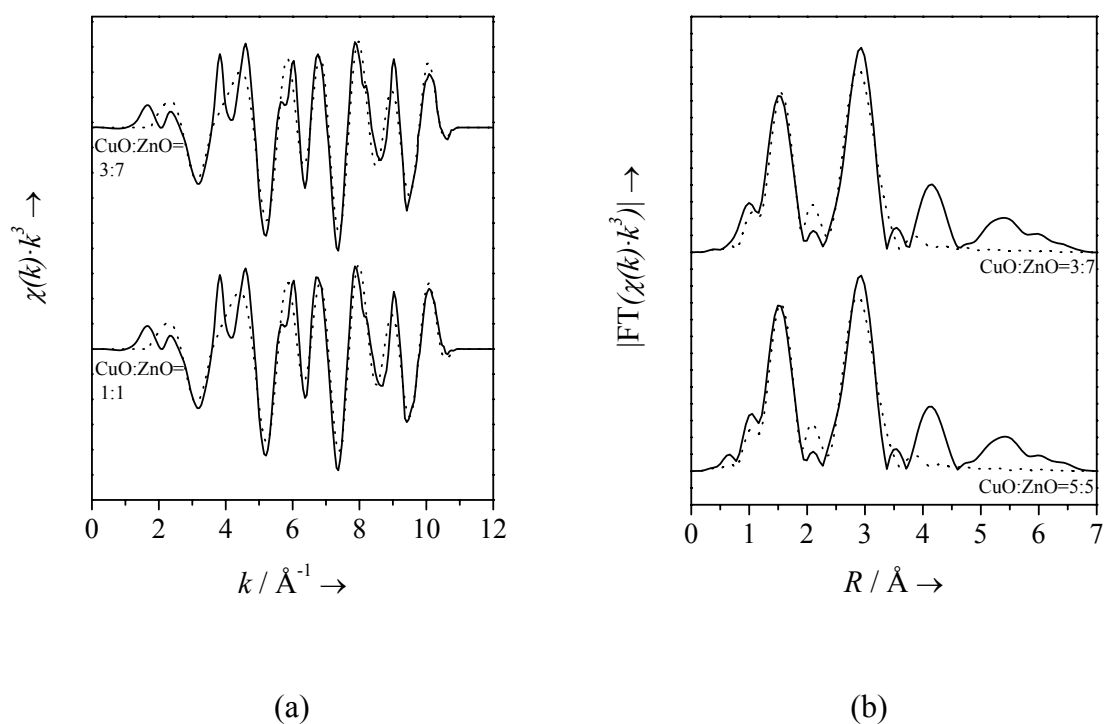
Fig. 8-9: Zn K-edge EXAFS raw data (a) and Fourier transform magnitudes (b) of CuO/ZnO with different Cu:Zn molar ratios prepared in the presence of NaAOT. Solid line: experimental data, dotted line: fit data.

Table 8-2: Fit parameters for the Zn K-edge EXAFS spectra of CuO/ZnO with different Cu:Zn molar ratios.

CuO/ZnO	Zn – 4 O			Zn – 12 Zn		
Cu:Zn	R / Å	N	$\sigma^2 \cdot 10^3$/ Å^2	R / Å	N	$\sigma^2 \cdot 10^3$/ Å^2
3:7	1.96	4.0	5.28	3.23	12.5	13.0
1:1	1.96	4.3	5.50	3.23	12.3	12.9

8.4 Conclusions

In summary, copper(II) oxide, zinc oxide and copper-zinc mixed oxides were prepared by heat-treatment of the respective metal hydrate aqueous solutions at low temperature. The preparation conditions, such as the addition of NaAOT or the nature of the solvents (aqueous or organic), have a significant effect on the morphology of the products. CuO leaflets, platelets and spherical particles were obtained in the synthesis without NaAOT in water, with NaAOT in water, and with NaAOT in mixture of water and butanol, respectively. Flower-like ZnO structures consisting of ZnO rods with different shapes and sizes were formed in the preparation of mixed oxides with the presence of NaAOT in water or in a mixture of water and butanol. The ratio of Cu:Zn in the mixed oxides can be easily tuned in the synthesis.

9 Methods

9.1 Electron microscopy

Electron microscopy is a fairly straightforward technique to determine the morphology and structure of samples. It can also reveal information on the composition and internal structure of the particles, for example by detecting the characteristic X-rays that are produced by the interaction of electrons with matter, or by analyzing how the electrons are diffracted [185, 186].

Accelerated electrons have characteristic wavelengths of less than 1 Å. Fig. 9-1 summarizes what happens to the electrons when the primary beam of energy between 100 and 400 keV hits the sample:

- Depending on sample thickness, a fraction of the electrons passes through the sample without suffering energy loss. As the attenuation of the beam depends on density and thickness, the transmitted electrons form a two-dimensional projection of the sample.

- Electrons are diffracted by particles if they are favorably oriented towards the beam, enabling one to obtain dark field images as well as crystallographic information.

- Electrons can collide with atoms in the sample and back scattered; backscattering is more effective when the mass of the atom increases. If a region of the sample contains heavier atoms (*e.g.* Pt) than those of its surroundings, it can be distinguished because of a higher yield of backscattered electrons.

- Auger electrons and X-rays are formed in the relaxation of core-ionized atoms.

- Electrons excite characteristic vibrations in the sample, and these can be studied by analyzing the energy loss suffered by the primary electrons.

- Many electrons lose energy in a cascade of consecutive inelastic collisions. Most of the secondary electrons emitted by the sample have their last loss process in the surface region.

- The emission of a range of photons from UV to infrared, called cathodoluminescence, is mainly caused by recombination of electron-hole pairs in the sample.
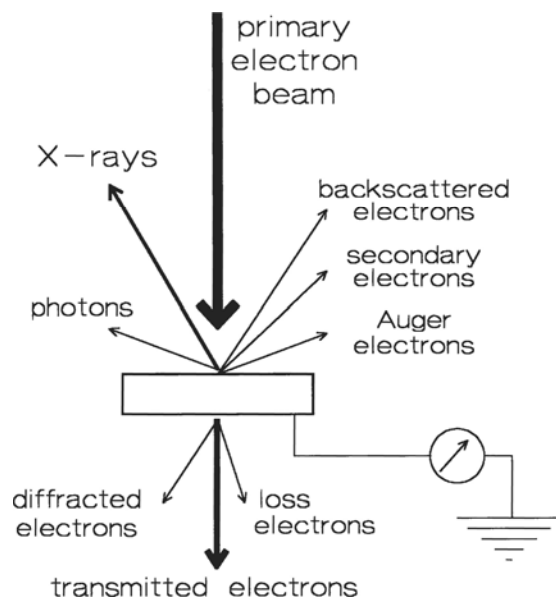
Fig. 9-1: The interaction between the primary electron beam and the sample in an electron microscope leads to a number of detectable signals [187].

Thus, the interaction of the primary beam with the sample provides a wealth of information on morphology, crystallography and chemical composition.

Three types of electron microscopes are shown schematically in Fig. 9-2. Transmission electron microscopy (TEM) uses transmitted and diffracted electrons. A TEM instrument is in a sense similar to an optical microscope if one replaces optical by electromagnetic lenses. In TEM, a primary electron beam of high energy and high intensity passes through a condenser to produce parallel rays, which impinge on the sample. As the attenuation of the beam depends on the density and the thickness, the transmitted electrons form a two-dimensional projection of the sample mass, which is subsequently magnified by the electron optics to produce a so-called bright field image. The dark field image is obtained from the diffracted electron beams, which are slightly off angle from the transmitted beam. Typical operating conditions of a TEM instrument are 100-200 keV electrons, 10^{-6} mbar vacuum, 0.5 nm resolutions and a magnification of $3 \cdot 10^5$ to 10^6.

Scanning electron microscopy (SEM) is carried out by scanning a narrow electron beam over the sample surface and detecting the yield of either secondary or backscattered electrons as a function of the position of the primary beam. Contrast is caused by the orientation, parts of the surface facing the detector appearing brighter than parts of the surface with their surface normal pointing away from the detector. The secondary electrons have mostly low energies

(in the approximate range 5-50 eV) and originate from the surface region of the sample. Backscattered electrons come from deeper regions and carry information on the composition of the sample, because heavy elements are more efficient scatterers and appear brighter in the image.
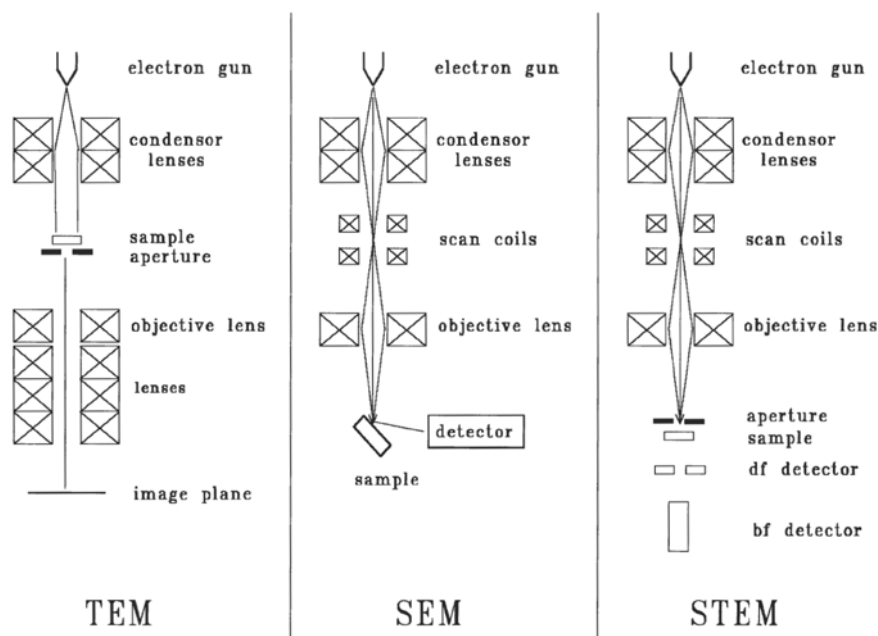
Fig. 9-2: Schematic setup of an electron microscope in the transmission (TEM), scanning (SEM), and combined (STEM) mode [188].

Dedicated SEM instruments have resolutions of about 2-3 nm. Simple versions of SEM with micron resolution are often available on Auger electron spectrometers, for the purpose of sample positioning. The main difference between SEM and TEM is that the SEM sees contrast due to the topology and composition of a surface, whereas the electron beam in TEM projects all information on the mass it encounters in a two-dimensional image, which, however, is of subnanometer resolution.

9.2 X-ray diffraction

X-rays have wavelengths in the angstrom range, are sufficiently energetic to penetrate solids, and are well suited to probe their internal structure. XRD is used to identify bulk phases, to monitor the kinetics of bulk transformations, and to estimate particle sizes. An attractive feature is that the technique can be applied in situ. The theory of X-ray diffraction is given in textbooks of solid state physics [189, 190] and in specialized books [191, 192].

A conventional X-ray source consists of a target that is bombarded with high-energy electrons. The emitted X-rays arise from two processes. Electrons slowed down by the target emit a continuous background spectrum of bremsstrahlung. Superimposed on this are characteristic, narrow lines. The Cu K_α line, with an energy of 8.04 keV and a wavelength of 0.154 nm, arises because a primary electron under emission of an X-ray quantum. K_β radiation is emitted when the K-hole is filled from the M-shell, and so on.
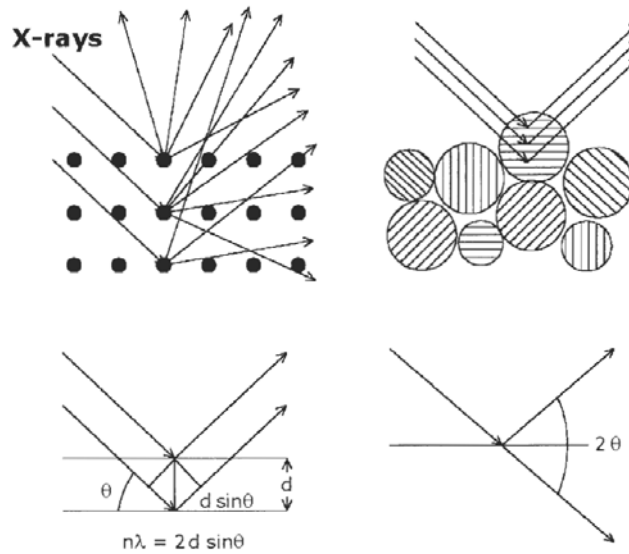
Fig. 9-3: X-rays scattered by atoms in an ordered lattice interfere constructively in directions given by Bragg's law. The angles of maximum intensity enable one to calculate the spacings between the lattice planes and furthermore allow for phase identification. Diffractograms are measured as a function of the angle 2θ. When the sample is a polycrystalline powder, the diffraction pattern is formed by a small fraction of the particles only. Rotation of the sample during measurement increases the number of particles that contribute to diffraction [187].

X-ray diffraction is the elastic scattering of X-ray photons by atoms in a periodic lattice. The scattered monochromatic X-rays that are in phase give constructive interference. Fig. 9-3 illustrates how the diffraction of X-rays by crystal planes allows one to derive lattice spacings by using the Bragg relation:

$n \lambda = 2d \sin\theta; n = 1,2, ...$

where

λ is the wavelength of the X-rays

d   is the distance between two lattice planes

θ   is the angle between the incoming X-rays and the normal to the reflecting lattice plane

n   is an integer called the order of the reflection.

If one measures the angles under which constructively interfering X-rays leave the crystal, the Bragg relation gives the corresponding lattice spacings, which are characteristic of a given compound.

The XRD pattern of a powdered sample is measured with a stationary X-ray source (usually Cu K$_\alpha$) and a movable detector, which scans the intensity of the diffracted radiation as a function of the angle 2θ between the incoming and the diffracted beams. When working with powdered samples, an image of diffraction lines occurs because a small fraction of the powder particles will be oriented such that by chance a certain crystal plane is at the right angle θ with the incident beam for constructive interference (see Fig. 9-3).

X-ray diffraction has an important limitation: clear diffraction peaks are only observed when the sample possesses sufficient long-range order. The advantage of this limitation is that the width (or rather the shape) of diffraction peaks carries information on the dimensions of the reflecting planes. Diffraction lines from perfect crystals are very narrow. For crystallite sizes below 100 nm, however, line broadening occurs due to incomplete destructive interference in scattering directions where the X-rays are out of phase.

9.3 Extended X-ray absorption fine structure (EXAFS)

EXAFS is an X-ray absorption technique that gives detailed local structure information [193]. The technique is based on the absorption of X-rays and the creation of photoelectrons, which are scattered by nearby atoms in a lattice. Interference effects are visible in the X-ray absorption spectrum and give detailed information on the distance, number and type of neighbors of the absorbing atom. The phenomenon has been known since the 1920s [194], but has had to wait before it could be exploited as an analytical tool until the bright, tuneable sources of X-rays at synchrotrons became available in the 1970s. Laboratory systems have been built [193], and although these spectrometers can be quite successful for applications in the low energy range, they have in general been abandoned in favor of synchrotrons. Important

for the progress of EXAFS were the theoretical developments by Sayers et al. [195], who showed how local structure information is extracted from EXAFS measurements.

At the time when EXAFS was introduced in catalysis, around 1975, the technique was considered to be one of the most promising tools for investigating catalysts. These high expectations have not quite been fulfilled, mainly because data analysis in EXAFS is highly complicated and, unfortunately, not always possible without ambiguity. A number of successful applications, however, have proven that EXAFS applied with care on optimized catalysts can be a very powerful tool in catalysis [196].

Fig. 9-4 illustrates the EXAFS phenomenon. First we consider the X-ray absorption spectrum of a free atom, which has an electron with binding energy E_b. If we irradiate this atom with X-rays of energy hv, absorption takes place when h$v \geq E_b$ and the electron leaves the atom with a kinetic energy E_k = hv-E_b. The X-ray absorption spectrum shows a series of edges corresponding to the binding energies of all electrons present in the atom, but contains no further structure.

Fine structure arises if neighbors surround the atom. In this case the photoelectron, which has both particle and wave character, can be scattered back from a neighboring atom (see Fig. 9-4). Because of its wave character, the outgoing and the backscattered electrons interfere. Depending on the wavelength of the electron, the distance between emitting and scattering atom, and the phase shift caused by the scattering event, the two waves enhance or destroy each other. As a result, the cross section for X-ray absorption is modulated by the interference between the photoelectron waves, such that it is enhanced at energies where constructive interference occurs. As indicated schematically in Fig. 9-4, the X-ray absorption spectrum exhibits a fine structure which extends to several hundred eV above the absorption edge. The absorption around the edge arises from electrons with low kinetic energies, which interact with valence electrons. This part of the spectrum is often referred to as the NEXAFS or XANES [197].

The intensity of the wiggles increases if the number of neighbors increases, the number of oscillations depends inversely on interatomic distances (as in any scattering or diffraction experiment), and the step height of the edge is proportional to the concentration of atoms in the sample.
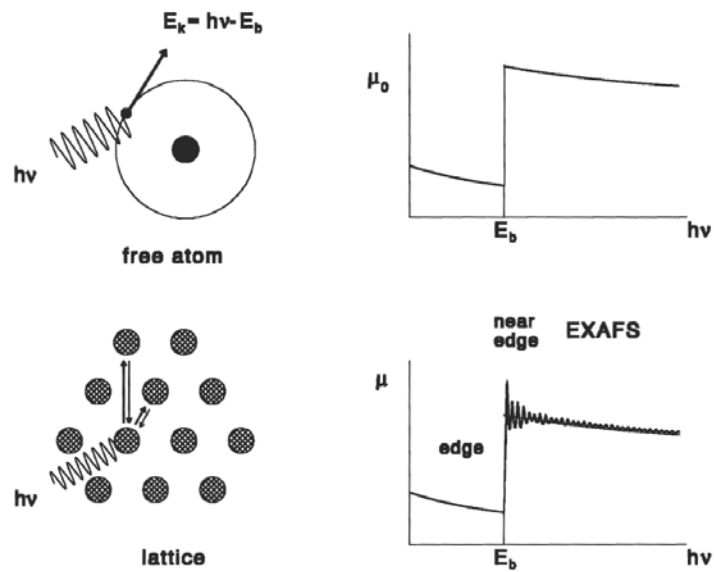
Fig. 9-4: Absorption of X-rays as a function of photon energy E=hv by a free atom and by atoms in a lattice. The fine structure represents the EXAFS function [187].

The EXAFS function, $\chi(k)$, is extracted from the X-ray absorption spectrum in Fig. 9-4 by removing first the approximately parabolic background and the step, i.e. the spectrum of the free atom in Fig. 9-4. As in any scattering experiment, it is customary to express the signal as a function of the wave number, k, rather that of energy. The relationship between k and the kinetic energy of the photoelectron is

$$k = \frac{2\pi}{h}\sqrt{2m_e E_{kin}} = \frac{2\pi}{h}\sqrt{2m_e(hv - E_b)}$$

where

k is the wave number of the photoelectron

h   is Planck's constant

m_e is the mass of an electron

E_{kin} is the kinetic energy of the photoelectron

v is the X-ray frequency

E_b is the binding energy of the photoemitted electron.

$hk/2\pi$ is the momentum of a wave quantum, and $\sqrt{(2m_e E_{kin})} = m_e v$ is the classical momentum of the electron when considered as a particle.

It is impossible to explain EXAFS properly without theoretical formulae. In a monoatomic solid, the EXAFS function $\chi(k)$ is the sum of the scattering contributions of all atoms in neighboring coordination shells:

$$\chi(k) = \sum_j A_j(k)\sin\left(2kr_j + \phi_j(k)\right)$$

in which

$\chi(k)$ is the EXAFS function, with the wave number as argument

j is the label of the coordination shells around the electron-emitting atom

$A_j(k)$ is the amplitude, the scattering intensity due to the jth coordination shell

r_j is the distance between the central atom and atoms in the jth shell

$\phi(k)$ is the total phase shift, equal to the phase shift of the backscattering atom plus twice that of the absorbing atom.

Thus, each coordination shell contributes a sine function multiplied by amplitude. EXAFS analysis boils down to recognizing all sine contributions in $\chi(k)$. The obvious mathematical tool to achieve this is Fourier analysis.

The argument of each sine contribution depends on k, which is known, r, which is to be determined, and the phase shift $\phi(k)$. The latter needs to be known before r can be determined. The phase shift is a characteristic property of the scattering atom in a certain environment, and is best derived from the EXAFS spectrum of a reference compound, for which all distances are known.

The amplitude $A_j(k)$ of each scattering contribution contains the number of neighbors in a coordination shell as the most desirable information:

$$A_j(k) = N_j \frac{e^{-2r_j / \lambda(k)}}{k r_j^2} S_0^2(k) F_j(k) e^{-2k^2 \sigma_j^2}$$

where

N_j is the coordination number of atoms in the jth shell

S_0 is the correction for relaxation effects in the emitting atom

F_{j},   is the backscattering factor of atoms in the jth shell

λ is the inelastic mean free path of the electron

σ^2 is the mean-squared displacement of atoms in the sample.

The contributions to $A_j(k)$ are discussed below.

N_j is the coordination number, equal to the number of neighbors in the jth coordination shell. For an fcc metal such as rhodium we expect 12 neighbors in the first shell. If a particle becomes small, the average coordination number decreases. Note that unless the sample is that of a single element, N is a fractional coordination number, *i.e.* the product of the real coordination number and the concentration of the element involved.

The second term expresses that nearest and next nearest neighbors dominate scattering contributions to the EXAFS signal, while contributions from distant shells are weak. The dependence of the amplitude on $1/r^2$ reflects that the outgoing electron is a spherical wave, the intensity of which decreases with the distance squared. The term $\exp(-2r/\lambda)$ represents the exponential attenuation of the electron when it travels through the solid. The factor 2 is there because the electron has to make a round trip between the emitting and the scattering atom in order to cause interference.

The term $S_0^2(k)$ is a correction for relaxation or final state effects in the emitting atom, such as the shake-up, shake-off and plasmon excitations. The result of these processes is that some absorbed X-ray quanta of energy hν are converted not into photoelectrons with the kinetic energy hν-E_b, but into electrons with a lower kinetic energy as well.

The backscattering factor $F_j(k)$ represents the scattering performance of the jth neighbor. The term $\exp(-2k^2\sigma^2)$ accounts for the disorder of the solid. Static disorder arises if atoms of the same coordination shell have slightly different distances to the central atom. Amorphous solids, for instance, possess large static disorder. Dynamic disorder, on the other hand, is caused by lattice vibrations of the atoms. Dynamic disorder becomes much less important at lower temperatures, and it is therefore an important advantage to measure spectra at cryogenic temperatures, especially if a sample consists of highly dispersed particles.

The EXAFS function becomes understandable if we look at the Fourier transform of $\chi(k)$, which resembles a radial distribution function:

$$\theta(r) = \frac{1}{\sqrt{2\pi}} \int_{k_{min}}^{k_{max}} k^n \lambda(k) e^{2ikr}\, \mathrm{d}k$$

in which

$\theta_n(r)$ is the Fourier Transform of the EXAFS signal

n is an integer, usually chosen as 1, 2, or 3.

The function $\theta_n(r)$ represents the probability of finding an atom at a distance r, modified by the two r-dependent terms in the amplitude, which progressively decrease the intensity of distant shells. The transform is often weighted with either k or k^3 to emphasize the role of light or heavy atoms, respectively. Vaarkamp, however, has argued that there is little mathematical justification for doing so, and advocates the use of weight factors based on the statistical errors in the EXAFS data [198]. In principle, the Fourier transform becomes more accurate when the k-interval is larger, but in practice the signal-to-noise ratio of the spectrum sets the limit for k.

A straightforward Fourier transform of the EXAFS signal does not yield the true radial distribution function. First, the phase shift causes each coordination shell to peak at the incorrect distance; second, due to the element-specific backscattering amplitude, the intensity may not be correct. The appropriate corrections can be made, however, when phase shift and amplitude functions are derived from reference samples or from theoretical calculations. The phase- and amplitude-corrected Fourier transform becomes:

$$\theta_n(r) = \frac{1}{\sqrt{2\pi}} \int\limits_{k_{min}}^{k_{max}} k^n \chi(k) \frac{e^{-i\phi(k)}}{F_j(k)} e^{2ikr} dk$$

with all symbols as defined above.

Fourier transforms usually show intensity at distances that are too small to correspond to neighbor atoms. Although artefacts induced by the limited k-range over which the Fourier transform has been taken may occur, part of the intensity at low values of r is due to scattering of the electrons inside the atom from which they originate.

The main steps for the analysis of an EXAFS spectrum are:

- Extract the EXAFS function $\chi(k)$ from measured data.

- Select a k-interval and compute the k or k^3 weighted Fourier transform.

- Identify individual contributions to the Fourier transform and use these to construct a set of parameters that gives acceptable fits to the spectrum $\chi(k)$, the magnitude and the imaginary part of the Fourier transforms.

In order to do this, one needs phases and backscattering amplitudes, preferably from spectra of reference compounds, although calculated data are used as well.

9.4 Infrared spectroscopy
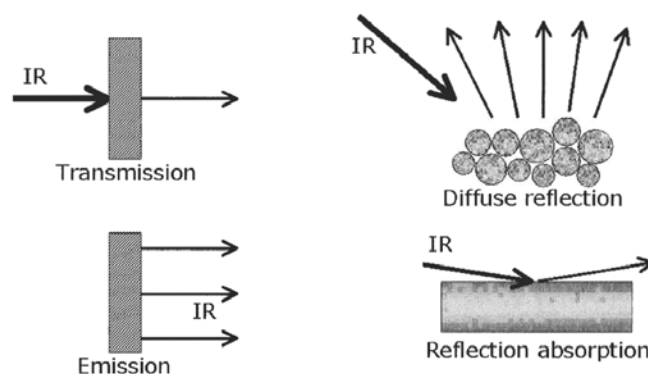
Fig. 9-5: different ways to perform infrared spectroscopy [187].

Several forms of infrared spectroscopy are in use, as illustrated in Fig. 9-5. The most common form of the technique is transmission infrared spectroscopy. In this case the sample consists typically of 10-100 mg of samples, pressed into a self-supporting disk of approximately 1 cm^2 and a few tenths of a millimetre in thickness. Transmission IR can be applied if the bulk of the sample absorbs weakly.

In the diffuse reflectance mode, samples can be measured as loose powders, with the advantages that not only is the tedious preparation of wafers unnecessary but also diffusion limitations associated with tightly pressed samples are avoided. Diffuse reflectance is also the indicated technique for strongly scattering or absorbing particles. The often-used acronyms DRIFT or DRIFTS stand for diffuse reflectance infrared Fourier transform spectroscopy. The diffusely scattered radiation is collected by an ellipsoidal mirror and focussed on the detector. The infrared absorption spectrum is described the Kubelka-Munk function:

$$\frac{K}{S} = \frac{(1 - R_\infty)^2}{2R_\infty}$$

in which

K is the absorption coefficient, a function of the frequency v

S is the scattering coefficient

R_∞ is the reflectivity of a sample of infinite thickness, measured as a function of v.

If the scattering coefficient does not depend on the infrared frequency, the Kubelka-Munk function transforms the measured spectrum $R_\infty(v)$ into the absorption spectrum $K(v)$.

Fourier-transform infrared (FTIR) spectrometers operating on the principle of the Michelson interferometer are widely used today. These instruments have the great advantage that the entire spectrum is obtained for each scan the interferometer makes, with the result that the total collection time needed to measure a spectrum is much lower. The treatment of the Fourier transform technique can be found elsewhere [199, 200].

Optical components can be made of NaCl, transparent from 650 cm^{-1} to 4000 cm^{-1}, KBr, with a low energy cut-off of 400 cm^{-1}, or CsI, with an even more favourable cut-off of 200 cm^{-1}. The source is usually a temperature-stabilized ceramic filament operating around 1500 K.

9.5 Thermal analysis techniques

Thermogravimetry (TG)

In this technique, changes in the mass of a sample are studied while the sample is subjected to a controlled temperature programme. The temperature programme is most often a linear increase in temperature, but isothermal studies can also be carried out, when the changes in sample mass with time are followed [201, 202]. TG is inherently quantitative, and therefore an extremely powerful analytic technique, but gives no direct chemical information. The ability to analyse the volatile products during a weight change is of great value.

The essential components of the equipment used, called a thermobalance, are a recording balance, furnace, temperature programmer, sample holder, an enclosure for establishing the required atmosphere, and a means of recording and displaying the data.

Balance sensitivity is usually around one microgram, with a total capacity of a few hundred milligrams. A typical operating range for the furnace is ambient temperature to 1000°C, with heating rates up to 100 K min^{-1}. The quality of the furnace atmosphere deserves careful attention, particularly the ability to establish an inert (oxygen-free) atmosphere, and it is useful to be able to quickly change the nature of the atmosphere. Compatibility between the materials of construction and the sample and its decomposition products, and the gaseous atmosphere, must be considered. Sample holder materials commonly available include aluminum, platinum, silica, and alumina.

The measurement of the sample temperature occurs by a thermocouple close to the sample. Careful calibration for temperature is important, especially for kinetic studies. Various means are available for temperature calibration, which is not a trivial matter, although reproducibility is often more important than absolute accuracy. Weight calibration is readily achieved using standard compounds.

The ability of TG to generate fundamental quantitative data from almost any class of materials, has led to its widespread use in every field of science and technology. Key application areas are listed below:

- Thermal stability: related materials can be compared at elevated temperatures under the required atmosphere. The TG curve can help to elucidate decomposition mechanisms.

- Kinetic studies: a variety of methods exist for analysing the kinetic features of all types of weight loss or gain, either with a view to predictive studies, or to understanding the controlling chemistry.

- Material characterisation: TG and DTG curves can be used to "fingerprint" materials for identification or quality control.

- Corrosion studies: TG provides an excellent means of studying oxidation, or reaction with other reactive gases or vapours.

- Simulation of industrial processes: the thermobalance furnace may be thought of as a mini-reactor, with the ability to mimic the conditions in some types of industrial reactor.

- Compositional analysis: by careful choice of temperature programming and gaseous environment, many complex materials or mixtures may be analysed by selectively decomposing or removing their components. This approach is regularly used to analyse, e.g., the filler content in polymers; carbon black in oils; ash and carbon in coals, and the moisture content of many substances.

Differential Thermal Analysis (DTA)

DTA involves heating or cooling a test sample and an inert reference under identical conditions, while recording any temperature difference between the sample and reference. This differential temperature is then plotted against time, or against temperature. Changes in the sample which lead to the absorption or evolution of heat can be detected relative to the inert reference.

Differential temperatures can also arise between two inert samples when their response to the applied heat-treatment is not identical. DTA can therefore be used to study thermal properties and phase changes which do not lead to a change in enthalpy. The baseline of the DTA curve should then exhibit discontinuities at the transition temperatures and the slope of the curve at

any point will depend on the microstructural constitution at that temperature. The area under a DTA peak can be related to the enthalpy change and is not affected by the heat capacity of the sample.

DTA may be defined formally as a technique for recording the difference in temperature between a substance and a reference material against either time or temperature as the two specimens are subjected to identical temperature regimes in an environment heated or cooled at a controlled rate. The key features of a differential thermal analysis instrument are shown in Fig. 9-6:
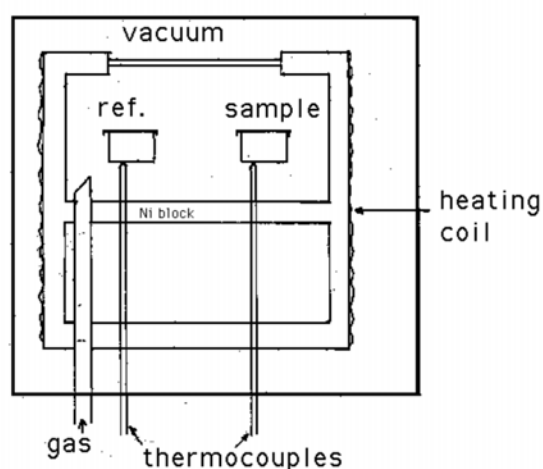
Fig. 9-6: Schematic illustration of a DTA cell [201].

9.5 Nitrogen adsorption measurement

Adsorption techniques are widely used for the characterization of the structure of porous materials. Due to its low cost and availability, nitrogen at its boiling point 77.35 K is typically used as the adsorbate. Nitrogen adsorption offers the possibility to determine the surface area and the pore size distribution in one step [203]. In order to explain the principles of this technique, some definitions have to be made. For convenience the pore sizes in porous materials are divided into micro-, meso- and macro-pores. This differentiation arises from the different behaviour of the respective pores in N_2 adsorption studies.

Considering the slit shaped pores in Fig. 9-7, the adsorption process starts in very small pores, the size of which is hardly larger than that of the adsorbed gas. This is due to the fact that in view of the proximity of neighboring pore walls, the adsorption potential in small pores is

strongly increased. Therefore the adsorption mechanism in micropores is usually considered as pore volume filling rather than adsorption [204]. This phenomenon is crucial for molecular sieve application of such adsorbants [205]. The smallest pore size that can be filled by nitrogen is determined by its kinetic diameter of 0.4 nm. The filling of small micropores (ultramicropores < l nm, Fig. 9-7 a) is known as primary micropore filling, whereas for larger micropores (supermicropores 1-2 nm, Fig. 9-7 b) the term secondary micropore filling is used [206]. Using a high-resolution adsorption apparatus, in the latter case a difference between monolayer adsorption (Fig. 9-7 b) and volume filling of supermicropores (Fig. 9-7 c) can be observed, which differentiates these pores from ultramicropores [207].
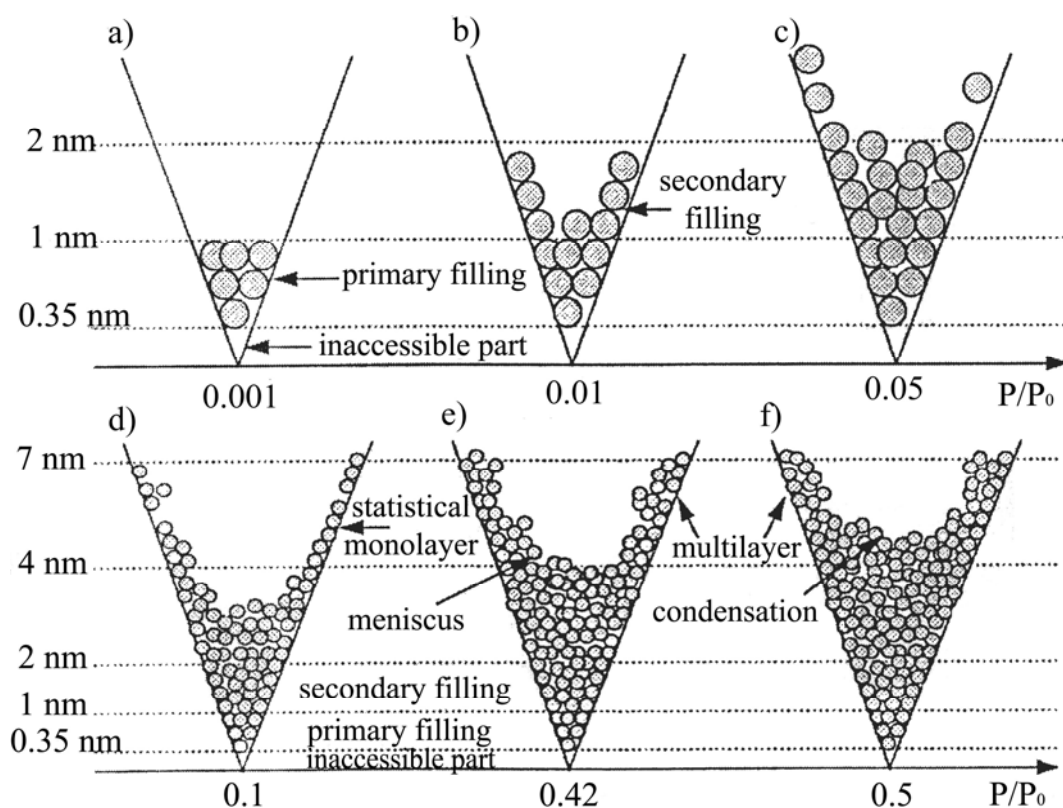
Fig. 9-7: Schematic drawing of the adsorption mechanism in micro- (a, b, c) and mesopores (d, e, f) [205].

Once the micropores are filled, the adsorption is characterized by adsorption on the mesor external surface of porous structure. In the first stages a preferential adsorption as a monolayer is observed (Fig. 9-7 d). From the monolayer capacity the surface area is derived. With increasing relative pressure the pore volume is gradually filled via successive build-up of multilayers without change in interaction potential between the layers. For relative

pressures $p/p_0 > 0.5$, the reduction of vapour pressure above concavely shaped surfaces (Fig. 9-7 e) leads to capillary condensation in mesopores.

By making use of adsorption models, surface areas and pore size distributions can be derived from the isotherm. One of the most frequently used models to determine the surface area of porous solids is the BET-model, established by Brunauer, Emmett and Teller [208]. Via transformation of the adsorption data (v_{ads} = moles adsorbed) in the BET-equation

$$\frac{p/p_0}{v_{ads} \cdot (1 - p/p_0)} = \frac{1}{v_{mono} \cdot C} + \frac{C-1}{v_{mono} \cdot C} \cdot p/p_0$$

for meso- or macroporous samples a linear dependence as a function of p/p_0 is observed for relative pressures between 0.05 and about 0.3. C is a characteristic variable describing the interaction of the respective adsorbent-adsorbate system. From the BET transformation plotted vs. p/p_0, the monolayer capacity v_{mono} is calculated from the linear region by 1/(slope + y-intercept). With

$$S_{BET} = v_{mono} \cdot \sigma \cdot N_A ,$$

where σ is the molecular cross sectional area for nitrogen (= 0.162 nm^2) and N_A is Avogadro's number, the BET-surface area is obtained. The model is based on the successive build-up of mono- and multilayers of adsorptive on the surface of the adsorbent and is strictly valid only for materials where the adsorption forces of neighboring walls do not overlap. The BET surface area thus cannot be regarded as a true measure for the internal surface area of ultramicroporous materials due to a significant distortion in the submonolayer region. However, if in the BET transformation of the isotherm linearity is obeyed in a reduced pressure range (usually at $p/p_0 < 0.15$), the derived value does give a useful measure of the extent of supermicropore area plus external surface area [209].

The special adsorption mechanism of microporous materials was first explained by Dubinin and Raduskevich [204]. They put forward an equation in terms of fractional micropore filling:

$$Ln(V_{ads}) = \ln(V_{mic}) - (\frac{RT}{E\beta})^2 \cdot (\ln(p_0/p))^2$$

where

V_{mic} is the micropore volume

E is the characteristic energy of adsorption (which is indirectly proportional to the micropore width)

P is a gas dependent affinity coefficient (0.33 for nitrogen).

Upon plotting the adsorption data according to eq. as a function of $(\ln(p_0/p))^2$, for microporous materials at low relative pressure (< 0.1) a straight line is obtained. The ordinate intercept gives the micropore volume and from the slope, the characteristic energy of adsorption E is derived. With the empirical relation

$$L_\mu \cdot (E - 11.4 \frac{kJ}{mol}) = 10.8 \frac{kJ}{mol} \cdot nm$$

the micropore width L_μ (in nm) can be calculated [210].

Deviation from the fit line in the DR-plot at low relative pressure is explained by activated diffusion in ultramicropores, deviation at high relative pressure is attributed to the presence of larger micropores. Sometimes in both representations two linear regions are seen, indicating a dual porosity distribution in the micropore region. Of course the reality in most adsorbents is somewhat more complicated. Instead of assuming a single pore size, a generalization of the model includes size distributions [211].
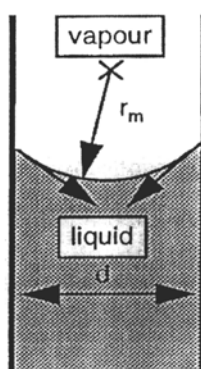
Fig. 9-8: Capillary model for the condensation in cylindrical mesopores [203].

In order to derive a pore size distribution for mesoporous materials, a capillary condensation model is frequently used. For this purpose, a liquid in a cylindrical pore with diameter d is

considered in equilibrium with its vapour. The curvature between the pore walls is concave and has a mean radius of curvature r_m (Fig. 9-8).

The capillary pressure exerted by the pore liquid on the walls is

$$\Delta p = 2\gamma/\Upsilon m = 2\gamma \cdot \cos\theta / d / 2$$

where

γ is the surface tension

θ is the wetting angle of the liquid.

At constant temperature and assuming an ideal gas behavior, the Kelvin equation is obtained for the vapour pressure p above a meniscus [203].

$$\mathrm{Ln}(p/p_0) = -\frac{2\gamma V_{ads}}{RT}\frac{1}{r_m}$$

V_{ads} is the molar volume of liquid adsorptive, which for the condensation in is assumed to be incompressible. From *eq.* it follows cylindrical mesopores that the pressure p over a concave meniscus is smaller than the saturation vapour pressure p_0. Condensation of a vapour in a pore with radius $d/2 = r_m \cdot \cos\theta$ thus occurs already at some pressure *p* below p_0. Each relative pressure is assigned to a specific pore radius. *Eq.* is applicable for pore radii between 1 nm and 25 nm. Based on the Kelvin equation, Barrett, Joyner and Halenda developed a method to derive the pore size distribution of mesoporous materials [212]. The pore size distribution from adsorption and desorption will generally result in different pore sizes, for instance due to the hindered outgassing of a pore with a small entrance. For aerogels a more realistic explanation for hysteresis is that condensation is governed by a cylindrical meniscus, whereas evaporation occurs from a hemispherical meniscus. Also Scherer argued that the pore size distribution from the desorption-branch better reflects the actual pore sizes in aerogels [213].

For more information on methods, please refer to references 187, 192, 193, 197, 203.

10 Summary

As a whole, the preparation of metals or mixed oxides is based on the thermolysis of solution-obtained precursors. Various routes and reaction conditions were explored, including the preparation of coordination polymers, sol-gel synthesis, and heat-treatment of metal salt solutions. The structure, morphology and properties of products were controlled by the variation of reaction conditions such as concentration, composition, residence time, additives, or thermolysis temperature.

Online analysis such as TG-IR or TG-MS was frequently employed to study the thermolysis of metal or intermetallic precursors. SEM, TEM, IR, XRD and EXAFS were used to elucidate the morphology and structure of the samples. Nitrogen physisorption and N_2O chemisorption were applied to investigate the specific surface area, the pore structure, and copper surface area. The Cu-based nanocomposites were used as catalysts for the synthesis of methanol.

The thermolysis of the coordination polymer $((CH_3)_3Sn)_4Ru(CN)_6$ was studied and Ru_3Sn_7 or $(Sn,Ru)O_2$ were prepared. Both compounds can be obtained in a nanocrystalline form if the reaction conditions are chosen properly. A batch-wise method and a continuous synthesis method were applied to the precipitation of the Cu–Zn coordination compound $Zn[Cu(CN)_3]$. With the continuous overflow precipitation method, fine spherical particles are obtained at high solution concentration and short residence time. The thermolysis of the cyanides led to Cu-Zn bimetallic oxides, which were reduced to Cu/ZnO and used as catalysts for methanol synthesis. The binuclear complex $[Zn(en)_3][Zn(CN)_4]$ and the mononuclear compound $Zn(CN)_2$ were prepared. Under oxygen, the thermolysis of both complexes led to ZnO nanoparticles with a size of 100–200 nm.

A sol-gel route was developed to prepare nanostructured porous ZnO/Al_2O_3. It was found that the nanostructure of the oxides can be fine-tuned by the Zn:Al ratio. ZnO can be dispersed in Al_2O_3 in atomic scale in a wide range of Zn concentrations. A high Al_2O_3 content led to amorphous ZnO with a high specific surface area. The obtained bimetallic oxides are very promising as supports for metal catalysts such as Cu for methanol synthesis. Propylene oxide was used as the gelation initiator for the sol-gel synthesis of CuO/Al_2O_3 and $CuO/ZnO/Al_2O_3$. The wet gel was dried in air as well as in supercritical carbon dioxide. Cu-Al and Cu-Zn-Al

mixed oxides were obtained after thermolysis at 400 °C. The oxides showed a porous structure and a high specific surface area.

In addition, copper oxide, zinc oxide and copper-zinc mixed oxides were prepared by heat-treatment of the corresponding metal hydrate solutions. The preparation conditions, such as the addition of NaAOT or the nature of the solvents (aqueous or organic), have a significant effect on the morphology of the products.

In summary, this work explored the synthesis of oxide nanocomposites for catalytic applications. The control of microstructures was the main focus. It was found that the microstructures could be controlled by composition, reaction (nucleation) rate, thermal treatment, drying and other parameters. Finally, the microstructures were correlated to specific applications such as catalysts for methanol synthesis.

References

1. J. Sato, N. Saito, H. Nishiyama and Y. Inoue. *J. Phys. Chem. B,* **2001**, *105*, 6061.

2. W. Cheng and H. H. Kung. *Methanol Production and Use*. New York, Marcel Dekker, **1994**.

3. Anonymous. *Miscellanea Berolinensia ad incrementum scientiarum (Berlin),* **1710**, *1*, 377.

4. H. J. Buser, A. Ludi, W. Petter and D. Schwarzenbach. *J. Chem. Soc. Chem. Commun.,* **1972**, 1299.

5. J. F. Keggin and F. D. Miles. *Nature,* **1936**, *137*, 577.

6. A. Ludi and H. U. Güdel. *Struct. Bonding,* **1973**, *14*, 1.

7. M. Verdaguer, A. Bleuzen, V. Marvaud, J. Vaissermann, M. Seuleiman, C. Desplanches, A. Scuiller, C. Train, R. Garde, G. Gelly, C. Lomenech, I. Rosenman, P. Veillet, C. Cartier and F. Villain. *Coord. Chem. Rev.,* **1999**, *192*, 1023.

8. R. Maisel. *Principles of Adsorption and Reaction on Solid Surfaces*. New York, Wiley, **1996**.

9. R. Schlögl, A. Knop-Gericke, M. Hävecker, U. Wild, D. Frickel, T. Ressler, R. E. Jentoft, J. Wienold, G. Mestl, A. Blume, O. Timpe and Y. Uchida. *Top. Catal.,* **2001**, *15*, 219.

10. M. L. Toebes, J. A. van Dillen and K. P. de Jong. *J. Mol. Catal. A: Chem.,* **2001**, *173*, 75.

11. D. J. Darensbourg, M. J. Adams, J. C. Yarbrough and A. L. Phelps. *Inorg. Chem.,* **2003**, *42*, 7809.

12. J. van der Loosdrecht, A. J. van Dillen, A. A. van der Horst, A. M. van der Kraan and J. W. Geus. *Top. Catal.,* **1995**, *2*, 29.

13. W. Teunissen, A. A. Bol and J. W. Geus. *Catal. Today,* **1999**, *48*, 329.

14. E. Boellaard, A. M. van der Kraan and J. W. Geus. Preparation of Supported Mono- and Bimetallic Catalysts by Deposition-Precipitation of Metal Cyanide Complexes. In: G. e. a. Poncelet, ed. *Preparation of Catalysts VI*, Elsevier, **1995**.

15. E. Boellaard, A. M. van der Kraan, A. B. P. Sommen, J. H. B. J. Hoebink, G. B. Marin and J. W. Geus. *Appl. Catal. A,* **1999**, *179*, 175.

16. K. L. Ng, J. Ding, L. Wang, L. M. Gan and C. H. Quek. *J. Phys. Chem. A,* **2000**, *104*, 8814.

17. X. Liu, G. Lu, Z. Yan and J. Beltramini. *Ind. Eng. Chem. Res.,* **2003**, *42*, 6518.

18. K. L. Ng, D. Chadwick and B. A. Toseland. *Chem.Eng. Sci.,* **1999**, *54*, 3587.

19. V. M. Palekar, H. Jung, J. W. Tierney and I. Wender. *Appl. Catal., A,* **1993**, *102*, 13.

20. R. J. Gormley, V. U. S. Rao, Y. Soong and E. Micheli. *Appl. Catal.,* **1992**, *87*, 81.

21. K. Klier. *Adv. Catal.,* **1982**, *31*, 243.

22. G. C. Chinchen, K. C. Waugh and D. A. Whan. *Appl. Catal. A,* **1986**, *25*, 101.

23. G. C. Chinchen, P. J. Denny, D. G. Parker, M. S. Spencer and D. A. Whan. *Appl. Catal. A,* **1986**, *30*, 333.

24. S. A. French, A. A. Sokol, S. T. Bromley, C. R. A. Catlow and P. Sherwood. *Topics in Catalysis,* **2003**, *24*, 161.

25. S. A. French, A. A. Sokol, S. T. Bromley, C. R. A. Catlow, S. C. Rogers, F. King and P. Sherwood. *Angew. Chem.,* **2001**, *113*, 4569.

26. Y. L. Zhang, Q. Sun, J. F. Deng, D. Wu and S. Y. Chen. *Appl. Catal. A,* **1997**, *158*, 105.

27. M. Kurtz, J. Strunk, O. Hinrichsen, M. Muhler, K. Fink, B. Meyer and C. Wöll. *Angew. Chem. Int. Ed.,* **2005**, *44*, 2790.

28. M. E. Fakley, J. R. Jennings and M. S. Spencer. *J. Catal.,* **1989**, *118*, 483.

29. R. G. Herman, K. Klier, G. W. Simmons, B. P. Finn and J. B. Bulko. *J. Catal.,* **1979**, *56*, 407.

30. I. A. Fisher and A. T. Bell. *J. Catal.,* **1998**, *178*, 153.

31. N. Tsubaki, M. Ito and K. Fujimoto. *J. Catal.,* **2001**, *197*, 224.

32. R. Yang, Y. Fu, Y. Zhang and N. Tsubaki. *J. Catal.,* **2004**, *228*, 23.

33. J. B. Hansen. *Handbook of Heterogeneous Catalysis*, vol. 3. Weinheim, VCH, **1997**.

34. M. Bowker, R. A. Hadden, H. Houghton, J. N. K. Hyland and K. C. Waugh. *J. Catal.,* **1988**, *109*, 263.

35. J. L. Li and T. Inui. *Appl. Catal., A,* **1996**, *137*, 105.

36. J. L. Li and T. Inui. *Appl. Catal., A,* **1996**, *139*, 87.

37. J. G. Wu, S. C. Luo, J. Toyir, M. Saito, M. Takeuchi and T. Watanabe. *Catal. Today,* **1998**, *45*, 215.

38. M. M. Günter, T. Ressler, B. Bems, C. Büscher, T. Genger, O. Hinrichsen, M. Muhler and R. Schlögl. *Catal. Lett.,* **2001**, *71*, 37.

39. D. Fang, Z. Liu, Y. Yang, H. Zhang and J. LIn. *Shiyou Huagong (Chinese Version),* **2005**, *34*, 1032.

40. T. Ressler, B. L. Kniep, I. Kasatkin and R. Schlögl. *Angew. Chem. Int. Ed.,* **2005**, *44*, 4704.

41. B. Bems, M. Schur, A. Dassenoy, H. Junkes, D. Herein and R. Schlögl. *Chem. Eur. J.,* **2003**, *9*, 2039.

42. W. S. Ning, H. Y. Shen and H. H. Liu. *Appl. Catal., A,* **2001**, *211*, 153.

43. S. Vukojevic, O. Trapp, J. D. Grunwaldt, C. Kiener and F. Schüth. *Angew. Chem. Int. Ed.,* **2005**, *44*, 7978.

44. R. Becker, H. Parala, F. Hilpler, O. Tkachenko, K. Klementiev, W. Grünert, H. Wilmer, O. Hinrichsen, M. Muhler, A. Birkner, C. Wöll, S. Schäfer and R. A. Fischer. *Angew. Chem. Int. Ed.,* **2004**, *43*, 2839.

45. M. Kurtz, N. Bauer, C. Büscher, H. Wilmer, O. Hinrichsen, R. Becker, S. Rabe, K. Merz, M. Driess, R. A. Fischer and M. Muhler. *Catal. Lett.,* **2004**, *92*, 49.

46. R. Burch, S. E. Golunski and M. S. Spencer. *J. Chem. Soc., Faraday Trans.,* **1990**, *86*, 2683.

47. M. S. Spencer. *Catal. Lett.,* **1998**, *50*, 37.

48. C. V. Ovesen, B. S. Clausen, J. Schiotz, P. Stoltze, H. Topsoe and J. K. Norskov. *J. Catal.,* **1997**, *168*, 133.

49. N. Y. Topsoe and H. Topsoe. *J. Mol. Catal.,* **1999**, *141*, 95.

50. I. Nakamura, T. Fujitani, T. Uchijima and J. Nakamura. *Surf. Sci.,* **1998**, *400*, 387.

51. Y. Choi, K. Futagami, T. Fujitani and J. Nakamura. *Appl. Catal., A,* **2001**, *208*, 163.

52. P. R. Dennison, K. J. Packer and M. S. Spencer. *J. Chem. Soc., Faraday Trans.,* **1989**, *85*, 3537.

53. J. Yoshihara and C. T. Campbell. *J. Catal.,* **1996**, *161*, 776.

54. T. Fujitani and J. Nakamura. *Appl. Catal., A,* **2000**, *191*, 111.

55. R. Naumann d'Alnoncourt, M. Kurtz, H. Wilmer, E. Loeffler, V. Hagen, J. Shen and M. Muhler. *J. Catal.,* **2003**, *220*, 249.

56. H. B. Chen, D. W. Liao, L. J. Yu, Y. J. Lin, J. Yi, H. B. Zhang and K. R. Tsai. *Appl. Surf. Sci.,* **1999**, *147*, 85.

57. M. Kurtz, H. Wilmer, T. Genger, O. Hinrichsen and M. Muhler. *Catal. Lett.,* **2003**, *86*, 77.

58. J. Livage, M. Henry and C. Sanchez. *Prog. Solid State Chem.,* **1988**, *18*, 259.

59. P. Ratnasamy and A. J. Leonard. *J. Phys. Chem.,* **1972**, *76*, 1838.

60. A. E. Gash, T. M. Tillotson, J. H. Satcher Jr., L. W. Hrubesh and R. L. Simpson. *J. Non-Cryst. Solids,* **2001**, *285*, 22.

61. C. N. Chervin, B. J. Clapsaddle, H. W. Chiu, A. E. Gash, J. H. Satcher Jr. and S. M. Kauzlarich. *Chem. Mater.,* **2005**, *17*, 3345.

62. Lawrence livermore national laboratory,www-cms.llnl.gov, April 2006.

63. D. Kiessling, G. Wendt, K. Hagenan and R. Schoellner. *Appl. Catal.,* **1991**, *71*, 69.

64. G. M. Pajonk. *Appl. Catal.,* **1991**, *72*, 217.

65. V. Augugliaro, L. Palmisano, M. Schiavello and A. Sciafani. *J. Catal.,* **1986**, *99*, 62.

66. J. Sabate, M. A. Anderson, H. Kikkawa, M. Edwards and C. G. Hill. *J. Catal.,* **1991**, *127*, 167.

67. Y. Zhang, G. Xiong, N. Yao, W. Yang and X. Fu. *Catal. Today,* **2001**, *68*, 89.

68. W. Dai, Q. Liu, Y. Cao and J. Deng. *Appl. Catal. A,* **1998**, *175*, 83.

69. Y. Cao, J. Dai and J. Deng. *Mater. Lett.,* **2001**, *50*, 12.

70. Y. Dong, W. Dai, J. Li and J. Deng. *Chem. Lett.,* **2001**, *354*, 534.

71. L. Ren, W. Dai, Y. Cao and K. Fan. *Catal. Lett.,* **2003**, *85*, 81.

72. N. Moussa, A. Ghorbel and P. Grange. *J. sol-gel Sci. Tech.,* **2005**, *33*, 127.

73. P. Carlo and V. Pierluigi. *Catal. Today,* **1957**, *34*, 281.

74. G. J. Hutchings and J. C. Vedrine. Heterogeneous catalyst preparation. In: M. Baerns, ed. *Basic principles in applied catalysis*, vol. 75 New York, Springer, **2004**.

75. J. Rouxel. The chemistry and chemical reactivity of low-dimensional solids: some soft chemical approaches to the synthesis of new solid compounds. In: T. E. Mallouk, ed. *Advances in the synthesis and reactivity of solids*, vol. 2, London, Jai Press, **1994**.

76. J. Gopalakrishnan. *Chem. Mater.,* **1995**, *7*, 1265.

77. U. Behrens, A. K. Brimah and R. D. Fischer. *J. Organomet. Chem.,* **1991**, *411*, 325.

78. U. Behrens, A. K. Brimah, T. M. Soliman, R. D. Fischer, D. C. Apperley, N. A. Davies and R. K. Harris. *Organometallics,* **1992**, *11*, 1718.

79. S. Eller, P. Schwarz, A. K. Brimah, R. D. Fischer, D. C. Apperley, N. A. Davies and R. K. Harris. *Organomet.,* **1993**, *12*, 3232.

80. M. Rehbein, M. Epple and R. D. Fischer. *Solid State Sci.,* **2000**, *2*, 473.

81. M. Rehbein, R. D. Fischer and M. Epple. *Thermochim. Acta,* **2002**, *382*, 143.

82. M. Heibel, G. Kumar, C. Wyse, P. Bukovec and A. B. Bocarsly. *Chem. Mater.,* **1996**, *8*, 1504.

83. S. L. Sharp, G. Kumar, E. P. Vicenzi, A. B. Bocarsly and M. Heibel. *Chem. Mater.,* **1998**, *10*, 880.

84. A. M. Silva, O. A. A. Santos, M. J. Mendes, E. Jordao and M. A. Fraga. *Appl. Catal. A,* **2003**, *241*, 155.

85. M. J. Mendes, O. A. A. Santos, E. Jordao and A. M. Silva. *Appl. Catal. A,* **2001**, *217*, 253.

86. V. A. Chaudhary, I. S. Mulla, K. Vijayamohanan, S. G. Hegde and D. Srinivas. *J. Phys. Chem. B,* **2001**, *105*, 2565.

87. B. E. Conway. *J. Electrochem. Soc.,* **1991**, *138*, 1539.

88. J. P. Zheng and T. R. Jow. *J. Electrochem. Soc.,* **1995**, *142*, L6.

89. N. L. Wu, S. L. Kuo and M. H. Lee. *J. Power Source,* **2002**, *104*, 62.

90. M. Ito, Y. Murakami, H. Kaji, H. Ohkawauchi, K. Yahikozawa and Y. Takasu. *J. Electrochem. Soc.,* **1994**, *141*, 1243.

91. X. Wang, D. Tang and J. Zhou. *Guisuanyan Xuebao,* **2002**, *30 (Suppl.)*, 49.

92. H. Hanika-Heidl and R. D. Fischer. *Inorg. Chim. Acta,* **2004**, *357*, 1748.

93. O. Nial. *Svensk Kem. Tidskr.,* **1947**, *59*, 172.

94. O. Schwomma, H. Nowotny and A. Wittmann. *Monatsh. Chemie,* **1964**, *95*, 1538.

95. A. Ciccioli, G. Balducci, G. Gigli, L. Pering and J. C. G. Kuntz, J.C. *Ber. Bunsen-Ges. Phys. Chem.,* **1998**, *102*, 1275.

96. S. V. Meschel and O. J. Kleppa. *Thermochim. Acta,* **1998**, *314*, 205.

97. L. Eriksson and J. Lanner. *Acta Cryst.,* **2001**, *E57*, i85.

98. H. P. Klug and L. E. Alexander. *X-ray diffraction procedures for polycrystalline and amorphous materials*, New York, Wiley-Interscience, **1974**.

99. G. McCarthy and J. Welton. *Powder Diffr.,* **1989**, *4*, 156.

100. C. E. Boman. *Acta Chim. Scand.,* **1970**, *24*, 116.

101. Y. Chen, X. Xia, Y. Chen and J. Chen. *Huagong Xuebao (Chinese Edition),* **1996**, *47*, 42.

102. O. Vazquez Cuchillo, U. Pal and C. Vazquez Lopez. *Modern Phys. Lett. B,* **2001**, *15*, 675.

103. S. M. Zhou, X. H. Zhang, X. M. Meng, K. Zou, X. Fan, S. K. Wu and S. T. Lee. *Nanotechnology,* **2004**, *15*, 1152.

104. L. Guo and S. Yang. *Chem. Mater.,* **2000**, *12*, 2268.

105. A. M. Pollard, M. S. Spencer, R. G. Thomas, P. A. Williams, J. Holt and J. R. Jennings. *Appl. Catal. A,* **1992**, *85*, 1.

106. Y. Choi, K. Futagami, F. T. and J. Nakamura. *Appl. Catal. A,* **2001**, *208*, 163.

107. K. D. Jung and O. S. Joo. *Catal. Lett.,* **2002**, *84*, 21.

108. H. Wilmer, T. Genger and O. Hinrichsen. *J. Catal.,* **2003**, *215*, 188.

109. B. L. Kniep, T. Ressler, A. Rabis, F. Girgsdies, M. Baenitz, F. Steglich and R. Schlögl. *Angew. Chem.,* **2004**, *116*, 114.

110. J. Hambrock, M. K. Schroeter, A. Birkner, C. Woell and R. A. Fischer. *Chem. Mater.,* **2003**, *15*, 4217.

111. Y. Guo, R. Weiss and M. Epple. *J. Mater. Chem.,* **2005**, *15*, 424.

112. T. Welzel, W. Meyer-Zaika and M. Epple. *Chem. Commun.,* **2004**, 1204.

113. M. Schur, B. Bems, A. Dassenoy, I. Kassatkine, J. Urban, H. Wilmes, O. Hinrichsen, M. Muhler and R. Schlögl. *Angew. Chem.,* **2003**, *115*, 3945.

114. P. J. Ellis and H. C. Freeman. *J. Synchrotron Rad.,* **1995**, *2*, 190.

115. E. A. Stern, M. Newville, B. Ravel, Y. Yacoby and D. Haskel. *Physica B,* **1995**, *208-209*, 117.

116. O. Hinrichsen, T. Genger and M. Muhler. *Chem. Eng. Technol.,* **2000**, *11*, 956.

117. C. Kiener, M. Kurtz, H. Wilmer, C. Hoffmann, H. W. Schmidt, J. D. Grunwaldt, M. Muhler and F. Schüth. *J. Catal.,* **2003**, *216*, 110.

118. R. M. Izatt, J. J. Christensen, J. W. Hansen and G. D. Watt. *Inorg. Chem.,* **1965**, *4*, 718.

119. R. Paterson and J. Bjerrum. *Acta Chim. Scand.,* **1965**, *19*, 729.

120. J. Cernak, Z. Zak, J. Chomic and C. Kappenstein. *Acta Crystallogr. C,* **1998**, *54*, 1551.

121. A. G. Sharpe. In: P. M. Maitlis, S. West, ed. *The chemistry of cyano complexes of the transition metals,* London, **1976**.

122. W. Grünert, N. W. Hayes, R. W. Joyner, E. S. Shpiro, M. R. H. Siddiqui and G. N. Baeva. *J. Phys. Chem. A,* **1994**, *98*, 10832.

123. G. U. Kulkarni and C. N. R. Rao. *Top. Catal.,* **2003**, *22*, 183.

124. N. Uekawa, R. Yamashita, Y. Wu and K. Kakegawa. *Phys. Chem. Chem. Phys.,* **2004**, *6*, 442.

125. M. Mo, J. C. Yu, L. Zhang and S. A. Li. *Adv. Mater.,* **2005**, *17*, 756.

126. J. Y. Lao, J. G. Wen and Z. F. Ren. *Nano Lett.,* **2002**, *2*, 1287.

127. K. S. Choi, H. C. Lichtenegger, G. D. Stucky and E. W. McFarland. *J. Am. Chem. Soc.,* **2002**, *124*, 12402.

128. P. X. Gao and Z. L. Wang. *J. Am. Chem. Soc.,* **2003**, *125*, 11299.

129. H. Wilmer, M. Kurtz, K. Klementiev, O. Tkachenko, W. Grünert, O. Hinrichsen, A. Birkner, S. Rabe, K. Merz, M. Driess, C. Wöll and M. Muhler. *Phys. Chem. Chem. Phys.,* **2003**, *5*, 4736.

130. L. Vayssieres. *Adv. Mater.,* **2003**, *15*, 464.

131. J. Q. Hu, Y. Bando, J. H. Zhan, Y. B. Li and T. Sekiguchi. *Appl. Phys. Lett.,* **2003**, *83*, 4414.

132. J. Q. Hu, Q. Li, X. M. Meng, C. S. Lee and S. T. Lee. *Chem. Mater.,* **2003**, *15*, 305.

133. F. Li, Y. Ding, P. Gao, X. Xin and Z. L. Wang. *Angew. Chem. Int. Ed.,* **2004**, *43*, 5238.

134. W. I. Park and G. C. Yi. *Adv. Mater.,* **2004**, *16*, 87.

135. X. Y. Kong, Y. Ding, R. Yang and Z. L. Wang. *Science,* **2004**, *303*, 1348.

136. Z. K. Tang, G. K. L. Wong, P. Yu, M. Kawasaki, A. Ohtomo, H. Koinuma and Y. Segawa. *Appl. Phys. Lett.,* **1998**, *72*, 3270.

137. C. Pacholski, A. Kornowski and H. Weller. *Angew. Chem. Int. Ed.,* **2002**, *41*, 1188.

138. M. Shim and P. Guyot-Sionnest. *J. Am. Chem. Soc.,* **2001**, *123*, 11651.

139. J. Hambrock, S. Rabe, K. Merz, A. Birkner, A. Wohlfart, R. A. Fischer and M. Driess. *J. Mater. Chem.,* **2003**, *13*, 1731.

140. Y. Guo, R. Weiss and M. Epple. *J. Mater. Chem.,* **2005**, *15*, 424.

141. Y. Guo, R. Weiss and M. Epple. *Eur. J. Inorg. Chem.,* **2005**, 3072.

142. R. Weiss, G. Jansen, R. Boese and M. Epple. *Dalton Trans,* **2006**, 1831.

143. J. Cernak, I. Potocnak and J. Chomic. *J. Therm. Ana. Cal.,* **1993**, *39*, 849.

144. G. M. J. Schmidt and M. D. Cohen. *J. Chem. Soc.,* **1964**, 1996.

145. C. Chauvin, J. Jaussey, J. C. Lavalley, H. Idriss, J. P. Hidermann, A. Kiennemann, P. Chaumette and P. Coutry. *J. Catal.,* **1990**, *121*, 56.

146. N. Guilhaume and M. Primet. *J. Chem. Soc. Faraday Trans.,* **1994**, *90*, 1541.

147. J. R. Jensen, T. Johannessen, S. Wedel and H. Livbjerg. *J. Nanopart. Res.,* **2000**, *2*, 363.

148. C. O. Areán, B. S. Sintes, G. T. Palomino, C. M. Carbonell, E. E. Platero and J. B. P. Soto. *Microporous Mater.,* **1997**, *8*, 187.

149. L. Ji, J. Lin, K. L. Tan and H. C. Zeng. *Chem. Mater.,* **2000**, *12*, 931.

150. C. L. Carners, P. N. Kapoor and K. J. Klabunde. *J. Chem. Mater.,* **2002**, *14*, 2922.

151. J. Sanchez-Valente, X. Bokhimi and F. Hernandez. *Langmuir,* **2003**, *19*, 3583.

152. S. Liu, U. Fooken, C. M. Burba, M. A. Eastman and R. Wehmschulte. *J. Chem. Mater.,* **2003**, *15*, 2803.

153. T. F. Baumann, A. E. Gash, S. C. Chinn, A. M. Sawvel, R. S. Maxwell and J. H. Satcher Jr. *Chem. Mater.,* **2005**, *17*, 395.

154. A. E. Gash, J. H. Satcher Jr. and R. L. Simpson. *Chem. Mater.,* **2003**, *15*, 3268.

155. A. E. Gash, T. M. Tillotson, J. H. Satcher Jr., J. F. Poco, L. W. Hrubesh and R. L. Simpson. *Chem. Mater.,* **2001**, *13*, 999.

156. B. J. Clapsaddle, A. E. Gash, J. H. Satcher and R. L. Simpson. *J. Non-Cryst. Solids,* **2003**, *331*, 190.

157. B. J. Clapsaddle, A. E. Gash, J. H. Satcher and R. L. Simpson. *J. Non-Cryst. Solids,* **2004**, *350*, 173.

158. G. J. Hutchings and J. C. Vedrine. *Basic principles in applied catalysis*, vol. 75, New York, Springer, **2004**.

159. R. W. G. Wyckoff. *Crystal Structures*, New York, John Wiley & Sons, **1963**.

160. R. Weiss, Y. Guo, S. Vukojevic, L. Khodeir, R. Boese, F. Schüth, M. Muhler and M. Epple. *Eur. J. Inorg. Chem.,* **2006**, 1796.

161. S. Hingorani and V. Pillai. *Mat. Res. Bull.,* **1993**, *28*, 1303.

162. S. C. Lyu, Y. Zhang, H. Ruh, H. J. Lee, H. W. Shim, E. K. Suh and C. J. Lee. *Chem. Phys. Lett.,* **2002**, *363*, 134.

163. J. J. Wu and S. C. Liu. *J. Phys. Chem. B,* **2002**, *106*, 9546.

164. W. T. Chiou, W. Y. Wu and J. M. Ting. *Diamond Relat. Mater.,* **2003**, *12*, 1841.

165. Y. G. Wang, C. Yuen, S. P. Lau, S. F. Yu and B. K. Tay. *Chem. Phys. Lett.,* **2003**, *377*, 329.

166. J. Q. Hu, X. L. Ma, Z. Y. Xie, N. B. Wong, C. S. Lee and S. T. Lee. *Chem. Phys. Lett.,* **2001**, *344*, 97.

167. D. S. Boyle, K. Govender and P. O'Brien. *Chem. Commun.,* **2002**, *1*, 80.

168. P. Li, Y. Wei, H. Liu and X. Wang. *Chem. Commun.,* **2004**.

169. W. J. Li, E. W. Shi, W. Z. Zhong and Z. W. Yin. *J. Cryst. Growth,* **1999**, *203*, 186.

170. J. B. Reitz and E. I. Solomon. *J. Am. Chem. Soc.,* **1998**, *120*, 11467.

171. A. Chowdhuri, V. Gupta, K. sreenivas, R. Kumar, S. Mozumdar and P. K. Patanjali. *Appl. Phys. Lett.,* **2004**, *84*, 1180.

172. C. T. Hsieh, J. M. Chen, H. H. Lin and H. C. Shih. *Appl. Phys. Lett.,* **2003**, *83*, 3383.

173. R. V. Kumar, Y. Diamant and A. Gedanken. *Chem. Mater.,* **2000**, *12*, 2301.

174. X. Jiang, T. Herricks and Y. Xia. *Nano Lett.,* **2002**, *2*, 1333.

175. S. H. Wang, Q. J. Huang, X. G. Wen, X. Y. Li and S. H. Yang. *Phys. Chem. Chem. Phys.,* **2002**, *4*, 3425.

176. X. P. Gao, J. L. Bao, G. L. Pan, H. Y. Zhu, P. X. Huang, F. Wu and D. Y. Song. *J. Phys. Chem. B,* **2004**, *108*, 5547.

177. B. Liu and H. C. Zeng. *J. Am. Chem. Soc.,* **2004**, *126*, 8124.

178. C. Lu, L. Qi, J. Yang, D. Zhang, N. Wu and J. Ma. *J. Phys. Chem. B,* **2004**, *108*, 17825.

179. C. J. Johnson, M. Li and S. Mann. *Adv. Funct. Mater.,* **2004**, *14*, 1233.

180. J. D. Hopwood and S. Mann. *Chem. Mater.,* **1997**, *9*, 1819.

181. G. D. Rees, R. Evans-Gowing, S. J. Hammond and B. H. Robinson. *Langmuir,* **1999**, *15*, 1993.

182. F. J. Arriagada and K. Osseo-Asare. *Colloid interface Sci.,* **1995**, *170*, 8.

183. M. Li and S. Mann. *Langmuir,* **2000**, *16*, 7088.

184. H. Colfen and S. Mann. *Angew. Chem. Int. Ed.,* **2003**, *42*, 2350.

185. S. Amelinckx, D. van Dyck, J. van Landuyt and G. van Tendeloo. *Handbook of microscopy*, Weinheim, **1997**.

186. S. Amelinckx. *Electron Microscopy*, New York, Wiley, **1997**.

187. J. W. Niemantsverdriet. *Spectroscopy in Catalysis*, Weinheim, Wiley-VCH, **2000**.

188. J. V. Sanders. *Catalysis Science and Technology*, vol. 7, Berlin, Springer, **1985**.

189. C. Kittel. *Elementary Solid State Physics: A Short Course*, New York, Wiley, **1962**.

190. N. W. Ashcroft and N. D. Mermin. *Solid State Physics*, Philadelphia, Holt-Saunders, **1976**.

191. J. B. Cohen and L. H. Schwartz. *Diffraction from Materials*, New York, Springer-Verlag, **1987**.

192. C. Suryanarayana and M. Grant Norton. *X-ray Diffraction: A Practical Approach*, New York, Plenum, **1998**.

193. D. C. Koningsberger and R. Prins. *X-ray Absorption*, New York, Wiley, **1987**.

194. W. Kossel. *Z. Phys.,* **1920**, *1*, 119.

195. D. E. Sayers, F. W. Lytle and E. A. Stern. *Phys. Rev. Lett.,* **1971**, *27*, 1204.

196. J. H. Sinfelt, G. H. Via and F. W. Lytle. *Catal. Rev. Sci. Eng.,* **1984**, *26*, 81.

197. J. Stöhr. *NEXAFS Spectroscopy*, New York, Springer Verlag, **1996**.

198. M. Vaarkamp. *Catal. Today,* **1998**, *39*, 271.

199. W. O. George and P. S. Mcintyre. *Infrared Spectroscopy*, Chichester, Wiley, **1987**.

200. P. R. Griffiths. *Chemical Infrared Transform Spectroscopy*, Chichester, Wiley, **1975**.

201. W. F. Hemminger and H. K. Cammenga. *Methoden der Thermischen Analyse*, Springer Verlag, **1989**.

202. D. Krug. Kalorimetrie und Thermische Analyse. In: H. Naumer, ed. *Untersuchungsmethoden in der Chemie-Einführung in die moderne Analytik*, Thieme Verlag, **1990**.

203. S. J. Gregg and K. S. W. Sing. *Adsorption, surface area and porosity*, Academic Press Inc., **1982**.

204. M. M. Dubinin and L. V. Radushkevich. *Proc. Acad. Sci. USSR,* **1947**, *55*.

205. P. J. M. Carrott, R. A. Roberts and K. S. W. Sing. *Characterization of Porous Solids*, vol. 89, Elsevier Science, **1988**.

206. F. Stoeckli, D. Huguenin and A. Greppi. *J. Chem. Soc. Faraday Trans.,* **1993**, *89*, 2055.

207. K. Kaneko, C. Ishii, M. Ruike and H. Kuwabara. *Carbon,* **1992**, *30*, 1075.

208. S. Brunauer, P. H. Emmett and E. Teller. *J. Am. Ceram. Soc.,* **1938**, *60*, 309.

209. F. Rouquerol, J. Rouquerol and K. S. W. Sing. *Adsorption by Powers and Porous Solids*, Academic Press Inc., **1999**.

210. F. Stoeckli, P. Rebstein and L. Ballerini. *Carbon,* **1990**, *28*, 907.

211. H. F. Stoeckli. *J. Colloid Interf. Sci.,* **1977**, *59*, 184.

212. E. P. Barrett and L. G. Joyner. *Electrochemical Methods*, John Wiley & Sons, **1980**.

213. G. W. Scherer. *J. Non-Cryst. Solids,* **1998**, *225*, 192.

References

11 Appendices

11.1 List of abbreviations

BET   Method after Brunauer, Emmett and Teller

BJH   Method after Barrett, Joyner and Halenda

DESY   Deutsches Elektronensynchrotron

DTA   Differential thermal analysis

EDX   Energy dispersive X-ray analysis

EXAFS   Extended X-ray absorption fine structure

FWHM   Full width at half maximum

HASYLAB   Hamburg Synchrotronradiation Laboratory

SEM   Scanning electron microscopy

TEM   Transmission electron microscopy

TG   Thermogravimetry

TG-IR   Thermogravimetry-infrared spectroscopy

TG-MS   Thermogravimetry-mass spectrometry

XRD   X-ray diffraction

11.2 Safety and disposal of chemicals

The following list contains all chemical compounds, which were used in experiments for this work. The column "Symbol" lists the international hazard symbols appropriate for specific compounds. "R-Sätze" and "S-Sätze" are lists of dangers and safety precautions demanded by German law.

Chemical	Symbol	R-Sätze	S-Sätze	Disposal
Acetone	F	11	9-16-23-33	1
Aluminum nitrate 9-hydrate	O, X_i	8-36/38	17-26-36	2
Aluminum oxide	X_i	37	22-36	3
Copper nitrate 3-hydrate	O, C	8-22-34	17-26-36/37/39-45	2
Copper sulfate 5-hydrate	X_i, N	22-36/38-50/53	22-60-61	2
Ethanol	F	11	7-16	1
Ethylenediamine	C	10-21/22-34-42	23-26-36/37-45	1
Sodium cyanide	T^+	26/27/28-32-50/53	7-28-29-45-60-61	4
Sodium hydroxide	C	35	26-37/39-45	5
Sodium bis(2-ethylhexyl) sulfosuccinate	X_i	22-38-41	26-39	3
Potassium cyanide	T^+	26/27/28-32-5053	7-28-29-45-60-61	4
Potassium hexacyanoruthenate	T^+	32	22-24/25	4
Propylene oxide	F, T	45-46-12-20/21/22-36/37/38	53.1-45	--
Trimethyl tin chloride	T^+	26/27/28	26-27-28-45	6
Zinc nitrate 6-hydrate	O, X_i	8-22-36/37/38	17-26	2
Zinc sulfate 7-hydrate	X_n	36/38-50/53	22-25-60-61	2

Disposal:

1:      organic solvents were disposed in a container for organic halogen-free solvents;

2:      inorganic compounds were dissolved in water, made acidic and transferred to a container for acidic heavy metal solutions;

3:      solids were disposed in a container for solid waste;

4:      cyanide compounds were dissolved in water. The pH was adjusted to 10-11 and surplus hydrogen peroxide was then added. After stirring for 1h, sulfuric acid was added to adjust the pH to 8-9. The solution was then made acidic and transferred to a container for acidic heavy metal solutions;

5:      it was dissolved in water and disposed in a container for alkaline solutions;

6:      it was disposed in a container for toxic solid waste.

11.3 Publications

Yanzhi Guo, Rainer Weiss, Matthias Epple, Thermolysis of tetrakis(trimethyltin)hexacyanoruthenate(II): preparation and characterization of Ru₃Sn₇ and (Ru,Sn)O₂, *Journal of Materials Chemistry*, **2005**, *15*, 424.

Yanzhi Guo, Rainer Weiss, Matthias Epple, A straightforward route to copper/zinc oxide nanocomposites: the controlled thermolysis of Zn[Cu(CN)₃], *European Journal of Inorganic Chemistry*, **2005**, 3072.

Yanzhi Guo, Rainer Weiss, Roland Boese, Matthias Epple, Synthesis, structural characterization and thermochemical reactivity of tris(ethylenediamine)zinc tetracyanozincate, a precursor for nanoscale ZnO, *Thermochimica Acta*, **2006**, *446*, 101.

Yanzhi Guo, Wolfgang Meyer-Zaika, Martin Muhler, Sascha Vukojević, and Matthias Epple, Cu/Zn/Al-xerogels and aerogels as catalysts for methanol synthesis prepared by sol-gel reactions, *European Journal of Inorganic Chemistry*, in press.

Rainer Weiss, **Yanzhi Guo**, Sascha Vukojević, Lamma Khodeir, Roland Boese, Ferdi Schüth, Martin Muhler, Matthias Epple, Catalytic activity of copper oxide/zinc oxide composites prepared by thermolysis of crystallographically defined bimetallic coordination compounds, *European Journal of Inorganic Chemistry*, **2006**, 1796.

Carla Hipólito, João Paulo Leal, **Yanzhi Guo**, Matthias Epple, Thermochemistry of alkaline-earth phenoxides, *Journal of Chemical Thermodynamics,* **2006**, *38*, 296.

Yanzhi Guo, Matthias Epple, Thermolysis of complex metal cyanide to CuO/ZnO and its structural investigation by EXAFS, *HASYLAB Annual Report*, **2003**.

Yanzhi Guo, Rainer Weiss, Matthias Epple, EXAFS Study of copper zinc oxide catalysts prepared by thermolysis of a copper-zinc cyanide complex, *HASYLAB Annual Report*, **2005**.

Curriculum Vitae

Personal details

Family Name   Guo

Given Name   Yanzhi

Sex   Female

Date of Birth   April 27, 1976

Nationality   P. R. China

Marital status   Married

Education

09.1994–07.1999   **Bachelor,** Applied chemistry, Tongji University, Shanghai.

09.1999–06.2002   **Master,** Materials chemistry and physics, Tongji University, Shanghai,

in which, during 07/2001–06/2002 work for a joint project in Experimental Physics II, Bayerische Julius-Maximilians University Würzburg, Germany

05.2003–09.2003   **Ph.D student**, Institute of Inorganic Chemistry (Prof. M. Epple),
Ruhr University Bochum, Germany.

10.2003–06.2006   **Ph.D student**, Institute of Inorganic Chemistry (Prof. M. Epple),
University Duisburg-Essen, Germany.

Acknowledgements

This research would not have been possible and would not be complete without acknowledging the people who have been instrumental in encouraging and guiding me all through.

My sincere thanks are given to

Prof. Dr. Matthias Epple for providing me the chance to do my PhD work, and for his scientific guidance and support,

Mr. Rainer Weiß for fruitful discussions and experimental support,

Dr. Wolfgang Meyer-Zaika for TEM measurements,

Prof. Dr. Martin Muhler, Ms. Lamma Khodeir, Mr. Ralf Bergsträßer and Ms. Susanne Buse (Laboratory of Industrial Chemistry, Ruhr University Bochum), Prof. Dr. Ferdi Schüth and Mr. Sascha Vukojević (Max-Planck Institute for Coal Research) for productive research collaborations on calcination experiments and the measurements of BET surface area, Cu surface area, and catalytic activities,

Mr. S. Boukercha and Dr. R. Neuser (Ruhr University of Bochum) for SEM measurements,

Ms. K. Brauner and Ms. V. Hiltenkamp for all elemental analysis and AAS-measurements,

Dr. Mark Schumann for XRD measurements, and

all the colleagues in AK Epple for the friendly atmosphere that I enjoyed so much in the last 3 years.

My special thanks are given to my husband Wei for his continuous support, and to my parents in China for their unconditional backup.

Thanks are also given to the Deutsche Forschungsgemeinschaft (DFG) for financial support within the scope of the Collaborative Research Center SFB 558. The synchrotron beam-time was kindly provided by HASYLAB at DESY (Hamburg).

Eidesstattliche Erklärung

Hiermit erkläre ich, die vorliegende Arbeit selbständig durchführt und keine anderen als die angegebenen Hilfsmittel verwendet zu haben.

Essen, im Juli 2006

Yanzhi Guo